Kurzfassung

Injektions- und Rekombinationsphänomene in organischen Dünnschichtbauelementen

Mit Hilfe dünner Schichten aus organischen halbleitenden Materialien lassen sich verschiedenartige elektrische Bauelemente realisieren. Diese umfassen unter anderem Leuchtdioden, Solarzellen, Photodioden und Transistoren. Gegenüber konventionellen, auf anorganischen Halbleitern basierenden elektrischen Bauelementen ergeben sich vielfältige Vorteile in Bezug auf den Herstellungsprozess. Eine entscheidende Eigenschaft für ihre Funktionsweise ist die Ladungsträgerinjektion von den Elektroden in die aktive Schicht. Die energetischen Barrieren für diesen Prozess werden im wesentlichen durch die Potentialdifferenz zwischen dem Oxidations- bzw. Reduktionspotentials des Halbleiters, sowie der Austrittsarbeit des Elektrodenmaterials bestimmt. In der vorliegenden Arbeit wird das elektrische Feld, das in dieser Potentialdifferenz seine Ursache hat, systematisch untersucht und seine Bedeutung für die Funktionsweise diverser Halbleiterbauelemente studiert. In Abwesenheit signifikanter Mengen an beweglichen Ladungsträgern bildet sich ein homogenes elektrisches Feld über die aktive Schicht aus. Besonders der Effekt der Einbettung einer starken Elektronenakzeptor Spezies in eine Elektrondonormatrix wurde untersucht. Diese Materialkombination ist für die Herstellung effizienter organischer Solarzellen notwendig. Das in der aktiven Schicht bestehende, eingebaute elektrische Feld konnte als Triebkraft des Fotostroms identifiziert werden und limitiert damit die maximale Spannung, die dieses Photovoltaische Element liefern kann. Des weiteren wurde ein System untersucht, dem durch Dotierung zusätzliche, bewegliche wie stationäre, Ladungen zugefügt werden können, die die Ausbildung eines homogenen elektrischen Feldes in der Halbleiterschicht verhindern. Die Ladungsträgerinjektion in solche dotierten Proben konnte erfolgreich im Rahmen eines Schottky Kontaktes beschrieben werden. In einem zweiten Teil wird die Rekombination von injizierten Ladungsträgern untersucht. Ungleichnamige Ladungen, die sich in der aktiven Schicht treffen, löschen einander aus. Dies kann je nach Material unter Abgabe von Licht erfolgen. Diese Rekombination kann verschiedenen Mechanis-

men folgen, die sich unter anderem in Ihrer Zeitkonstante unterscheiden. Impedanzspektroskopie ist ein probates Mittel für die Untersuchung dieser Prozesse, da sich die Frequenz und damit die Zeitdomäne über mehrere Größenordnungen variieren lässt. Das oftmals beobachtete Phänomen einer negativen Kapazität wurde der Elektronen-Loch Rekombination zugeordnet. Die erhaltenen Spektren konnten mit einem einheitlichen Formalismus beschrieben werden, der auch diese negative Kapazität beinhaltet.

Acknowledgement

Contents

Chapter 1

Introduction

1.1 Motivation

Organic semiconductors are interesting materials as they show many unique properties unknown to their inorganic counterparts. The electronic properties of some organic molecules with conjugated π-electron systems have already been under investigation for several decades (e. g. [1, 2, 3]). Even today, these so-called "small molecules" and the thin film devices prepared thereof, draw significant interest and are studied in great detail. In the late seventies [4, 5, 6] a group of novel materials was added to the family of organic semiconductors: π-conjugated polymers like polyacetylene and their electronic properties were discovered. The key persons in this discovery and the following development, H. Shirakawa, A. G. MacDiarmid and A. J. Heeger were awarded the Nobel Prize for Chemistry in 2000. The members of this special class of polymers can be doped and by doing so, their conductivity is varied over several orders of magnitude. An enormous development followed the initial discovery and a whole variety of π-conjugated polymers were synthesized, most prominent those based on poly(phenylene vinylene), polyfluorene or polythiophene units. Application of side chains to the backbone of the polymers drastically improves their solubility in common organic solvents. This allows to cast thin polymer films from solution by using various established techniques including printing. The scientific research and development towards possible applications of these polymeric compounds basically points into two directions. The first is interested in doped polymers that show good conductivity as thin films (antistatic coat-

ing, etc.). The second one aims for undoped polymers, making use of their semiconductor properties. Many devices analogous to their inorganic counterparts have already been realized. Among these are diodes, photo-diodes, solar cells, transistors and light emitting diodes. Many materials used nowadays, which exhibit promising properties have band-gaps around 2 eV [7]. This comparably large energy gap limits the number of thermally excited mobile charge carriers at room temperature (roughly 10^{10} cm^{-3}). Furthermore impurities act in most cases as traps for charge transport rather than as a source of mobile carriers. From this point of view the π-conjugated polymers should be considered as electrical insulators, not as semiconductors [8]. Although large crystals of organic electronic materials are available (e. g. [2]), they are usually employed in their amorphous or partly crystalline form. This leads to several differences compared to the conventional Si based semiconductor technology. Whereas the charges in Si crystals are transported in the band structures [9], in the disordered organic materials the charge carriers appear to be localized. Band transport seems to be largely replaced by variable range hopping processes [10, 11]. Furthermore the purity of available organic semiconductors is way below what is used by the Si based semiconductor industry. These impurities are frequently made responsible for the poor performance of many organic semiconductor devices as compared to their inorganic counterparts, especially for photovoltaic devices [12, 13, 7, 14] and transistors [9].

However, despite these indisputable disadvantages in terms of performance, some unique properties of organic semiconductors may enable them to open new fields of applications that might be impossible to serve with the available conventional inorganic semiconductor technology. Thin layers of organic semiconductors can be produced from solution by using well established industrial printing techniques [15]. These films are the basis of many semiconductor devices, hence enabling the production of printed electronics. The benefits and possibilities of this new field of semiconductor technology are about to be developed and realized.

1.2   Injection and recombination

Charge carrier injection and recombination phenomena are important effects governing many properties of organic semiconductor thin film devices.

Organic semiconductor/metal interfaces behave in many respects differently from their inorganic counterparts [9]. In the inorganic crystals bonds have to be broken to be able to form the interface. Hence unbound valence electrons are available at the surface ("dangling bonds"), which are highly reactive. This leads to interface states determining much of the behavior of devices incorporating this interface. Such phenomena are unknown to organic semiconductor devices based on π-conjugated polymers or evaporated small molecules. No carbon-carbon bonds have to be broken to form the interface.

In this work, the injection of charge carriers into thin films of π-conjugated polymers will be studied. Various contact metals, polymers and their blends with electron acceptors are subject to the experiments. The electric field inside organic semiconductor thin film devices is studied by Electroabsorption spectroscopy. General questions on the influence of the internal electric field in the diodes on their performance, or how the introduction of an electron accepting species affects the photovoltaic performance of the donor-acceptor based devices, are addressed. If injected electrons and holes recombine in the polymer diodes, light is emitted, hence indicating the bipolar characteristic of the device. The transport of the injected charge carriers will be described in the framework of space charge limited current (SCLC) (e. g. [16]). Admittance studies are presented, fitted and interpreted within the SCLC theory for both, monopolar and bipolar devices.

1.3 The internal electric field in organic semiconductor thin film devices

In the first part, the internal electric field in organic semiconductor thin film devices is studied. Three different cases are compared: The first is the one of diodes based on a conjugated polymer with an insignificant amount of mobile charge carriers. A soluble poly(phenylene vinylene) (PPV) derivative, namely MDMO-PPV is employed as a model system [17, 18]. Secondly, another type of device based on a different polymer is investigated. This system uses thin films of poly(3-hexylthiophene), hence incorporating a material that is becoming p-doped upon exposure to oxygen [19, 20] and/or moisture [21]. Furthermore, MDMO-PPV is blended with a fullerene derivative. Such mixtures form the basis for organic bulk heterojunction solar cells
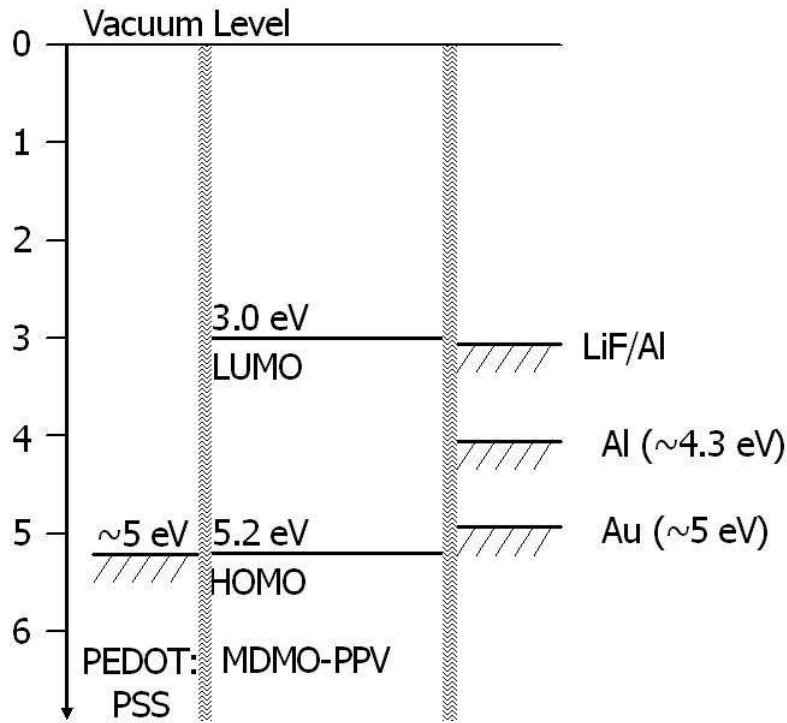
Figure 1.1: Scheme depicting the relevant energy levels for ITO - PE-DOT:PSS - MDMO-PPV thin film devices with various top electrodes. Due to our experimental results energetic alignment between the highest occupied molecular level (HOMO) of MDMO-PPV and PEDOT:PSS as well as between the lowest unoccupied molecular level (LUMO) of MDMO-PPV and LiF/Al is assumed. Interface effects are not included in the scheme.

in which an electron donating species (the π-conjugated polymer) is blended with an electron accepting species (the fullerene derivative) [22, 23].

1.3.1 Slightly doped π-conjugated polymers

MDMO-PPV is used as a model system, because it is known for its low amount of mobile charge carriers in the dark. Figure 1.1 displays the relevant energy levels of the studied devices. Indium tin oxide (ITO) covered with a layer of poly(3,4-ethylenedioxythiophene) doped with poly(styrenesulfonate) (PEDOT:PSS) is employed as hole injecting contact. It is the same in all devices, whereas the electron injecting contact is changed from Au via Al to LiF/Al. The work functions of Al, Au [24] and PEDOT:PSS are plotted in Fig. 1.1 together with the highest occupied (HOMO) and the lowest unoc-

4

cupied molecular orbital (LUMO) levels of MDMO-PPV.

Introducing a nominally 0.7 nm thick LiF layer, between the polymer film and the Al electrode, light emission of organic light emitting diodes is typically enhanced [25]. This is explained by a reduction of the barrier towards electron injection for LiF/Al as compared to Al electrodes [26, 27, 28]. Due to the offset between the work functions of the contact metals and the LUMO of MDMO-PPV an increasing barrier for electron injection is expected from LiF/Al via Al to Au.

Under short circuit conditions, it is expected that the work function mismatch of the electrodes in devices based on MDMO-PPV causes a homogeneous internal electric field (V_{int}/d, d being the thickness of the film) across the active layer. This situation is schematically depicted in Fig. 1.3(a). The rectifying behavior of devices based on π-conjugated polymers containing a sufficiently small amount of mobile charge carriers in the dark has been described within the Metal-Insulator-Metal (MIM) framework [29]. The concentration of mobile charges is too small to allow Fermi level alignment across the device or distortion of the electric field. In reverse direction (ITO is wired −, the metal top electrode +) injection of additional free charges from the electrodes is energetically unfavorable (Fig. 1.2). Under forward bias, injection of charge carriers is explained in the framework of the MIM picture by a tunneling process (Fig. 1.3(c)). It is described to happen via a Fowler-Nordheim mechanism across a triangular barrier rather than following the Schottky theory [29, 9]. A sufficiently large applied electric field can enable current flow across the barrier [29] according to:

$$I_{FN} = k_1 E^2 e^{-k_2/E} \ , \tag{1.1}$$

where I_{FN} is the Fowler-Nordheim tunneling current, k_1 and k_2 are constants and E is the electric field strength.

In the absence of a significant amount of charge carrier injection, Electroabsorption (EA) spectroscopy [24] is an appropriate tool to study the electric field inside the diodes. The experiments were carried out at low temperatures of around 100 K in order to avoid disturbing effects due to current flow induced by the applied bias [28]. At these temperatures, π-conjugated polymers such as the used PPV derivative [30] show an orders of magnitude reduced conductivity as compared to room temperature due to the

pronounced temperature dependence of the charge carrier mobility [31, 11]. It was shown that 100 K are sufficient to ensure reliable EA measurements on MDMO-PPV based diodes [28]. By studying the homogeneous electric field E

$$E = \frac{V_{dc} - V_{int}}{d} \tag{1.2}$$

across the active layer, the internal electric field and therefore the barrier for charge carrier injection can be estimated.

1.3.2   Intentionally doped π-conjugated polymers

Expressing the internal electric field under short circuit conditions as V_{int}/d is only permitted when the electric field within the material is uniform. This is assumed to be the case for MDMO-PPV based diodes. If a sufficient amount of mobile charge carriers is present in the conjugated polymer film, the electric field can be screened already close to the electrode, hence leaving most of the bulk field free. Poly(3-hexylthiophene) (P3HT) is a conjugated polymer becoming p-doped upon exposure to oxygen [19, 20] and/or moisture [21]. The acceptor species diffuse into the polymer abstracting electrons from the π-electron system and leave behind mobile positive charge carriers. Diodes based on these doped organic semiconductors are studied by Impedance spectroscopy.

1.3.3 π-conjugated polymers doped with an electron acceptor species

The two π-conjugated polymers presented above exhibit an interesting feature of this class of materials which is electroluminescence. For this the effects governing the injection of charge carriers are important parameters. Another process that was demonstrated in organic semiconductor based devices is the photovoltaic (PV) effect. The energy alignment of the contact is most important in this case to allow the extraction of the photo-generated charge carriers. As photoexcitation leads to bound electron-hole pairs (excitons), the charge generation efficiency in pristine conjugated polymers is generally small [32]. For efficient exciton dissociation, these materials are blended with electron accepting species, e.g., C_{60} buckminster fullerene [22]

Figure 1.2: Scheme depicting the relevant energy levels of ITO - PE-DOT:PSS - MDMO-PPV - Au devices under short circuit conditions (a) and increasing applied reverse bias (b) - (c). The rigid bands of the MDMO-PPV indicate a homogeneous electric field inside the device. This electric field is determined by $(-V_{dc} - V_{int})$, the applied (negative) bias V_{dc} corrected by V_{int}. Interface effects are not included in the scheme.

7

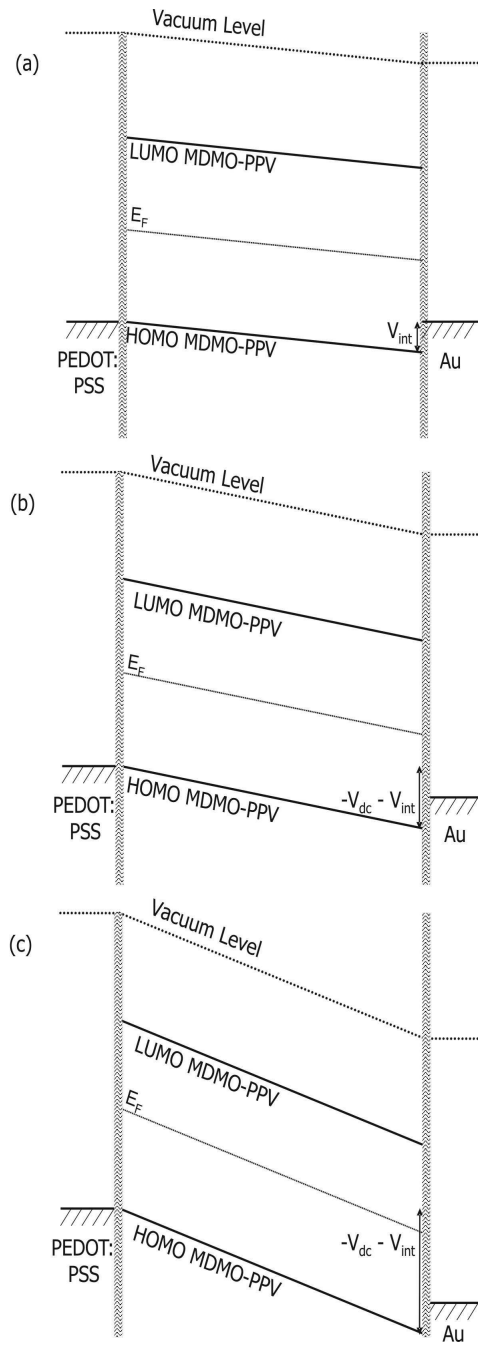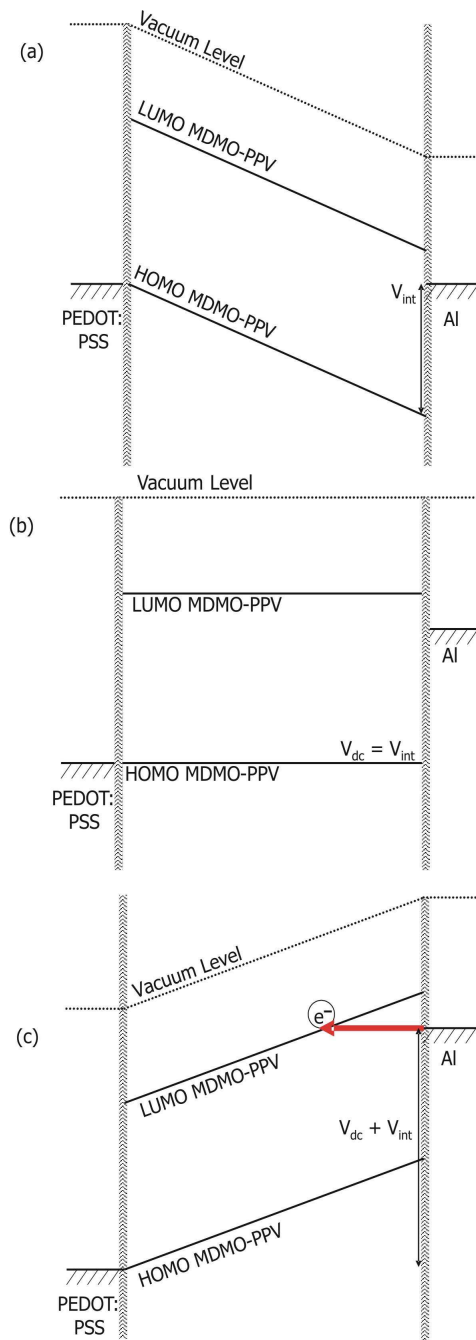Figure 1.3: Scheme depicting the relevant energy levels of ITO - PE-DOT:PSS - MDMO-PPV - Al devices under short circuit conditions (a), flat-band conditions (b) and forward bias (c). The rigid bands of the MDMO-PPV indicate a homogeneous electric field inside the device. A triangular barrier for electron injection is schematically depicted in (c). Interface effects are not included in the scheme.

or its more soluble derivatives. The difference in the electron affinities of the two components has to be large enough to overcome the exciton binding energy in the polymer and the Coulomb correlations. Although the MIM picture proved successful in providing significant insight in the physical behavior of the conjugated polymer based devices shown above, its applicability for solar cells based on donor/acceptor blends remains under debate [33]. Applying the framework of the MIM picture to PV devices, the difference in the work functions of the electrodes governs the maximum photovoltage deliverable by the device. If no other loss mechanisms are involved, the open circuit voltage (V_{OC}) could hence reach V_{int}. An alternative model [34, 35] suggests that the offset between the HOMO of the polymer and the LUMO of the acceptor indicates the upper limit for V_{OC} created in such a device. This offset in energy levels enables efficient charge generation, due to the ultra-fast charge transfer from the LUMO of the conjugated polymer to the LUMO of the electron acceptor [22]. On the other hand it also introduces a loss mechanism to the device as V_{OC} is reduced [36]. This has been identified as a major limiting factor of the power conversion efficiency shown by organic photovoltaic devices [7, 37]. Hence, the strength of the internal electric field (V_{int}/d, d is the thickness of the photoactive layer) and its influence on the photovoltaic performance of organic bulk heterojunction solar cells are still under discussion. Electroabsorption spectroscopy was performed to determine V_{int} for thin film devices based on pristine MDMO-PPV and its blend with PCBM, both with the same electrodes: ITO/PEDOT:PSS and LiF/Al. The relevant energy levels of the pristine polymer device are schematically depicted in Fig. 1.4 and those of the MDMO-PPV/PCBM mixture in Fig. 1.5.

The diodes based on donor/acceptor blends contained only highly diluted acceptor concentrations of 1% (MDMO-PPV:PCBM = 100:1 (w/w)). This recipe does not yield efficient solar cells - to reach the highest efficiency for this material combination, the MDMO-PPV/PCBM ratio is 1:4 (w/w) [23]. With the low amount of only 1% no percolated network of PCBM is expected between the electrodes. This is necessary to keep the conductivity of the active layer low hence ruling out disturbing effects due to undesirable current flow in the device. Unlike the conjugated polymers, C_{60} and its derivative used here (PCBM) show a distinctly different behavior of its conductivity as a function of temperature [38]. While pristine MDMO-PPV

9

Figure 1.4: Scheme depicting the relevant energy levels of ITO - PE-DOT:PSS - MDMO-PPV - LiF/Al devices under flat band (left) and short circuit conditions (right). Interface effects are not included in the scheme. Due to our experiments, an almst ohmic contact between MDMO-PPV and LiF/Al is assumed.
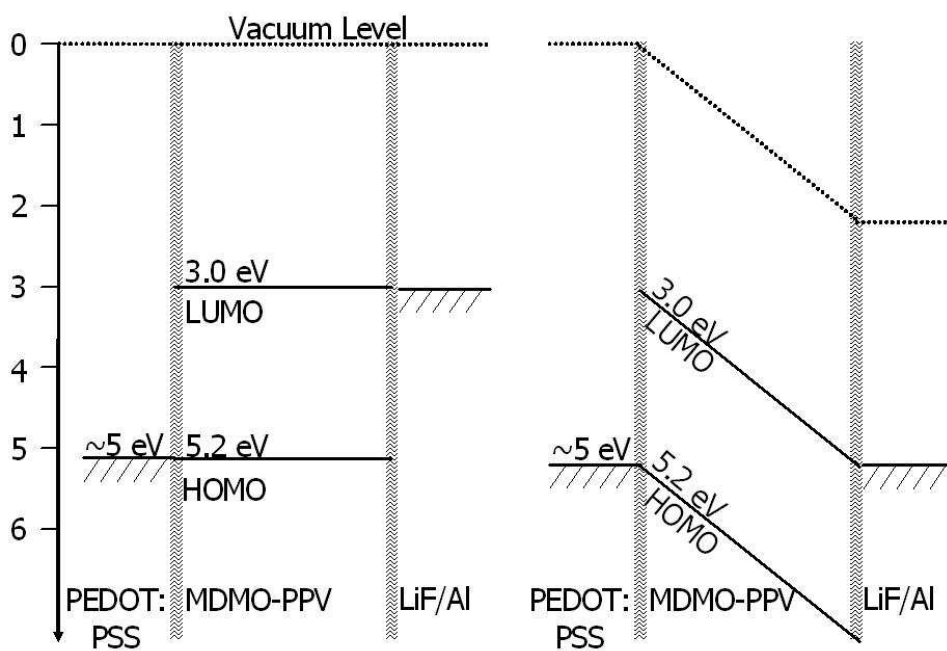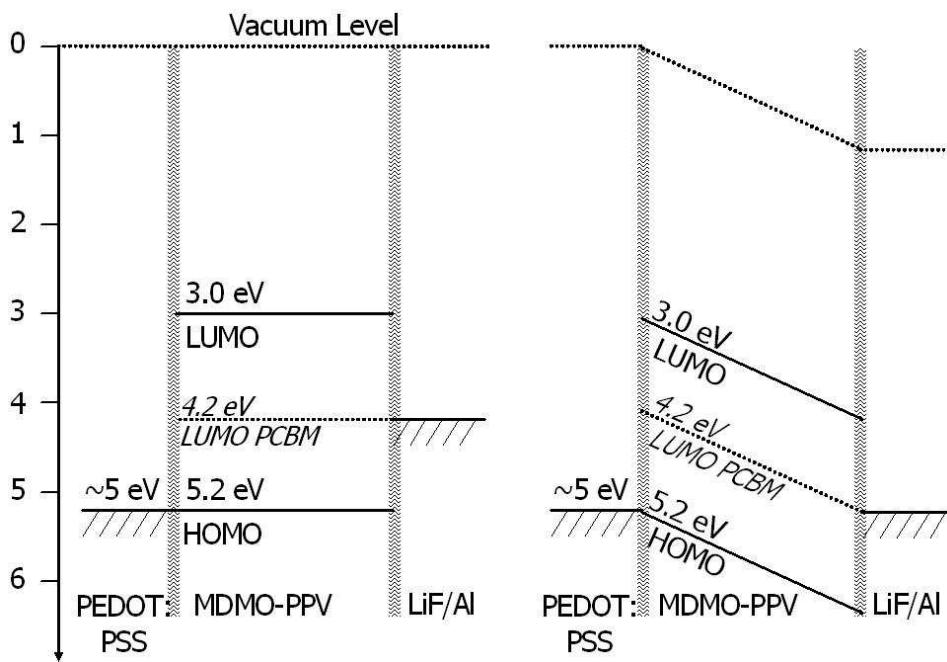
Figure 1.5: Scheme depicting the relevant energy levels of ITO - PE-DOT:PSS - MDMO-PPV/PCBM - LiF/Al devices under flat band (left) and short circuit conditions (right). Interface effects are not included in the scheme. Due to our experiments, an ohmic contact between PCBM and LiF/Al is assumed.

acts as electrical insulator at the measuring temperature of EA (≈ 100 K), C_{60} does not lose its conductive properties.

1.4 Impedance spectroscopy on polymer semiconductor thin film devices

In the MDMO-PPV and P3HT based thin film devices presented above, ohmic contact for holes from the interface with ITO or ITO/PEDOT:PSS is expected. Upon using these hole injecting electrodes, the electrical properties of the devices are largely influenced by the metal top electrode. Its work function is an important parameter for the electron injection into the organic semiconductor layer. In the studied devices the difference between the semiconductor bandgap and V_{int} gives a qualitative estimation for the chance for bipolar injection, i. e. the injection of both electrons and holes. The presence of both types of carriers in the film is the prerequisite for their radiative recombination and therefore electroluminescence, one of the desired and valuable properties of many π-conjugated polymers such as MDMO-PPV and P3HT [39].

MDMO-PPV based diodes with Au, Al and LiF/Al top electrodes as well as doped ITO - P3HT - Al devices are studied with Impedance spectroscopy. This technique is very versatile, as a frequency range over several orders of magnitude (in this case 20 Hz - 1 MHz) is experimentally accessible. It therefore allows to distinguish between phenomena on various time scales. The approach to measure the impedance of conjugated polymer based diode structures is significantly different from the study of Metal-Insulator-Semiconductor (MIS) devices. Whereas in the MIS structures based on organic semiconductors and dielectrics accumulated charges at the semiconductor/insulator interface are of primary interest (e.g. [40]), in the diodes it is desired to study features related to charge injection, transport and recombination in the bulk of the organic semiconductor.

Generally, the impedance of a device is defined as

$$\frac{v_{ac}(\omega)}{i_{ac}(\omega)} \equiv Z(\omega) = ReZ + i\,ImZ \ , \tag{1.3}$$

where v_{ac} and i_{ac} are the applied voltage and the measured current, respectively. $Z(\omega)$ is the frequency dependent complex impedance, with ReZ

and ImZ being its real and imaginary components. The modulus of the impedance $|Z|$ is hence defined as

$$|Z| = \sqrt{ReZ^2 + ImZ^2} \tag{1.4}$$

and its phase θ is derived using

$$tan\theta = \frac{ImZ}{ReZ} \ . \tag{1.5}$$

The impedance Z is related to the admittance Y via

$$\frac{1}{Z(\omega)} \equiv \frac{i_{ac}(\omega)}{v_{ac}(\omega)} \equiv Y(\omega) = ReY + i\ ImY \ , \tag{1.6}$$

The simplest equivalent circuit to describe a diode is a resistance (R_p) and a capacitance (C_p) in parallel. Hence the admittance can be expressed as:

$$Y(\omega) = \frac{1}{R_p} + i\omega C_p \tag{1.7}$$

1.4.1 Space charge limited current

While the MIM picture together with the proposed Fowler-Nordheim tunneling mechanism [29] gives a reasonable description of the onset of charge injection, it fails to correctly describe the current through the device under injection bias. In PPV based diodes the actual currents turned out to be significantly smaller than expected due to Fowler-Nordheim tunneling [41]. Therefore it was concluded that the tunneling injection mechanism does not limit the current through the device. Charge transport was identified as the limiting mechanism and the diode characteristics could be described accurately in the well established framework of space charge limited current (SCLC) (e.g. [16]).

1.4.2 Stationary single carrier space charge limited current

Ohmic contacts to space charge limited devices yield nonlinear current - voltage curves as with increasing voltage both the electric field across the semiconductor as well as the injected free carrier concentration become larger. The general description of the single carrier dc current density J is given by

Ohm's law

$$J = en(E)\mu_{dc}E \;, \tag{1.8}$$

where e is the elementary charge (for electrons or holes), n is the number of mobile charge carriers, μ_{dc} is the respective charge carrier drift mobility and E is the electric field strength. As long as the amount of thermally generated free charges is small compared to the number of charge carriers injected from the electrodes, it may be neglected and n represents only the injected charges. This approximation is justified for most organic semiconductors, where the band-gap is in the order of 2 eV and impurities rather introduce traps than acting as a source of mobile charges [8]. The relation between the total number of charge carriers and the electric field is described by the Poisson equation

$$n(x) = \frac{\varepsilon\varepsilon_0}{q}\frac{dE}{dx} \;, \tag{1.9}$$

where ε_0 is the permittivity of free space and ε the relative permittivity of the semiconductor. Plugging Eq. (1.9) into Eq. (1.8) yields the differential equation

$$J = \varepsilon\varepsilon_0\mu_{dc}E(x)\frac{dE}{dx} \;, \tag{1.10}$$

which is solved under the boundary condition $E(x=0)=0$ by

$$E(x) = \sqrt{\frac{2J}{\varepsilon\varepsilon_0\mu_{dc}}\,x}. \tag{1.11}$$

From integrating the electric field (Eq. (1.11)) from the injecting $x=0$ to the extracting electrode $x=d$ the voltage $V(x)$ is obtained:

$$V(x) = \int_0^d E(x)\,dx = \sqrt{\frac{8J}{9\varepsilon\varepsilon_0\mu_{dc}}}\,x^{3/2} \;. \tag{1.12}$$

Taking $x=d$ and $V=V(x=d)$, the current density - voltage relation

$$J = \frac{9}{8}\varepsilon\varepsilon_0\mu_{dc}\frac{V^2}{d^3} \;, \tag{1.13}$$

is obtained in the form of the famous Mott-Gurney square law, also known as Child's law for solids [16]. Combining Eq. (1.13) with Eq. (1.11) allows to describe the electric field strength between the electrodes

$$E(x) = \frac{3V}{2d}\sqrt{\frac{x}{d}} \ .$$

(1.14)

Knowing the electric field inside the semiconductor film allows to determine the interelectrode transit time of the charge carriers. The speed of the moving charges $v(x)$ depends on their mobility μ_{dc} and the electric field $E(x)$ inside the semiconductor and is described by

$$v(x) = \mu_{dc}E(x) \ .$$

(1.15)

Hence the transit time τ_{tr} can be determined by

$$\tau_{tr} = \int_0^L \frac{1}{v(x)} \ dx = \frac{1}{\mu_{dc}} \int_0^d \frac{1}{E(x)} \ dx \ .$$

(1.16)

The electric field $E(x)$ is described by Eq. (1.14), which can be plugged into Eq. (1.16). After integration the following relation between the transit time and the charge carrier mobility is established:

$$\tau_{tr} = \frac{4d^2}{3\mu_{dc}V} \ .$$

(1.17)

In the case of asymmetric electrodes an electric field is present across the semiconductor even when no external bias is applied. This internal electric field has to be overcome in order to inject charges into the device. Hence the externally applied bias has to be corrected by this V_{int}. Equation (1.17) is therefore transformed into:

$$\tau_{tr} = \frac{4d^2}{3\mu_{dc}(V - V_{int})} \ .$$

(1.18)

1.4.3 Modeling the admittance of trap-free space charge limited current diodes

In order to describe SCLC in the case of time dependent electric fields (e.g. alternating current), a displacement term should be added to Ohm's law

introduced above Eq. (1.8). The current density is then given by:

$$J(t) = qn(x,t)\mu E(x,t) + \varepsilon\varepsilon_0 \frac{\partial E(x,t)}{\partial t} \ , \tag{1.19}$$

where μ is assumed to be field and time independent. However, to allow for a possible change in the mobility, a normalized, dimensionless mobility is introduced:

$$\tilde{\mu} = \frac{\mu(\omega)}{\mu_{dc}} \ , \tag{1.20}$$

where $\mu(\omega)$ is the frequency dependent mobility and μ_{dc} is the dc mobility introduced above. If there are no traps in the semiconductor $\tilde{\mu} = 1$.

For single carrier SCLC devices theoretical descriptions of the capacitance are available from the Sixties and Seventies. Shao et al. [42] and Kassing [43] introduced a model for the dynamic, hence frequency dependent admittance $Y(\omega)$ of perfect single carrier space charge limited devices without traps. For the derivation the small signal approximation is used, i.e. a small ac voltage is superimposed on a large dc bias. The applied voltage is hence expressed by

$$V(x,t) = V_{dc}(x) + v_{ac}(x,t) = V_{dc}(x) + V_{ac}(x)e^{i\omega t}, \ |v_{ac}| << |V_{dc}|. \tag{1.21}$$

According to references [43] and [42] the results for the complex admittance $Y(\omega) = i_{ac}/v_{ac}$ can be written as:

$$Y(\omega) = \frac{C_g}{2\tilde{\mu}\tau_{tr}}\{\frac{(\Omega/\tilde{\mu})^3}{i[1 - e^{-i\Omega/\tilde{\mu}}] + \Omega/\tilde{\mu} - (1/2)i(\Omega/\tilde{\mu})^2}\} =$$
$$= \frac{C_g}{2\tau_{tr}}\{\frac{\Omega^3}{i\tilde{\mu}^2[1 - e^{-i\Omega}] + \tilde{\mu}\Omega - (1/2)i\Omega^2}\} \ , \tag{1.22}$$

with $\tilde{\mu} = 1$ for trap-free SCLC. For $\tilde{\mu} = 1$ we can separate into real and imaginary part:

$$Y(\omega) = \frac{C_g}{2\tau_{tr}}\Omega^3\{\frac{\Omega - sin\Omega}{(\Omega - sin\Omega)^2 + (1 - cos\Omega - \Omega^2/2)^2} + i\frac{\Omega^2/2 + cos\Omega - 1}{(\Omega - sin\Omega)^2 + (1 - cos\Omega - \Omega^2/2)^2}\}, \tag{1.23}$$

where $\Omega = \omega\tau_{tr}$ is a "normalized frequency" and $C_g = \varepsilon A/d$ is the geometric capacitance. Defining the dynamic conductance $G(\omega)$ and capacitance $C(\omega)$

by:

$$Y(\omega) = G(\omega) + i\omega C(\omega) \ , \tag{1.24}$$

we get:

$$G(\omega) = (G_0/6)\Omega^3 \{ \frac{\Omega - sin\Omega}{(\Omega - sin\Omega)^2 + (1 - cos\Omega - \Omega^2/2)^2} \} \ , \tag{1.25}$$

with $G_0 = G(0) = 3C_g/\tau_{tr} = 9\varepsilon\mu AV/4d^3$.

$$C(\omega) = (C_g/2)\Omega^2 \{ \frac{\Omega^2/2 + cos\Omega - 1}{(\Omega - sin\Omega)^2 + (1 - cos\Omega - \Omega^2/2)^2} \} \ . \tag{1.26}$$

At low frequencies, $\Omega \ll 1$, $G(\omega)$ approaches G_0 and $C(\omega)$ approaches $(3/4)C_g$. At high frequencies, $\Omega \gg 1$, $G(\omega) = (2/3)G_0$ and $C(\omega) = C_g$: Therefore, the sample can be represented at low and high frequencies by an equivalent circuit of a resistance (R_p) and a capacitance (C_p) in parallel, with:

$$R_p = G_0^{-1}; \quad C_p = (3/4)C_g; \quad \text{at} \quad \omega\tau_{tr} \ll 1$$
$$R_p = (3/2)G_0^{-1}; \quad C_p = C_g; \quad \text{at} \quad \omega\tau_{tr} \gg 1 \ . \tag{1.27}$$

Figure 1.6 shows a simulation of conductance G (Eq. (1.25)) and capacitance C (Eq. (1.26)) for trap-free single carrier SCLC in a diode. The important parameter governing both contributions to the admittance is the transit time τ_{tr} of the injected charge carriers (Eqs. (1.25) and (1.26)). In trap-free single carrier SCLC samples the transit time effect caused by the charge carriers moving from one electrode to the other is identified as the only influence on the the admittance [44]. The transitions observed in C and G are hence determined to take place at frequencies around $(\tau_{tr})^{-1}$. The low frequency values of C and G are affected by these transit time effects as the charge carriers can be injected and leave the device in the same half period of the ac voltage. v_{ac} can inject additional charge carriers which for frequencies $f < (\tau_{tr})^{-1}$ cause additional current. At higher frequencies the other contact cannot be reached in this time frame, the conductance decreases and the capacitance increases, finally reaching the geometric capacitance.
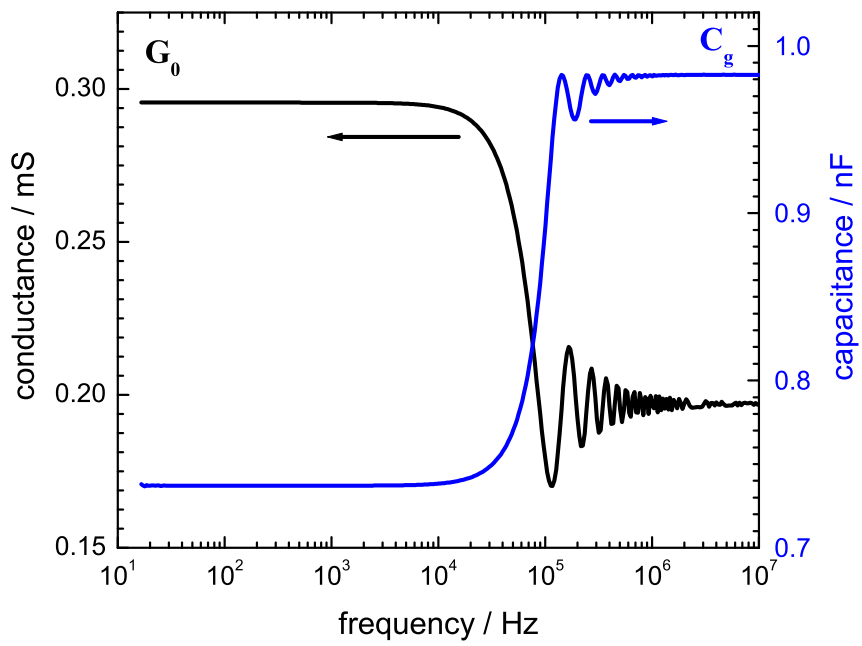
Figure 1.6: Simulated capacitance and conductance for trap-free single carrier space charge limited devices according to references [43] and [42] performed by Eitan Ehrenfreund.

1.4.4 Modeling the admittance of space charge limited current diodes with dispersive transport

The model of Shao and Kassing describes the admittance of trap-free SCLC diodes by Eq. (1.23), where the transit time of the charge carriers is the only effect on the admittance. This situation is certainly unrealistic for PPV based diodes, where the presence of traps for charge carriers induces dispersive transport (e.g. [45, 46, 47]). Traps capture and re-emit charge carriers, hence introducing relaxation processes. These add an additional frequency dependence to the admittance. Kassing [43] added one defined impurity trap level to his model for trap-free SCLC diodes described above. However, this modification is not sufficient to mimic the behavior of diodes based on conjugated polymers. A more general attempt to include traps was suggested by Martens et al. [48]. Whereas Kassing and Shao chose a constant charge carrier drift mobility in their calculations, Martens et al. introduced a normalized dimensionless mobility $\tilde{\mu}$ of the form

$$\tilde{\mu}(\omega) = \frac{\mu(\omega)}{\mu_{dc}} = 1 + M(i\omega\tau_{tr})^{1-\gamma} \; , \tag{1.28}$$

which is frequency dependent. The mobility μ is hence a function of frequency, normalized to the zero frequency (dc) mobility μ_{dc}. τ_{tr} is again the charge carrier transit time, M is a proportionality constant and γ is the dispersion coefficient [48]. M and γ are parameters determining the dispersivity of the charge transport. A large M indicates pronounced disorder, whereas $M = 0$ describes the trap-free case. γ can take up values between 0 and 1. A small exponent $(1 - \gamma)$ in Eq. (1.28), hence a γ close to 1 reflects non-dispersive and a small γ highly dispersive transport. From the resulting admittance

$$Y(\omega) = \frac{C_g}{2\tau_{tr}} \{ \frac{(\omega\tau_{tr})^3}{i\tilde{\mu}^2[1 - e^{-i\omega\tau_{tr}}] + \tilde{\mu}\omega\tau_{tr} - (1/2)i(\omega\tau_{tr})^2} \} \; , \tag{1.29}$$

the capacitance is extracted as $C(\omega) = ImY/\omega$. Simulations of the capacitance according to Eq. (1.29) are presented in Fig. 1.7. The parameters in this simulation are a dispersion coefficient $\gamma = 0.5$ and various values for the proportionality factor M ranging from 0 (trap-free case) to 0.3.
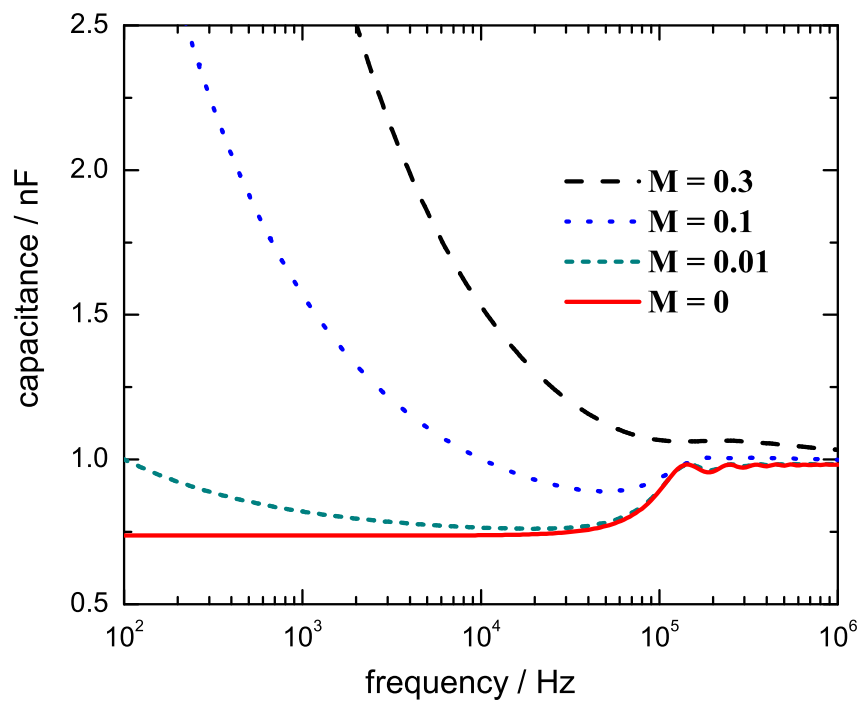
Figure 1.7: Simulated capacitance for single carrier space charge limited devices taking into account dispersive transport. According to reference [48], simulation performed by Eitan Ehrenfreund.

1.4.5 Single carrier drift mobility extracted from impedance measurements

As the simulation depicted in Fig. 1.7. shows, dispersive transport makes it difficult to determine the transit time of the charge carriers from admittance data. Whereas in the trap-free case (Fig. 1.6) a pronounced step indicates the transit of the injected charges, traps only allow to observe a depression (Fig. 1.7) when capacitance is plotted as a function of the frequency. As the transit time depends on the voltages, the position of this depression shifts as the applied bias is changed. It moves to higher frequencies with increasing forward bias. Such features have already been observed and described in the literature [49, 50, 51, 48, 44] and have been attributed to space charge limited current [16, 43, 52, 53, 54, 55]. By fitting experimental admittance data to Eq. (1.29), the transit time of the injected charges can be determined for single carrier space charge limited devices. Using Eq. (1.18) and hence taking into account V_{int} allows to determine the mobility of the charges. This procedure can be done directly with Eq. (1.29) using the relation $Y = G(\omega) + i\omega C$ when the used computer software can handle complex numbers (e.g. MATLAB). For other cases (e.g. ORIGIN), the actual separation into real and imaginary part is necessary, as the explicit expressions are needed. In the following the explicit expressions for computation of the real and imaginary parts are written. As a first step the dimensionless quantity

$$\bar{Y} = (2\tau_t/\Omega^3 C_g)Y(\Omega) \tag{1.30}$$

is introduced. Furthermore:

$$\gamma = 1 - \alpha$$
$$p = 2M\omega^\gamma sin(\pi\gamma/2) + M^2\omega^{2\gamma} sin(\pi\gamma)$$
$$q = 1 + 2M\omega^\gamma cos(\pi\gamma/2) + M^2\omega^{2\gamma} cos(\pi\gamma)$$
$$r = (1 + M\omega^\gamma cos(\pi\gamma/2))^2 + M^2\omega^{2\gamma} sin^2(\pi\gamma/2)$$
$$s = M\omega^{1+\gamma} sin(\pi\gamma/2)/r$$
$$v = \omega(1 + M\omega^\gamma cos(\pi\gamma/2)$$
$$u = v/r$$
$$n = M\omega^{1+\gamma} sin(\pi\gamma/2) - \omega^2/2$$
$$g = -p(1 - e^{-s}cos(u)) - qe^{-s}sin(u) + v$$
$$h = -q(1 - e^{-s}cos(u) + pe^{-s}sin(u) - n \qquad (1.31)$$

With these notations, one gets:

$$\bar{Y}^{-1} = g - ih$$
$$\bar{Y} = g/(g^2 + h^2) + ih/(g^2 + h^2) \qquad (1.32)$$

and the admittance

$$Y(\omega) = (C_g\omega^3/2\tau_t)[\frac{g}{g^2 + h^2} + i\frac{h}{g^2 + h^2}] \qquad (1.33)$$

The conductance is:

$$G(\omega) = ReY = (C_g\omega^3/2\tau_t)\frac{g}{g^2 + h^2} \qquad (1.34)$$

and the capacitance:

$$C(\omega) = ImY/\omega = (C_g/2)\frac{\omega^2 h}{g^2 + h^2} \qquad (1.35)$$

Chapter 2

Experimental

2.1 Device preparation

2.1.1 Substrate preparation

The organic semiconductor thin film devices studied herein were prepared in sandwich geometry. Substrates for these devices were 1.5 cm × 1.5 cm large glass sheets covered with indium tin oxide (ITO, purchased from Merck, Inc.). To ensure secure connection of the metal top electrode without risking the connector tip to punch through the metal layer and shortcut to the ITO, part of the ITO was removed by chemical wet etching. This was done by exposing the surface to a strong acid (HCl $_{conc.}$: HNO$_3$ $_{conc.}$: H$_2$O = 4.6 : 0.4 : 5) for 20 minutes. The part where ITO should remain was coated with scotch tape to protect it from the acid. For thorough cleaning the substrates subsequently underwent 20 minutes in a basic glass cleaning agent ("Hellmanex"). The remaining Hellmanex was removed with deionized water in an ultrasonic bath. After drying, the substrates were covered with PEDOT:PSS or the organic semiconductor layer, depending on the desired device structure.

2.1.2 Materials

PEDOT:PSS as intermediate layer

Poly(3,4-ethylenedioxythiophene) doped with poly(styrenesulfonate) (in the following abbreviated as PEDOT:PSS, purchased from Bayer AG as BAYTRON-PH) was spin coated onto the ITO. The chemical structure is given in Fig.
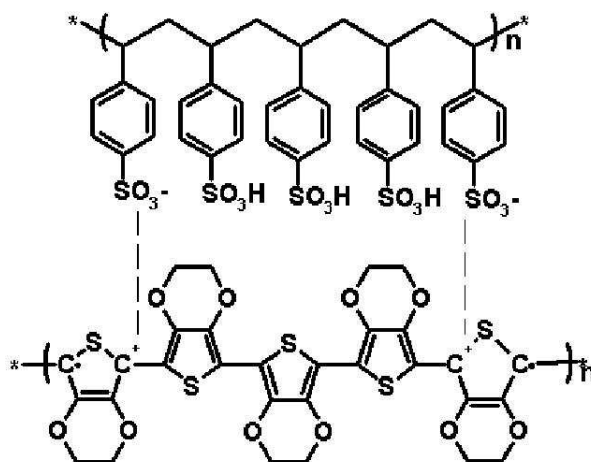
Figure 2.1: Chemical structure of poly(3,4-ethylenedioxythiophene) and poly(styrenesulfonate), PEDOT:PSS.
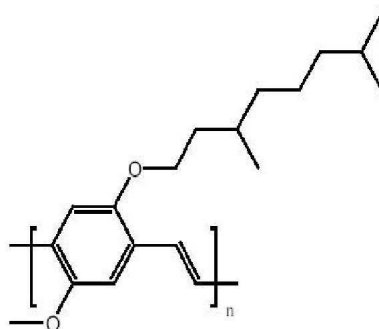
Figure 2.2: Chemical structure of poly[2-methoxy-5-(3',7'-dimethyloctyloxy)-1-4-phenylene vinylene], MDMO-PPV.

2.1. For the spin coating process a program was used, where the sample holder is accelerated with a ramp time of 4 s to 1500 rpm and kept at that rotational speed for 40 s. Subsequently the samples underwent 20 s of rotation with 2000 rpm. The coated devices were dried under vacuum over night, prior to further thin film deposition.

π-conjugated polymers: MDMO-PPV and P3HT

Active layers made from poly[2-methoxy-5-(3',7'-dimethyloctyloxy)-1-4-phenylene vinylene] (MDMO-PPV) were spin cast from a solution in chlorobenzene. The chemical structure is illustrated in Fig. 2.2. Films of regioregular
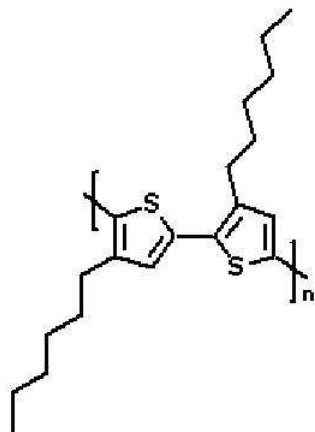
Figure 2.3: Chemical structure of regioregular poly(3-hexylthiophene-2,5-diyl), P3HT.

poly(3-hexylthiophene-2,5-diyl) (P3HT, purchased from Rieke, Inc.) were prepared from a solution in chloroform using the doctor blade technique.

Buckminster fullerene C_{60} and PCBM

Layers of Buckminster Fullerene C_{60} were applied by thermal evaporation on ITO/PEDOT:PSS covered glass substrates. Its more soluble derivative (1-(3-methoxycarbonyl)propyl-1-phenyl [6,6]C 61) (PCBM, purchased from
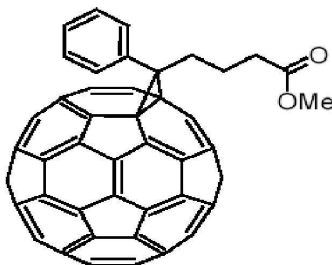
Figure 2.4: Chemical structure of (1-(3-methoxycarbonyl)propyl-1-phenyl [6,6]C 61), PCBM, a soluble derivative of Buckminster fullerene C_{60}.

Nano-C, Inc. The chemical structure is illustrated in Fig. 2.4) was employed as an electron acceptor in blends with MDMO-PPV. The mixtures of both materials were cast from their solution in chlorobenzene.

2.1.3 Evaporation of the top electrodes

The top electrodes were applied by thermal deposition through a shadow mask in vacuum better than 10^{-5} mbar. Tungsten boats were used as source. Three different contacts were applied for the devices studied herein: Au, Al and LiF/Al. For the first two, layers of around 70 nm were deposited directly onto the semiconductor films. In the case of LiF/Al electrodes, first LiF was applied by evaporating a nominally 0.6 nm thick layer of the salt directly onto the organic film, afterwards covered by approximately 70 nm Al. Thin interfacial layers of LiF are known to improve electron injection from the Al into the typical π-conjugated polymers such as PPVs.

2.2 Experimental methods

2.2.1 Electroabsorption spectroscopy

The method of Electroabsorption (EA) makes use of the Stark effect: An electric field acting on a conjugated polymer sandwiched between two electrodes, induces a change in the absorption of the film [56]. By measuring the electric field induced change in the transmission, information on this field inside the device can be gained.

The first harmonic EA response is described by

$$\frac{|\Delta T|}{T}(h\nu) \;\propto\; (V_{dc} - V_{int}) \cdot V_{ac} \;, \tag{2.1}$$

where $\Delta T/T$ is the normalized electric field induced change in the transmission, V_{dc} the externally applied dc bias and V_{ac} the ac amplitude. V_{int} is the potential difference induced by asymmetric contacts.

The homemade electroabsorption setup (Fig. 2.5) used for the experiments is operated in absorption/reflection geometry [24]. Hence, after passing through the device once, the probe light beam is reflected at the back electrode and passes through the film a second time. As light source a Xe lamp is used, powered by a very stable power supply (SVX 1530/LAX 1530 from
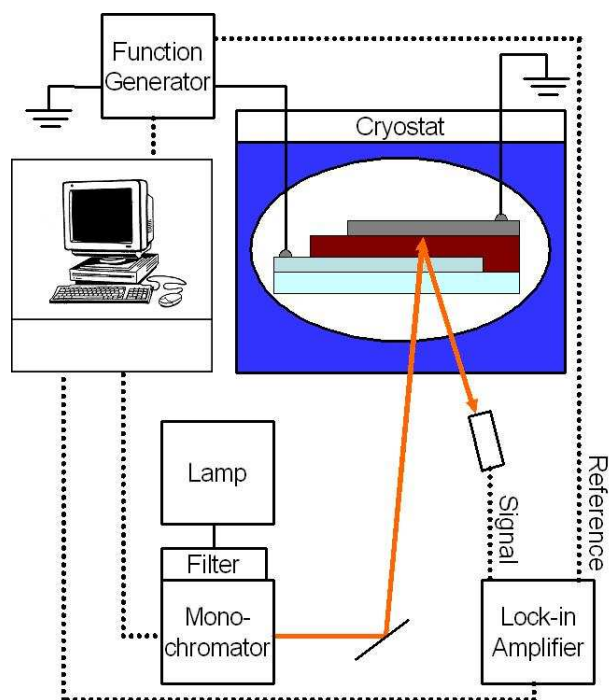
Figure 2.5: Experimental setup to measure Electroabsorption in reflection/absorption geometry.
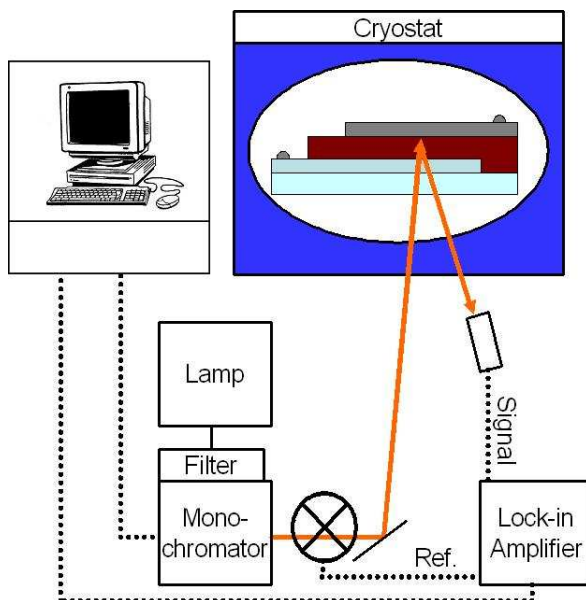

Figure 2.6: Experimental setup to measure transmission features in organic semiconductor thin film devices.

Müller GmbH Elektronik-Optik). Before entering the monochromator (Acton Research SP-150, 150 g/mm grating, with an 500 nm blaze) the light beam passes through a filter, cutting off wavelengths below 450 nm. The entrance and exit slits are opened by 0.3 mm, a good compromise delivering sufficient light intensity with a spectral resolution better than 5 nm. Via a system of three lenses and a mirror for precision alignment, the probe beam is focused onto the active area of the sample inside the cryostat (Oxford Instruments Optistat DN-V), where it is mounted on a cold finger. The cryostat can be filled with liquid nitrogen. It is therefore possible to cool the devices to about 77 K. The reflection coming from the Al back electrode is collected by a lens and focused on a Si-photo diode, delivering a signal proportional to the incoming light intensity to the lock-in amplifier (Stanford Research Systems SRS 830).

A combined dc and dc voltage produced by the function generator (Stanford Research Systems DS345) is applied across the sample, connecting the + to the ITO and the – to the Al. A reference signal of the same frequency and phase is delivered to the lock-in amplifier.

If no voltage is applied and instead a chopper wheel is set up in front of the monochromator exit slit, the signal coming from the detector is proportional to the double path transmission at that wavelength (Fig. 2.6). It can be read out from the lock-in if referenced to the chopping frequency. For every measured wavelength the EA response is normalized to this signal to get rid of the spectral response due to the characteristics of the setup.

These characteristics include the intensity distribution of the lamp, the performance of the monochromator and the sensitivity of the detector.

2.2.2   Electroluminescence measurements

Recombination of positive and negative charge carriers in MDMO-PPV leads to the emission of visible light. This electroluminescence is measured with the setup depicted in Fig. 2.7. A combined ac and dc voltage is applied by a function generator (Stanford Research Systems DS345) to the device. The lock-in amplifier is referenced to the ac voltage hence measuring the light emission induced by the applied bias.
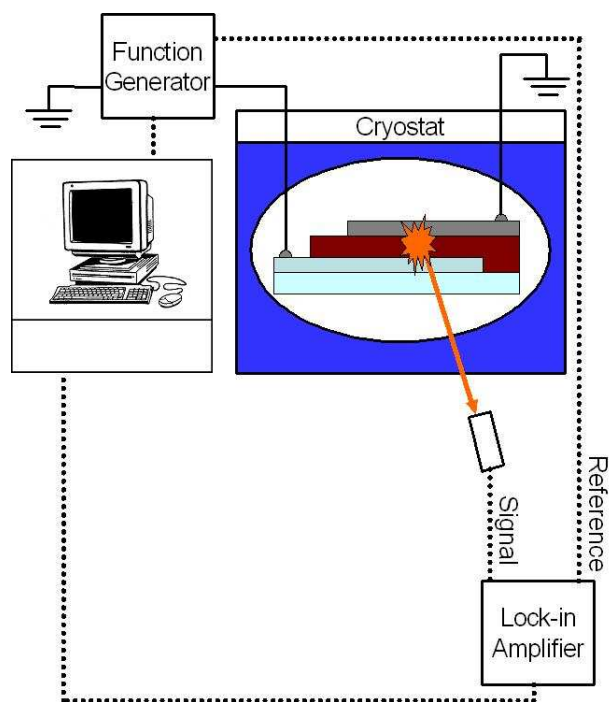
Figure 2.7: Experimental setup to measure the electroluminescence of organic semiconductor thin film devices.
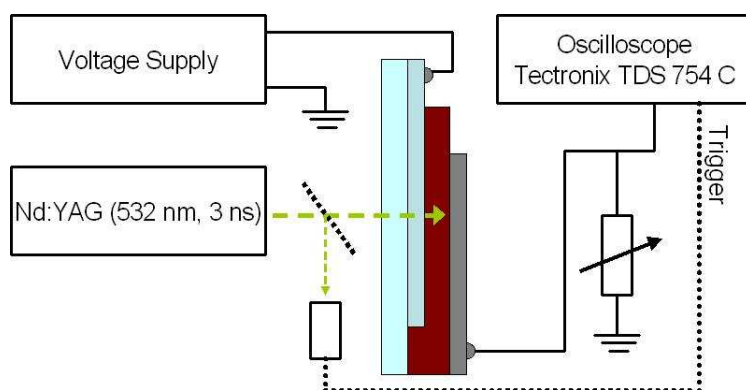
Figure 2.8: Experimental setup to measure the transient photocurrent under externally applied bias in organic semiconductor thin film devices.

2.2.3   Transient photocurrent measurements

The photovoltaic performance of the devices is studied with transient photocurrent measurements under applied bias (Fig. 2.8). Pulsed laser excitation (3 ns) using the 532 nm line of a neodymium doped yttrium aluminum garnet laser (Nd:YAG) was employed. Due to its high amount of photons delivered over a short period of time, deterioration of the sample is avoided. By using filters of various optical densities we observed that 0.3 mJ pulses saturate V_{OC} sufficiently long for the measurements. The laser pulse induced transient photocurrents were recorded on devices biased by an external voltage offset. The photogenerated charge carriers are extracted by the overall dc bias present in the semiconducting layer. Therefore, when this electric field is compensated externally, i.e., flat-band conditions are established, the created charge carriers cannot leave the device and recombine inside the photoactive layer. This compensation voltage is referred to as V_{BI} in the following [7]. The transients were recorded by a Tektronix TDS754C oscilloscope, the offset voltage applied by an Agilent 33250 A function generator.

Chapter 3

Results and discussion

3.1 The internal electric field in organic semiconductor thin film devices

In this section, the internal electric field of ITO - PEDOT:PSS - MDMO-PPV devices with various metal top electrodes is studied.

3.1.1 Slightly doped π-conjugated polymers

Figures 3.1 and 3.2 show the normalized electric field induced change in transmission (first harmonic Electroabsorption (EA) response) measured on a typical ITO - PEDOT:PSS - MDMO-PPV - Au device. The EA spectra displayed in Fig. 3.1 scale with the applied bias as expected from Eq. (2.1):

$$\frac{|\Delta T|}{T}(h\nu) \;\propto\; (V_{dc} - V_{int}) \cdot V_{ac} \;.$$

Figure 3.2 shows the EA response at the peak maximum (590 nm). Over the whole observed voltage range between -4 V and +4 V the electric field induced signal exhibits its predicted linearity with the dc voltage. The EA signal can be canceled by an externally applied dc voltage (V_{dc}). According to Eq. (2.1), this is the case for $V_{dc} = V_{int}$, hence determining V_{int} as +0.7 V from Fig. 3.2. This value does not fit the nominal work function mismatch illustrated in Fig. 1.1, from which hardly any potential offset is expected. On the other hand a V_{int} of +0.7 V supports the observed asymmetric current density - voltage (J-V) characteristics shown in Fig. 3.3. The rectification ratio at $+/-$ 6 V is appreciable, exceeding two orders of magnitude. The

Figure 3.1: First harmonic Electroabsorption spectra of a typical ITO - PE-
DOT:PSS - MDMO-PPV - Au device taken at various applied dc voltages.
Measurements performed at $\approx$ 100 K, 1 V ac amplitude.

Figure 3.2: First harmonic Electroabsorption data of a typical ITO - PE-DOT:PSS - MDMO-PPV - Au device at various applied bias voltages taken at 590 nm. Measurements performed at $\approx$ 100 K, 1 V ac amplitude.

Figure 3.3: Current density - voltage characteristic of a typical ITO - PE-DOT:PSS - MDMO-PPV - Au device at room temperature (130 nm active layer thickness).
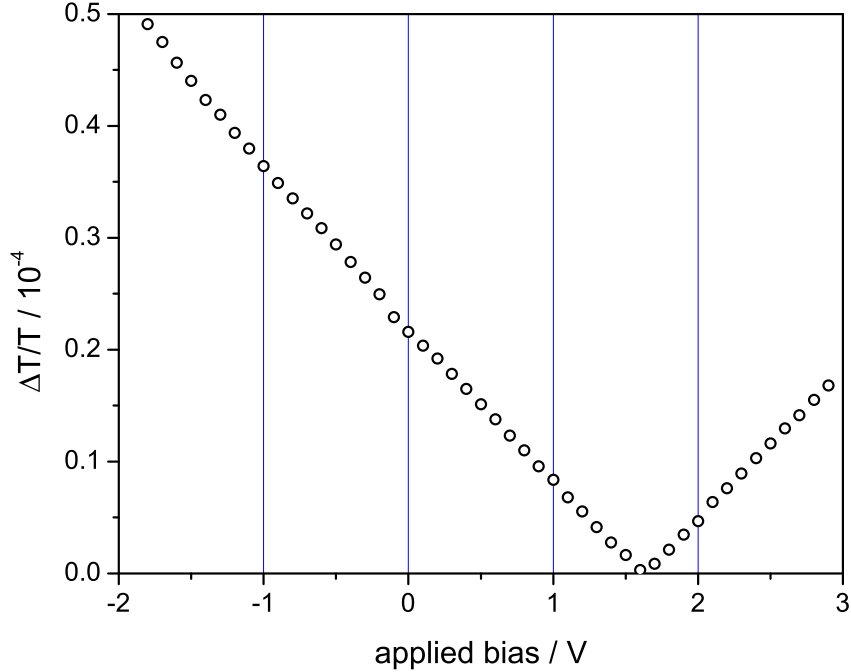
Figure 3.4: First harmonic Electroabsorption data of a typical ITO - PE-DOT:PSS - MDMO-PPV - Al device at various applied bias voltages taken at 590 nm. Measurements performed at $\approx$ 100 K, 1 V ac amplitude.

value of +0.7 V is still small as compared to the bandgap of MDMO-PPV ($\approx$ 2.1 eV optical and $\approx$ 2.3 eV electrochemical [57]). Therefore a large barrier towards electron injection and hence dominant hole current is expected in this device for sufficiently low applied bias.

Figure 3.5 displays the J-V characteristic at room temperature of a typical ITO - PEDOT:PSS - MDMO-PPV - Al diode with an active layer thickness of 130 nm. Figure 3.4 illustrates the determination of V_{int} for the same kind of device with EA measured at low temperatures. The peak maximum is around 590 nm. It is hence located at the same position as for Au electrodes because the spectrum is determined by the MDMO-PPV. By this method, V_{int} is measured to be +1.6 V.

Figures 3.6 and 3.7 show the J-V characteristics and the EA response measured on ITO - PEDOT:PSS - MDMO-PPV - LiF/Al device structures, respectively. Just as in the cases of Au and Al electrodes described above,
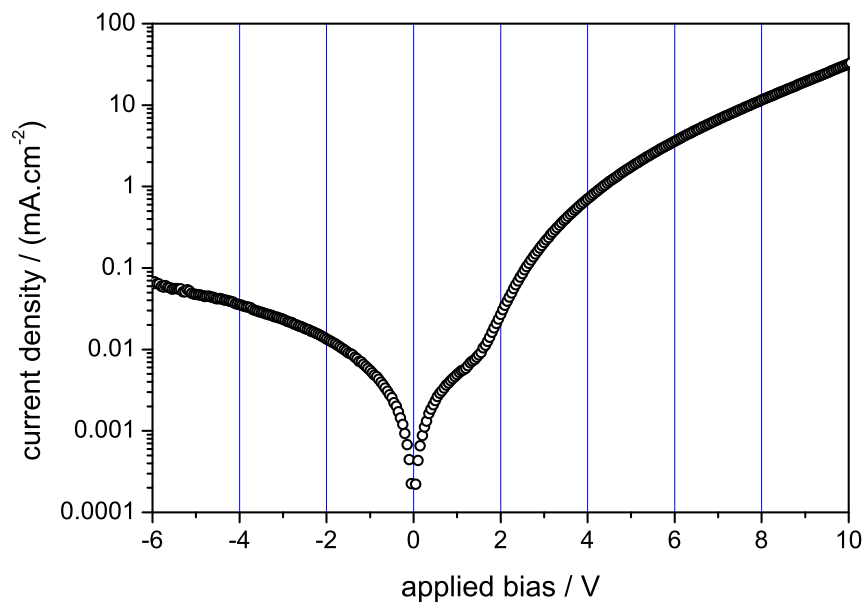
Figure 3.5: Current density - voltage characteristic of a typical ITO - PE-DOT:PSS - MDMO-PPV - Al device at room temperature (130 nm active layer thickness).
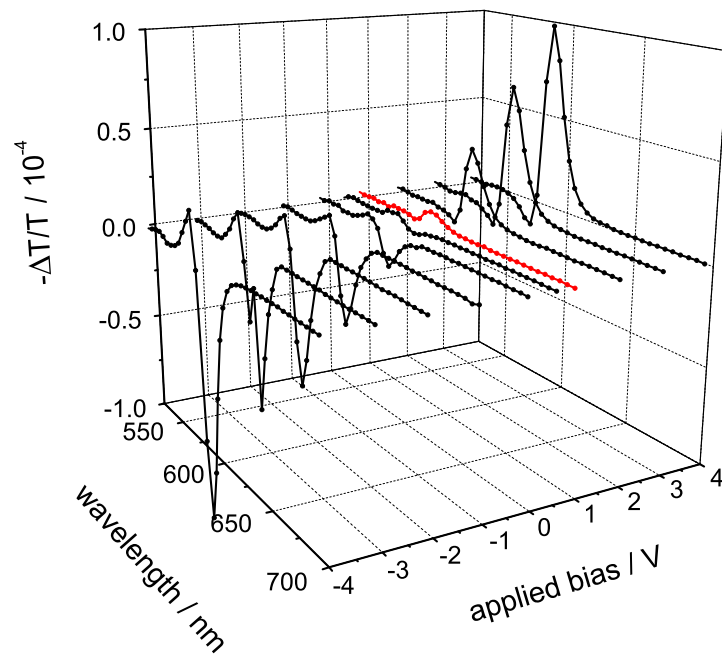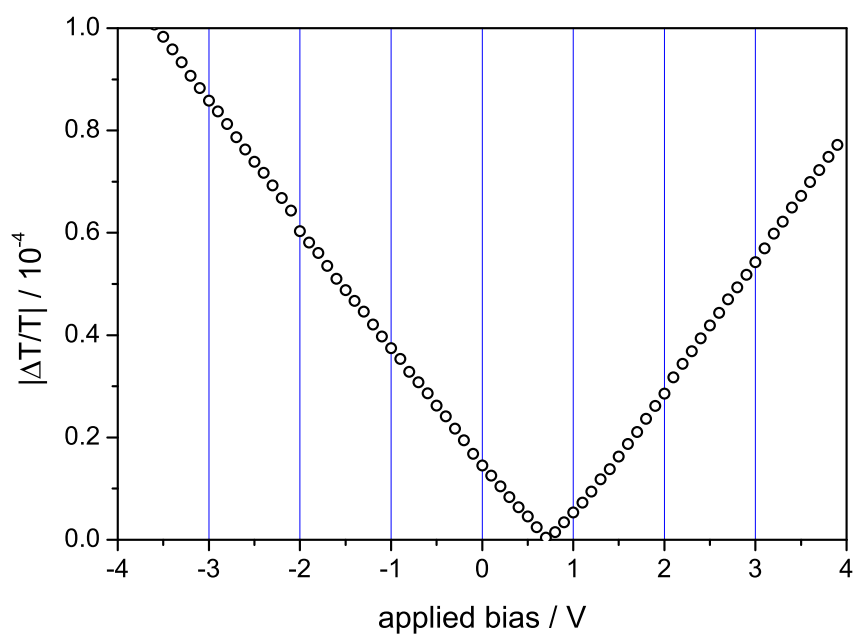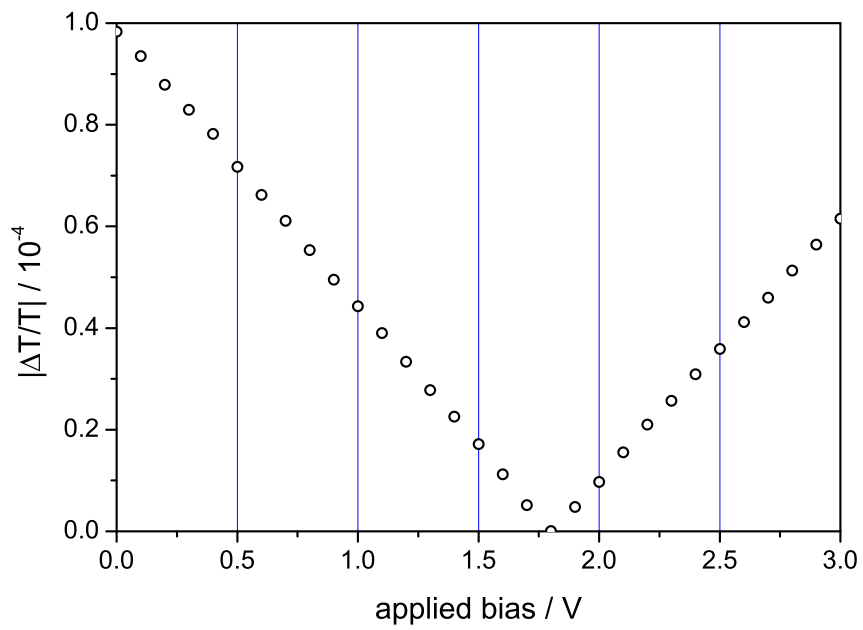
Figure 3.6: First harmonic Electroabsorption data of a typical ITO - PE-DOT:PSS - MDMO-PPV - LiF/Al device at various applied bias voltages taken at 590 nm. Measurements performed at $\approx$ 100 K, 1 V ac amplitude.
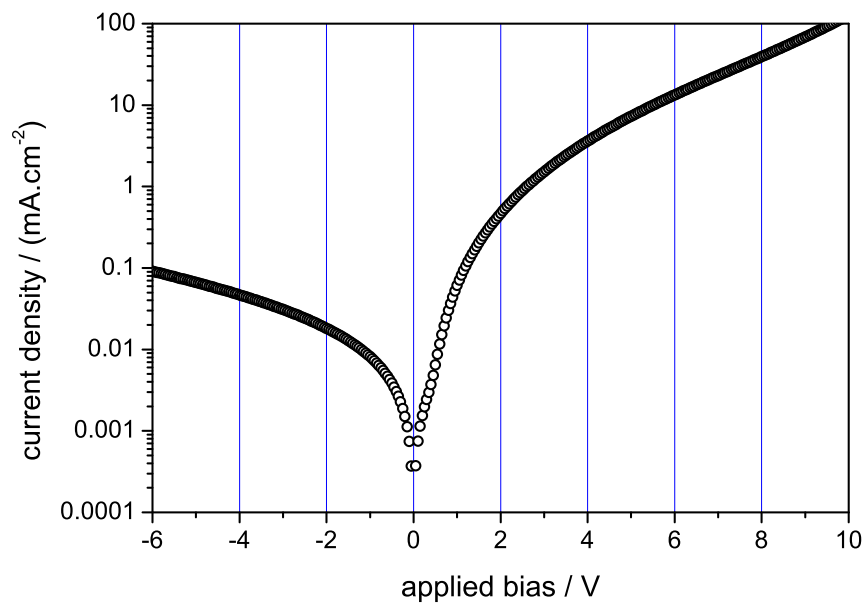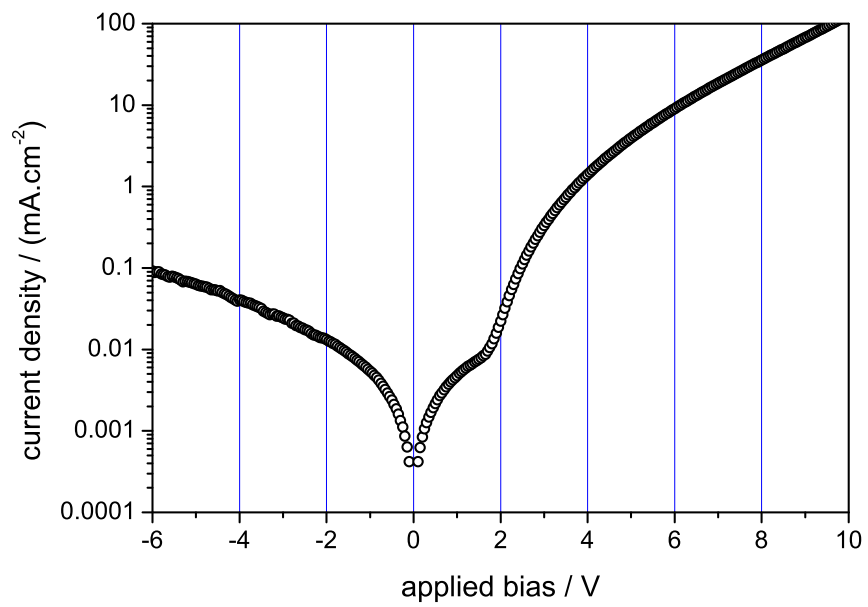
Figure 3.7: Current density - voltage characteristic of a typical ITO - PE-DOT:PSS - MDMO-PPV - LiF/Al device at room temperature (130 nm active layer thickness).
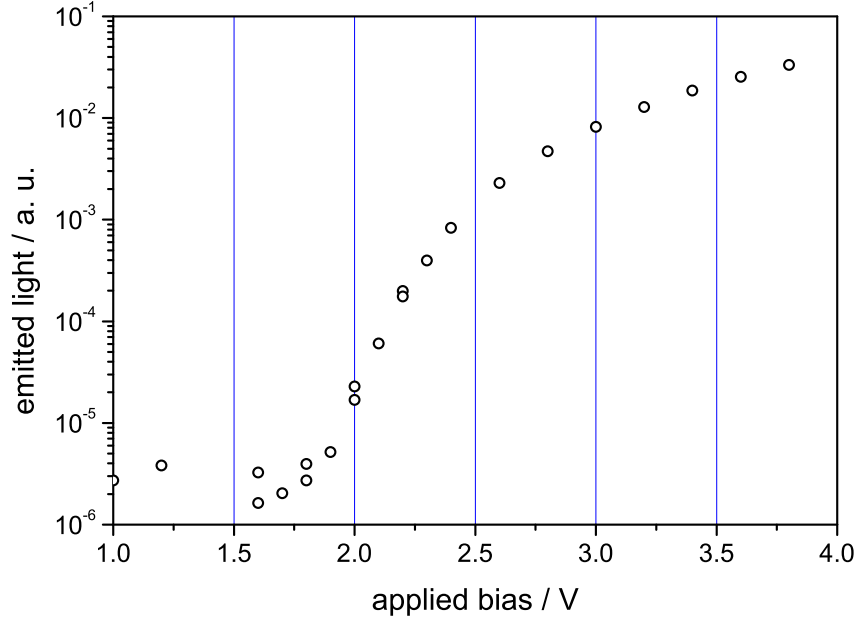
Figure 3.8: Electroluminescence response of a typical ITO - PEDOT:PSS - MDMO-PPV - LiF/Al device at room temperature (80 nm active layer thickness).

the electrical characterization was performed on a 130 nm thick diode at room temperature, whereas the EA response was measured at approximately 100 K. For LiF/Al top electrodes, V_{int} is determined to be +1.8 V. Figure 3.8 illustrates electroluminescence measurements performed on ITO - PEDOT:PSS - MDMO-PPV - LiF/Al devices at room temperature. The onset of light emission is determined for applied voltages just below +2 V. Hence the bias necessary to turn on light emission in the device closely corresponds to V_{int} measured with EA (Fig. 3.6) and the bandgap of MDMO-PPV [57]. This correlation is interpreted in terms of an almost ohmic contact between ITO/PEDOT:PSS and MDMO-PPV on one side [7, 58] and LiF/Al on the other side [18].

The data on the pristine MDMO-PPV films shown in Figs. 3.1 to 3.6 can be meaningfully interpreted in terms of a MIM picture [29]. Though not resembling the nominal work function mismatch between the electrode materials,

V_{int} can be shifted from +0.7 V (Au) up to +1.8 V by using LiF/Al top electrodes. The energetic offset between the work functions of the metals and the energy levels of the organic material is only a first approximation for the energy barrier towards charge injection. Explanations for the deviation between the work function difference of the electrode materials and the actual V_{int} determined by EA spectroscopy are suggested in various publications: The work functions of the pure metals are usually determined in ultra-high vacuum by photoelectron spectroscopy, while the energy levels in organic molecules are measured by cyclic voltammetry in solution. The preparation method of the organic semiconductor thin film devices presented herein was not clean enough to exclude the oxidation of the metal electrodes or the formation of adsorbate layers. Also chemical reactions are possibly taking place between the polymer film and the metals that would form an interfacial layer with properties deviating from those of the bulk [59, 60, 8]. Nevertheless, it has to be pointed out that upon changing the top electrode material from Au to Al, V_{int} changes from +0.7 V to +1.6 V. The work functions attributed to these metals are 4.3 eV and 5.1 eV respectively [24]. Hence the change in V_{int} is 0.9 V and therefore very close to the difference in the work functions (0.8 V).

3.1.2 Intentionally doped π-conjugated polymers

Expressing the internal electric field under short circuit conditions as V_{int}/d is only permitted when the electric field within the material is homogeneous. This is assumed to be the case for MDMO-PPV based diodes. If a sufficient amount of mobile charge carriers is present in the conjugated polymer film, the electric field can be screened already close to the electrode, hence leaving most of the bulk field free. Poly(3-hexylthiophene) (P3HT) is a conjugated polymer becoming p-doped upon exposure to oxygen [19, 20] and/or moisture [21]. Thin film devices based on organic semiconductors resemble parallel plate capacitors with the low mobility conjugated polymers as dielectric. The capacitance C displayed in Fig. 3.9 is extracted from the admittance Y measured on the device according to $C = ImY/\omega$. Figure 3.9 shows the evolution of the capacitance C of a P3HT based device as a function of voltage during the exposure to atmosphere. As can be seen in Fig. 3.9, the capacitance increases with time as long as it is ex-
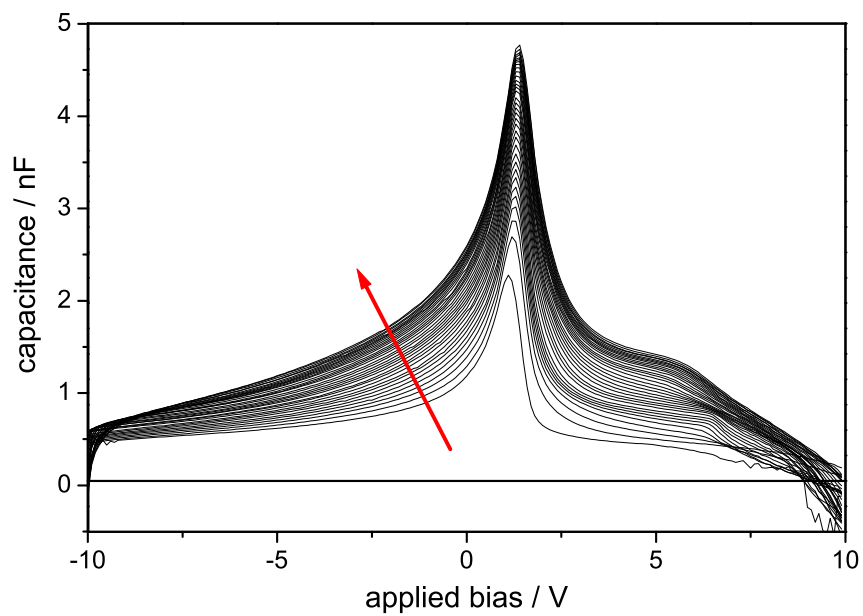
Figure 3.9: Evolution of the capacitance of an ITO - P3HT - Al device with an active layer thickness of roughly 1 μm in air. One sweep measured every second minute after removing the sample from inert atmosphere. The arrow indicates increasing exposure times. Measurements performed at room temperature. 200 mV ac amplitude, 1 kHz.

posed to atmosphere. The sweeps from -10 V to +10 V show a C increasing with voltage, peaking between +1.2 V and +1.5 V. At higher bias, the capacitance decreases abruptly. Around +8 V the measured C reaches zero, eventually turning negative as the bias is increased further. The growing capacitance with time is interpreted as an indication of the ongoing doping procedure [61]. In the case of a Schottky contact, $1/C^2$ evolves linearly with the voltage, according to [62, 63, 64]

$$1/C^2 = \frac{2(V_{dc} - V_{int})}{A^2 q \varepsilon \varepsilon_0 N_A} \; , \qquad (3.1)$$

where V_{dc} is the externally applied dc voltage, A is the active surface area of the device, q is the charge of the impurities, ε is the relative dielectric constant of the semiconductor, ε_0 is the permittivity of vacuum, and N_A is the concentration of acceptor impurities. Figure 3.10 shows the experimental results for the capacitance C from Fig. 3.9 in the form of $1/C^2$ versus applied dc bias. As can be seen in this plot, the experimental data for intermediate times follow a straight line over a wide range of voltage and doping level. Extrapolation of the linear regime yields a zero crossing at approximately + 1.2 V. According to Eq. (3.1) this voltage is equal to V_{int}, hence being a method to determine the potential offset between the electrodes in doped thin film devices where the electric field is pronouncedly nonuniform [61]. The experimental data gained from P3HT based diodes exposed to air can be successfully described by assuming a Schottky contact, but it does not unambiguously show at which of the two contacts the barrier is expected. It has been shown in the literature that ITO can form Schottky contacts with PPV prepared by the so-called precursor route [63]. It was claimed that the reason for this is the diffusion of InCl$_3$ into the PPV when the precursor polymer is eliminated from the substrates [65]. As Tomozawa et al. showed that ITO forms an ohmic contact to the HOMO of P3HT [66], this possibility can be ruled out for the solution processed P3HT. On the other hand the Fermi level of Al is located almost in the middle of the polymer band gap about 1 eV above its HOMO level [67]. Therefore, this contact is expected to be Schottky like when the diode is exposed to air [62]. The scheme of the relevant energy levels of ITO - P3HT - Al devices and the Schottky contact are depicted in Fig. 3.12. Figure 3.11(a) shows the doped device under short circuit conditions. Due to the presence of
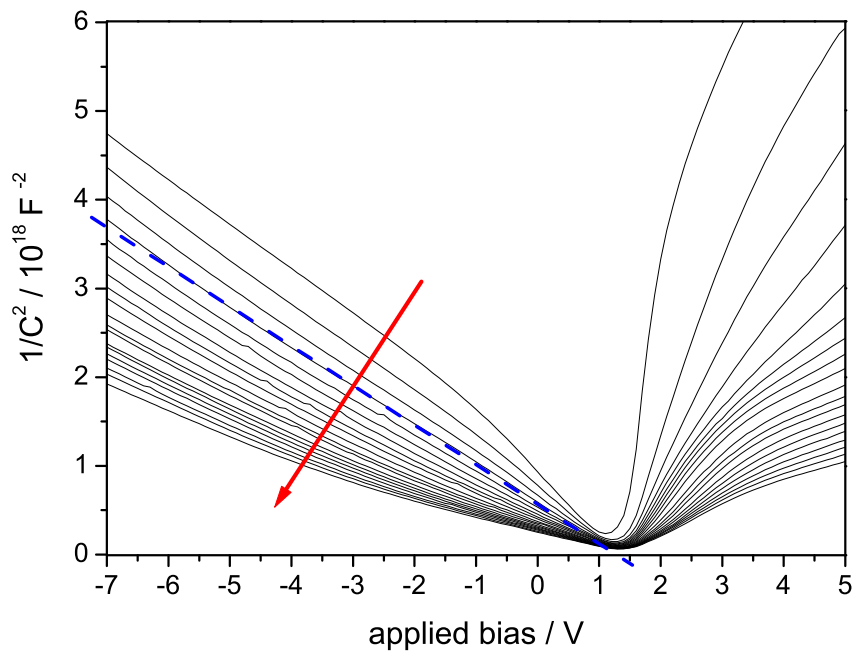
Figure 3.10: $1/C^2$ of an ITO - P3HT - Al device with an active layer thickness of roughly 1 μm in air. C is the capacitance displayed in Fig. 3.9. One sweep measured every second minute after removing the sample from inert atmosphere. The arrow indicates increasing exposure times. The dashed line is a guide to the eye indicating the linear behavior of $1/C^2$ versus applied bias. Measurements performed at room temperature. 200 mV ac amplitude, 1 kHz.
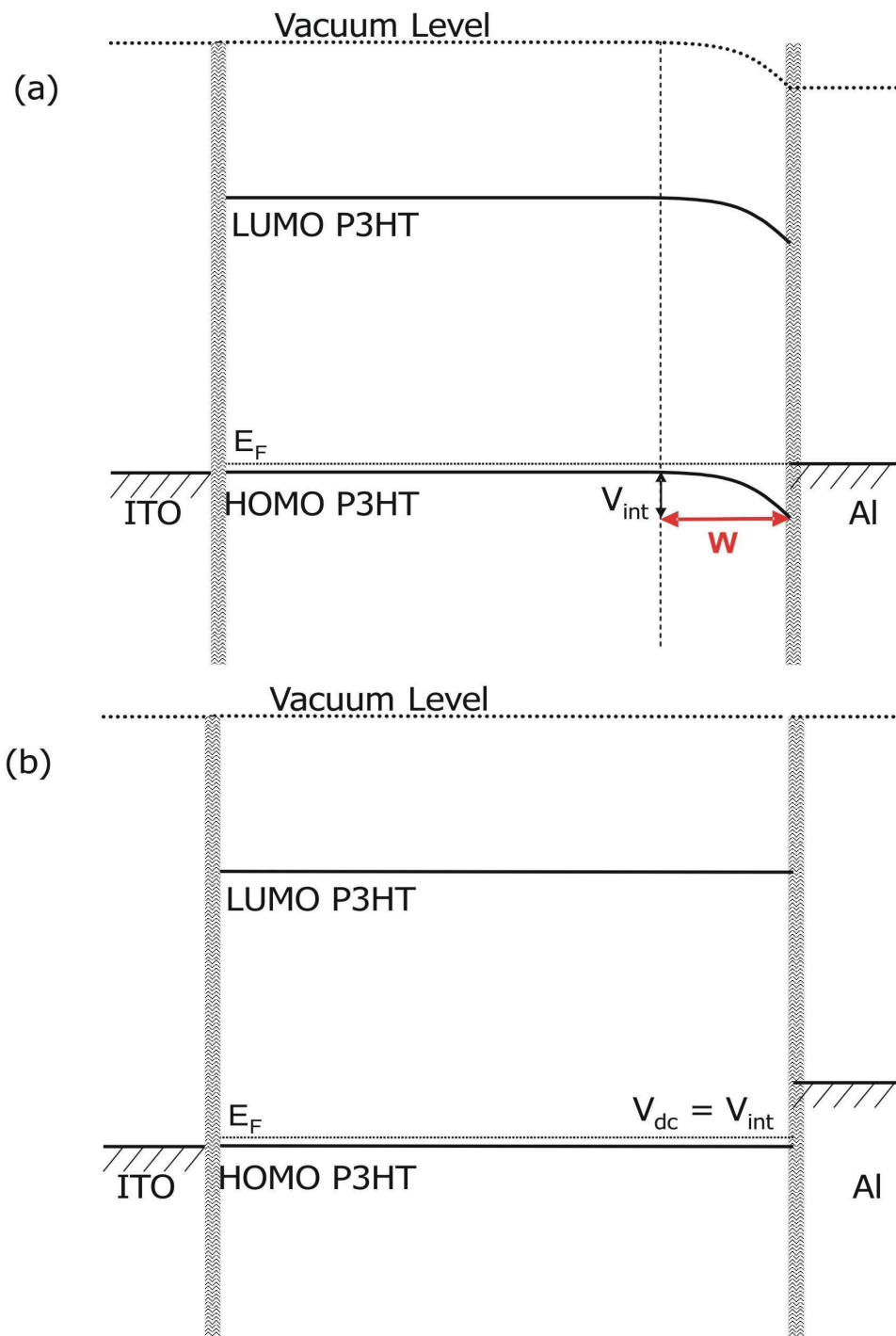
Figure 3.11: Scheme depicting the relevant energy levels of doped ITO - P3HT - Al devices under short circuit conditions (a) and flat band conditions (b).
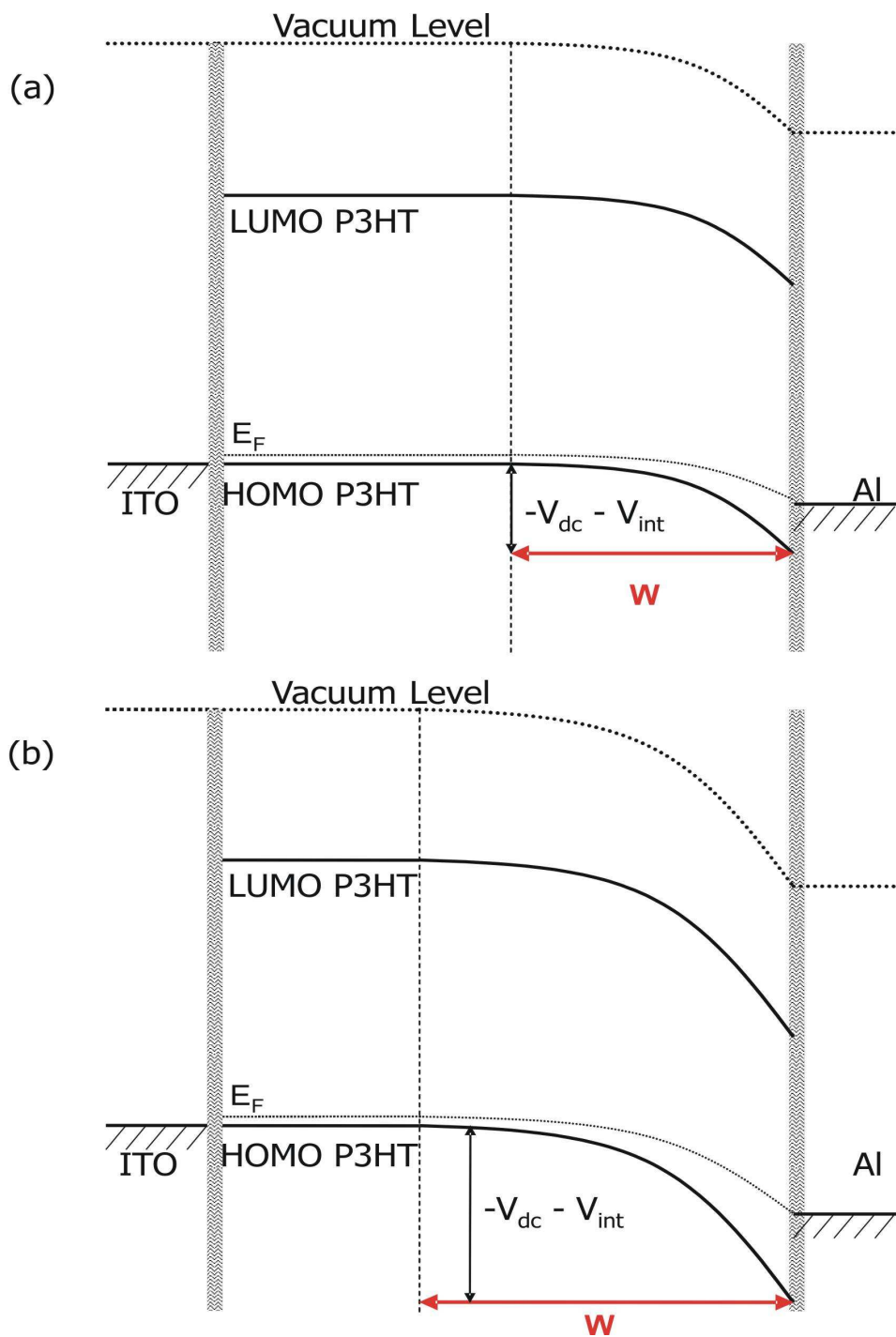
Figure 3.12: Scheme depicting the relevant energy levels of doped ITO - P3HT - Al devices under increasing applied reverse bias from (a) to (b). The electric field is already screened within the depletion zone width W leaving most of the polymer field free. $(-V_{dc} - V_{int})$ indicates the applied (negative) bias V_{dc} is corrected by V_{int}.

a significant amount of charge carriers ($N_A \approx 10^{17}$ in this case [61]), the Fermi level aligns between the doped P3HT and the Al contact. The mobile positive charges induced by the doping procedure recombine with electrons injected from the Al electrode. The remaining immobile negative charges screen V_{int} already in the vicinity of the Al contact. Figure 3.12(b) and (c) illustrate the device under reverse bias. The increasingly negative voltage cause a growing depletion zone width over which the potential drop takes place, while the rest of the P3HT film remains field free.

Contrary to their counterparts based on MDMO-PPV, which are shown to follow the MIM scheme, doped P3HT based devices behave differently due to this doping effect and are well described by assuming a Schottky contact.

3.1.3 π-conjugated polymers doped with an electron acceptor species

Figure 3.13 shows Electroabsorption measurements for thin film devices based on pristine MDMO-PPV and its blend with PCBM, both with the same electrodes: ITO - PEDOT:PSS and LiF/Al. V_{int} is measured for both types of devices. For this purpose the diodes based on donor/acceptor blends contained only highly diluted acceptor concentrations of 1% (MDMO-PPV:PCBM = 100:1 (w/w)). Though the studied devices do not resemble efficient solar cells, a clear effect due to the introduction of PCBM becomes visible from Fig. 3.13. As described above, V_{int} is given by the external dc bias necessary to cancel the EA response, around +1.2 V in the case of MDMO-PPV/PCBM blends and roughly +1.8 V for the pristine polymer (shown here again for comparison).

In Figures 3.14 and 3.15 photocurrent transients under various applied bias voltages are shown for both types of devices. As observable in Fig. 3.14, roughly +2 V have to be externally applied to cancel the photocurrent induced by the laser pulse in pristine MDMO-PPV based samples with LiF/Al electrodes. Adding PCBM to the active layer, this value is reduced to about +1.2 V (Fig. 3.15). In addition to the current response related to the bias voltage, which occurs in the time scale of several microseconds, an additional short term response (spike) immediately after the laser pulse can be seen. This feature is significantly more pronounced in the case without PCBM (Fig. 3.14). This spike is attributed to a creation of charge carriers close to the electrodes. Whereas devices based on MDMO-PPV films with
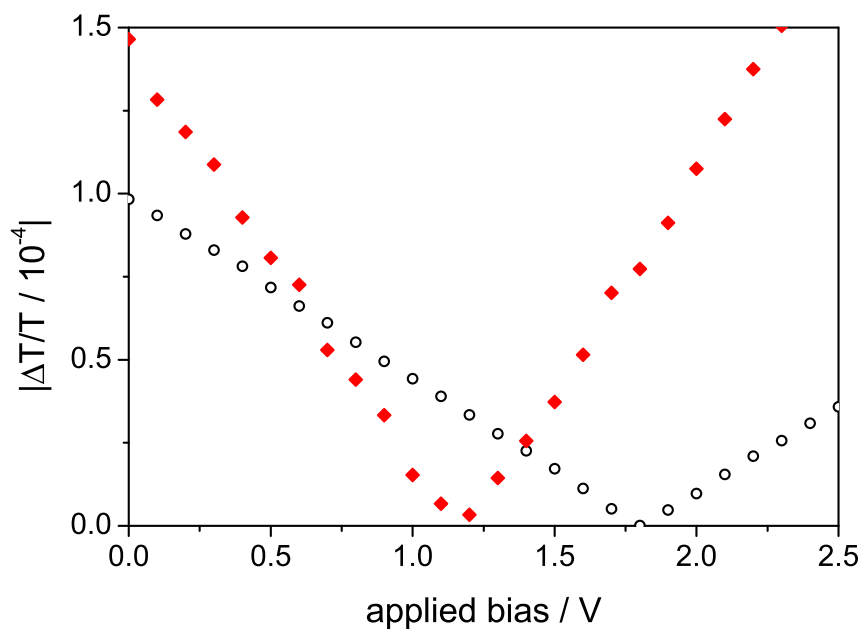
Figure 3.13: First harmonic electroabsorption response at 570 nm (100 K), ac amplitude of 1 V. The red diamonds represent ITO - PEDOT:PSS - MDMO-PPV/ PCBM (100:1) - LiF/Al and the circles represent ITO - PEDOT:PSS - MDMO-PPV - LiF/Al.
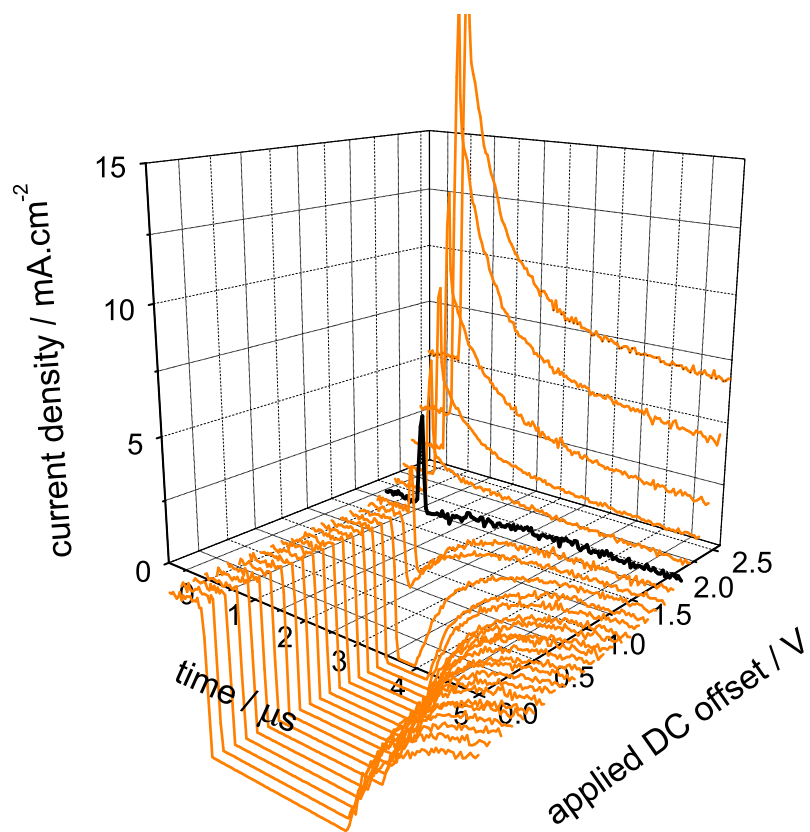
Figure 3.14: Transient photocurrents of an ITO - PEDOT:PSS - MDMO-PPV - LiF/Al device under various applied bias offsets.
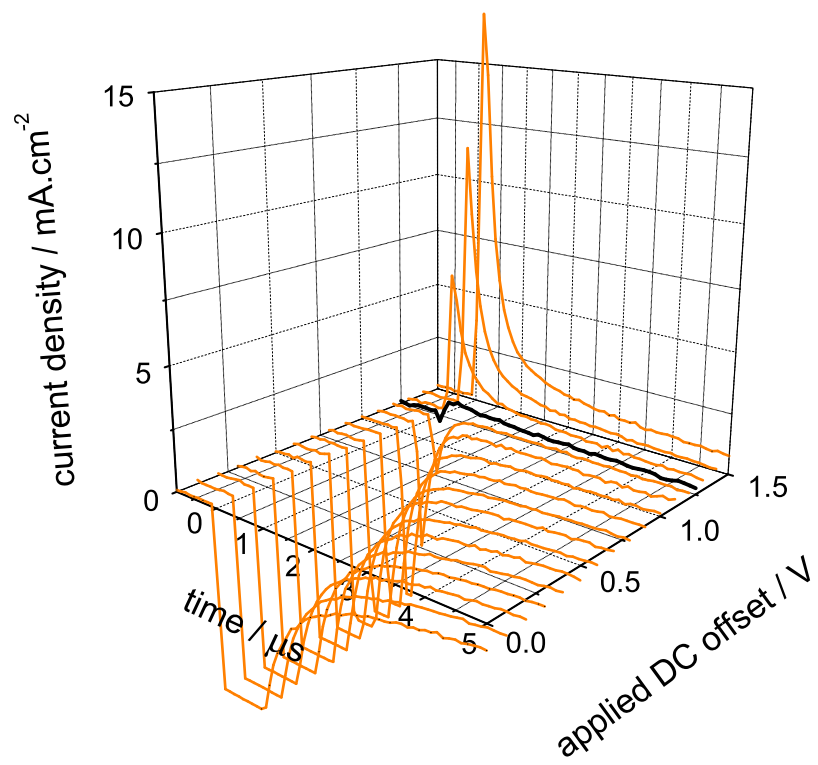
Figure 3.15: Transient photocurrents of an ITO - PEDOT:PSS - MDMO-PPV/PCBM (100:1) - LiF/Al device under various applied bias offsets.

PCBM have efficient exciton dissociation sites in the bulk, in the pristine polymer charge carriers are generated close to the electrode [68].

The photogenerated charge carriers are extracted by the overall dc bias present in the semiconducting layer. Therefore, when this electric field is compensated externally, i.e. flat-band conditions are established, the created charge carriers cannot leave the device and recombine inside the photoactive layer. For the diodes based on pure MDMO-PPV, LiF/Al top electrodes ensure good electron contact to the LUMO of the conjugated polymer. EA measurements on conjugated polymers doped with C_{60} have shown that due to electron transfer to the C_{60} the Fermi level of the low work function electrode is pinned close to the LUMO of the acceptor [69]. In the studied devices, which contain about 1% of PCBM, V_{int} is determined to be +1.2 V. Again, pinning of the Fermi level to the LUMO of PCBM is the reason for this value. By space charge limited current measurements, a V_{int} of +1 V was found for ITO - PEDOT:PSS - PCBM - LiF/Al devices [38]. The difference of 0.2 V between these pristine PCBM based devices and our results is attributed to the different matrix conditions. Energy values are sensitive to the environment and may be altered when PCBM is embedded into MDMO-PPV. According to previous work done by our group, the LUMO of PCBM is estimated to be approximately 4.3 eV [70]. Correlating V_{int} found by EA spectroscopy with transient photocurrent measurements under applied bias, the overall dc field inside the photoactive layer is identified as the driving force of the photocurrent in the solar cell [18]. The same trend is observed for the transient photocurrent measurements under applied bias.

3.2 Impedance spectroscopy on polymer semiconductor thin film devices

Figure 3.16 shows the phase θ and the modulus $|Z|$ of the impedance of an ITO - PEDOT:PSS - MDMO-PPV - LiF/Al diode as a function of voltage for an ac frequency of 10 kHz. For negative applied bias and up to approximately +2 V, both measured quantities stay remarkably constant. At voltages more positive than +2 V the phase of the impedance changes rapidly from approximately $-\pi/2$ towards zero, while at the same bias the impedance drops significantly from roughly 145 kΩ to about 10 Ω at +5 V. Comparing the impedance with the J-V characteristics of the ITO - PE-
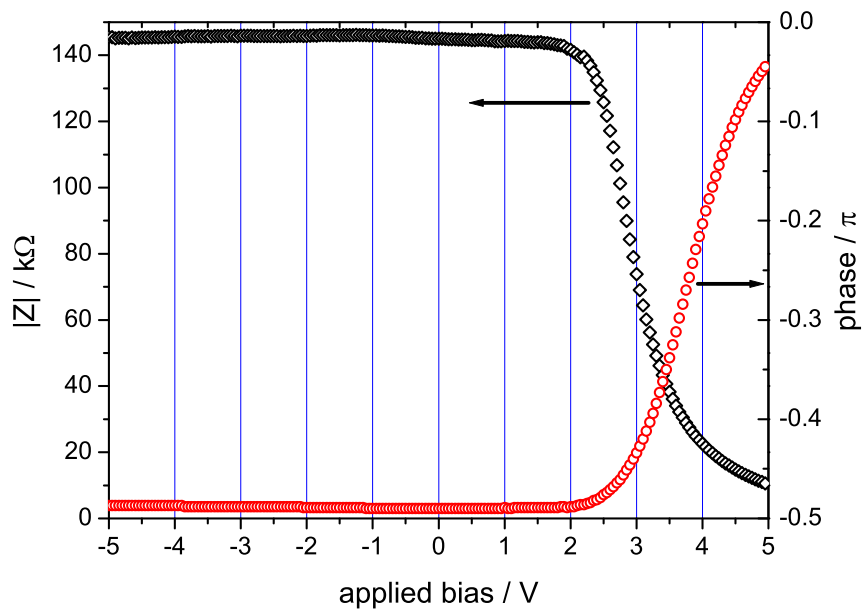
Figure 3.16: Modulus $|Z|$ and phase of the Impedance of a typical ITO - PEDOT:PSS - MDMO-PPV - LiF/Al device measured at 10 kHz. 200 mV ac amplitude.

DOT:PSS - MDMO-PPV - LiF/Al device displayed in Fig. 3.7, the voltage threshold where the impedance and its phase change corresponds to the opening of the diode. The voltage range below $+2$ V in which a constant impedance with a phase of $-\pi/2$ is observed, corresponds to the blocking regime of the diode. The modulus of the impedance is therefore large, as only a comparably small leakage current passes through the device. The remarkably constant impedance points to a negligibly low concentration of mobile charges in the MDMO-PPV and supports the observations with EA spectroscopy presented above. As the diode opens, the modulus of the impedance drops significantly, while the phase changes rapidly from $-\pi/2$ towards zero. A phase of $-\pi/2$ is the signature of a capacitor, indicating that the measured ac current i_{ac} lags behind the applied ac voltage v_{ac}. If i_{ac} is in phase with v_{ac} the device resembles a resistor. Figure 3.16 can be interpreted as the switching of the device from a capacitor to a resistor around $+2$ V. Hence this organic semiconductor diode electrically consists of two functionalities: In reverse direction the current flow is phase shifted half a cycle behind the applied bias (the diode hence resembling a capacitor), while in forward direction the current is in phase with the voltage (resistive behavior). The simplest equivalent circuit representing this diode is hence a capacitor and a resistor in parallel.

3.2.1 Admittance studies on MDMO-PPV based diodes

Figure 3.17 shows a set of capacitances for a typical ITO - PEDOT:PSS - MDMO-PPV - Al device with an active layer thickness of approximately 130 nm. The applied bias voltages are between $+1.5$ V and $+7$ V and the frequencies for v_{ac} range from 1 kHz to 1 MHz. At voltages from $+2$ V to $+5$ V, the capacitance is rising from ≈ 1 nF at 1 MHz up to around 1.25 nF at 1 kHz, in the case of $+1.5$ V even beyond 1.3 nF. Upon increasing the bias from $+1.5$ V to $+2$ V a knee appears around 5 kHz. This feature becomes more pronounced at $+3$ V, where the capacitance plot forms a distinct minimum, shifting to higher frequencies as the voltage is increased. For $+7$ V, an additional feature becomes visible in the studied frequency window, namely an effect of decreasing capacitance towards the lower frequency edge: The capacitance reaches a maximum around 2 kHz and decreases steadily while the frequency is lowered to 1 kHz.

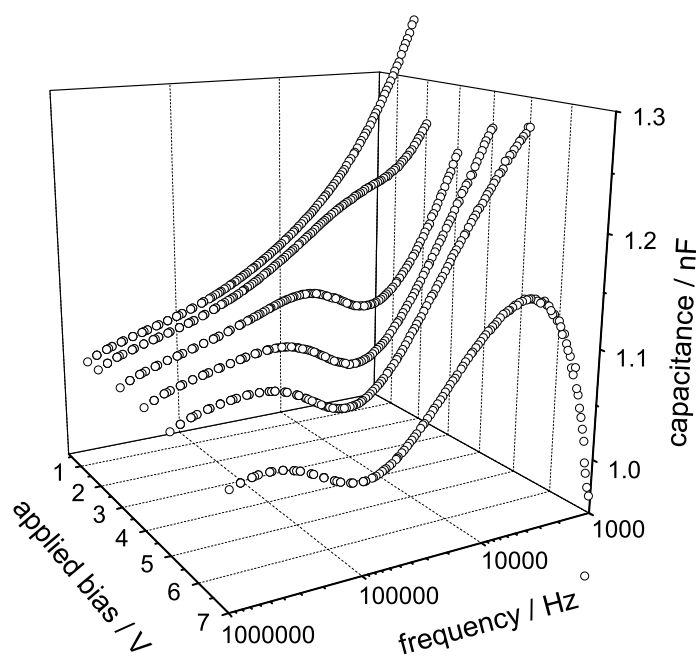Hence, three regimes are observed for typical ITO - PEDOT:PSS - MDMO-

Figure 3.17: Capacitance of a typical ITO - PEDOT:PSS - MDMO-PPV (130 nm) - Al device at various applied bias voltages as a function of frequency (200 mV ac amplitude).

PPV - Al devices presented in Fig. 3.17:

- In the studied frequency range of 1 kHz up to 1 MHz, the capacitance changes about 25%.

- For voltages of +2 V and above, a knee-like feature appears which turns into a minimum in the capacitance plot. This minimum shifts from $\approx$ 3 kHz in the case of +2 V to $\approx$ 70 kHz when +7 V are applied to the device.

- In the case of +7 V, the maximum in the capacitance is reached at 2 kHz and decreases abruptly at lower frequencies. This behavior significantly differs from that observed other lower voltages, where the capacitance reached its highest value at 1 kHz, the lowest frequency measured.

For similar device structures, but the top contact changed to Au, results are depicted in Fig. 3.18. The MDMO-PPV film thickness of 130 nm is the same as for the diode whose characteristics are plotted in Fig. 3.17. External voltages between +0.5 V and +10 V are applied to the ITO - PEDOT:PSS - MDMO-PPV - Au device. For all these voltages except the largest one, a decreasing capacitance is observed when the frequency is increased from 1 kHz to 1 MHz. In the +10 V case the maximum capacitance is reached around 2 kHz, decreasing again when the frequency is lowered down to 1 kHz. A knee appears in the graph for +0.75 V around 4 kHz. This knee becomes more pronounced and is shifted to 9 kHz when +1 V are applied. For higher bias up to +10 V the knee shapes into a pronounced minimum gradually moving from 7 kHz (+1.5 V) to roughly 500 kHz (+10 V). Hence all three phenomena observed for the MDMO-PPV based diodes with Al contact (Fig. 3.17) are found in the devices with Au top electrodes as well: Analogously to the Al case, the change in capacitance is about 25 % when the frequency is increased over three orders of magnitude from 1 kHz to 1 MHz. The knee in the plots appears already for +0.75 V in the case of Au top contacts as compared to +2 V for Al. Also the third effect of a decreasing capacitance towards low frequencies at high bias is observed. This effect appears to be less pronounced for Au electrodes as compared to Al. While in the Al case the decreasing contribution to the capacitance sets in strongly for +7 V around 2 kHz, no such feature becomes visible in the
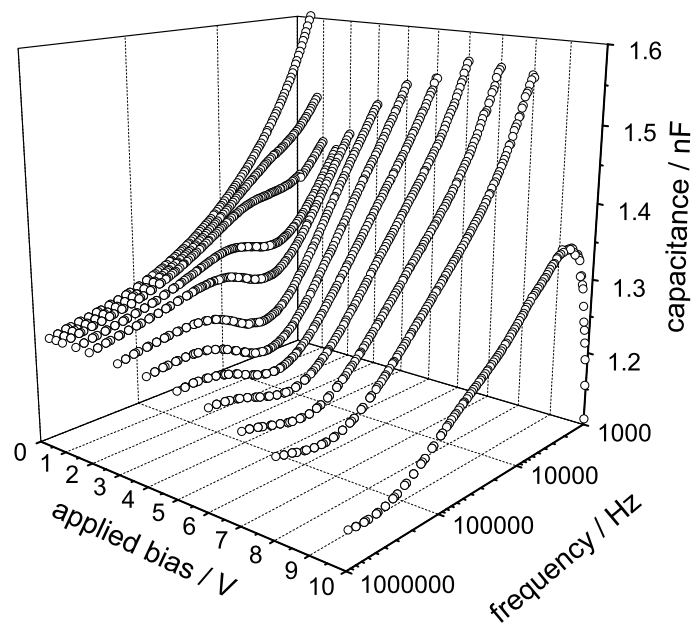
Figure 3.18: Capacitance of a typical ITO - PEDOT:PSS - MDMO-PPV
(130 nm) - Au device at various applied bias voltages as a function of fre-
quency (200 mV ac amplitude).
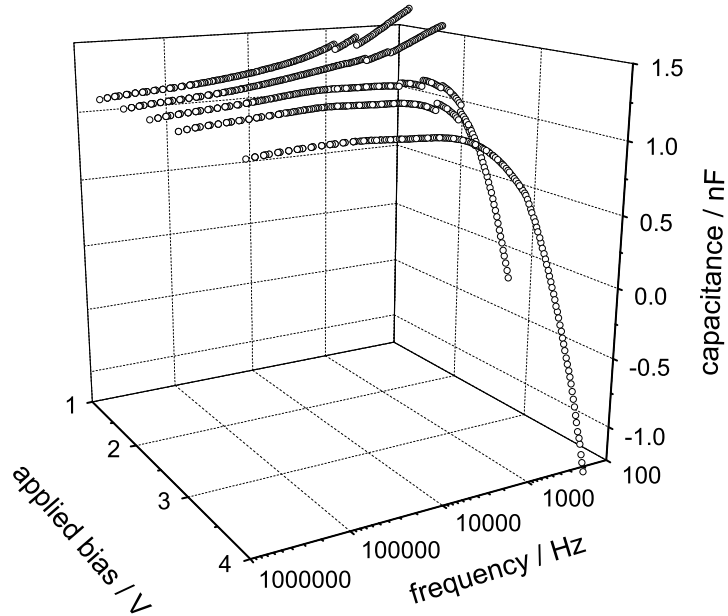
Figure 3.19: Capacitance of a typical ITO - PEDOT:PSS - MDMO-PPV (130 nm) - LiF/Al device in the frequency range 200 Hz to 1 MHz. Between +1.5 V and +4 V dc are externally applied. The ac amplitude is 200 mV.

studied frequency range for Au top contacts for this voltage. Only at +10 V a decreasing capacitance is observed in Fig. 3.18.

Figure 3.19 shows the measured device capacitance of a typical ITO - PEDOT:PSS - MDMO-PPV (130 nm) - LiF/Al structure in a voltage range between +1.5 V and +4 V for frequencies between 200 Hz and 1 MHz. The data for the frequency scans were not taken in one shot but in several stages. It can be seen in Fig. 3.19 that these stages meet at 1 kHz and 2 kHz. For the two scans with the lowest applied bias of +1.5 V and +2 V an increasing capacitance with reducing frequency is observed in the studied range. Between 1 MHz and 1 kHz this increase is of the order of 25 %, hence being comparable to the two other cases of Al and Au top contacts shown above. This effect is not visible for the curves taken at higher voltages of +2.5 V, +3 V and +4 V. The capacitance in the scan at +2.5 V remains largely

independent of the frequency down to approximately 1 kHz. The +3 V scan deviates from the almost constant high frequency capacitance roughly below 4 kHz, the +4 V scan already below 9 kHz. The distinct knees dominating the medium to high frequency regime for the MDMO-PPV devices with Al and Au contacts (Figs. 3.17 and 3.18) cannot be observed for LiF/Al top electrodes. Instead, the mechanism which is reducing the capacitance towards low frequencies is the dominating feature in all curves taken at voltages more positive than +2 V. The effect is so pronounced that the capacitance eventually turns negative around 230 Hz at +3 V and below 500 Hz when +4 V are applied to the device.

3.2.2 Excess capacitance

For all data sets depicted in Figs. 3.17, 3.18 and 3.19 the capacitance reaches an almost stable value at the high frequency side. Although still slightly decreasing, the influence of the above discussed phenomena appears to be small. The geometric capacitance (C_g) of the studied devices is given by

$$C_g = \frac{\varepsilon \varepsilon_0 A}{d} \ , \tag{3.2}$$

where ε_0 is the permittivity of free space, ε the relative permittivity of MDMO-PPV, A is the active surface area of the diode and d the thickness of the MDMO-PPV films. For the actual devices presented above these parameters are given by the device geometry (A = 5 - 6 mm^2, d = 130 nm) together with a typical ε for many conjugated polymers of 3 (e.g. [71]) and $\varepsilon_0 = 8.85 \times 10^{-12}$ Fm^{-1}. With these values, the geometric capacitance is calculated to be $\approx$ 1.0 nF - 1.2 nF. This is in excellent agreement with the high frequency capacitances measured in the devices presented above. The increase in capacitance towards lower frequencies in the order of 25% has hence to be considered as excess capacitance exceeding the geometric capacitance.

3.2.3 Single carrier drift mobility extracted from impedance measurements

Figure 3.20 shows the measured capacitance of ITO - PEDOT:PSS - MDMO-PPV (130 nm) - Au diodes. It displays the same data as Fig. 3.18 together

Figure 3.20: Capacitance of a typical ITO - PEDOT:PSS - MDMO-PPV (130 nm) - Au device at dc offsets ranging from +0.5 V to +10 V (200 mV ac amplitude). The lines represent best fits to the data.

Figure 3.21: Capacitance of a typical ITO - PEDOT:PSS - MDMO-PPV (130 nm) - Au device at dc offsets ranging from +0.5 V to +3 V (200 mV ac amplitude). The curves are off-set by 0.12 nF each to improve clarity. The lines represent best fits to the data.
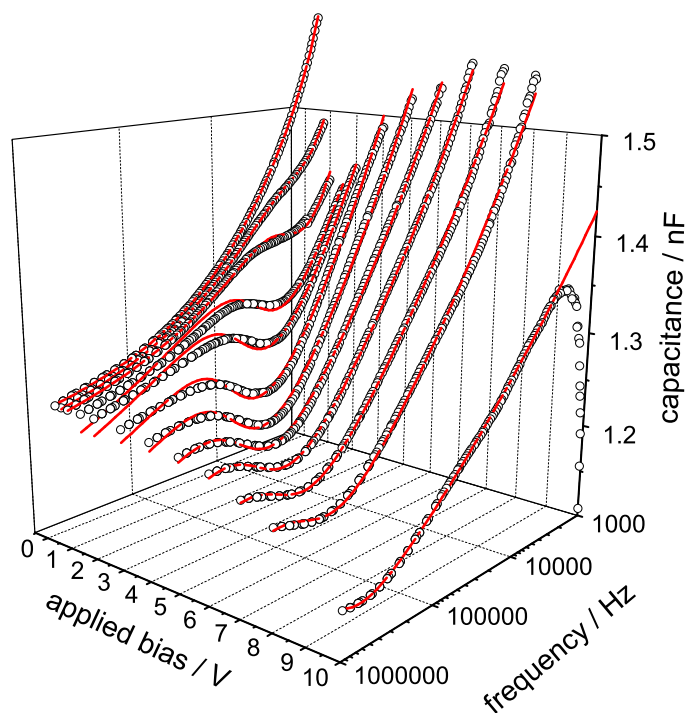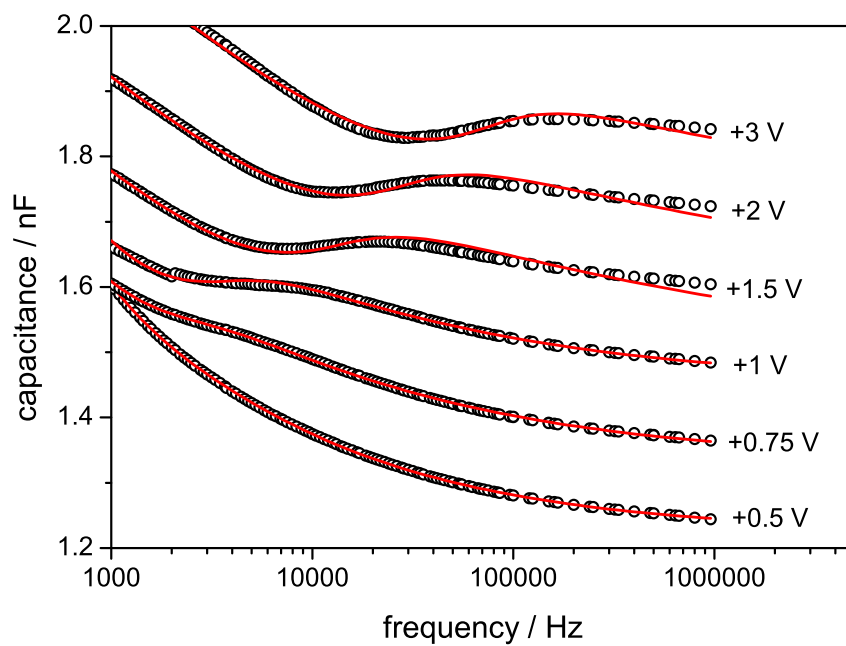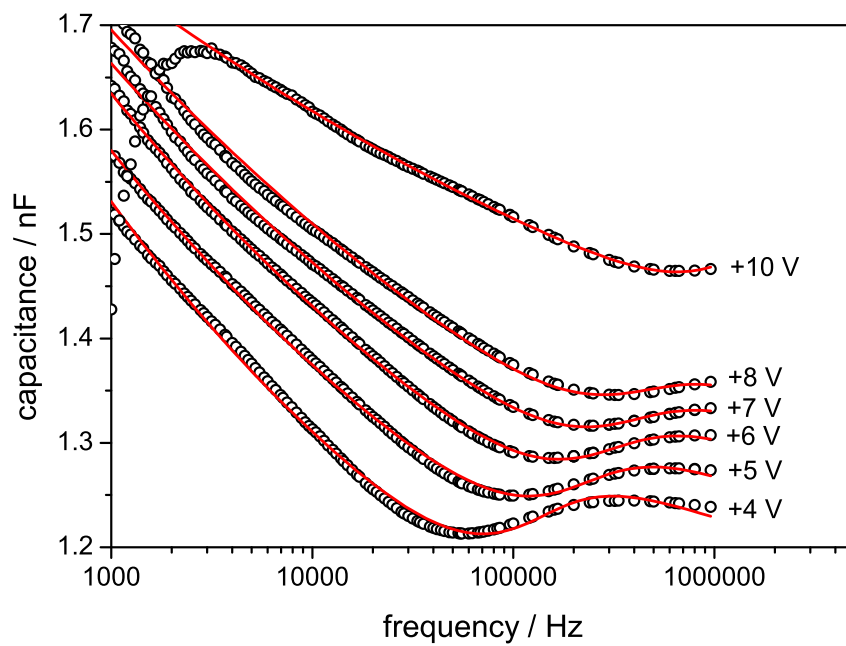
Figure 3.22: Capacitance of a typical ITO - PEDOT:PSS - MDMO-PPV (130 nm) - Au device at dc offsets ranging from +4 V to +10 V (200 mV ac amplitude). The curves are off-set by 0.04 nF each (the sweep at +10 V by 0.16 nF) to improve clarity. The lines represent best fits to the data.

Table 3.1: Capacitance analysis of ITO - PEDOT:PSS - MDMO-PPV (130 nm) - Au diodes. Fit parameters of the curves presented in Figs. 3.21 and 3.22.

applied bias	geometric capacitance C_g	transit time τ_{tr}	prop. factor M	dispersion coeff. γ
+0.5 V	1.22 ± 0.00017 nF	1260 ± 20 μs	0.48 ±0.0019	0.59 ± 0.00082
+0.75 V	1.21 ± 0.00057 nF	570 ± 7.14μs	0.26 ± 0.00087	0.66 ± 0.0015
+1 V	1.21 ± 0.0015 nF	330 ± 5.45 μs	0.20 ± 0.0013	0.67 ± 0.0036
+1.5 V	1.09 ± 0.010 nF	57.83 ± 3.10μs	0.16 ± 0.0024	0.83 ± 0.0085
+2 V	1.08 ± 0.0053 nF	29.22 ± 0.93 μs	0.15 ± 0.0016	0.83± 0.0042
+3 V	1.08 ± 0.0029 nF	11.27 ± 0.23 μs	0.14 ± 0.001	0.83 ± 0.002
+4 V	1.05 ± 0.0026 nF	5.72 ± 0.10 μs	0.15 ± 0.0011	0.85 ± 0.0013
+5 V	1.00 ± 0.0025 nF	3.25 ± 0.05 μs	0.16± 0.0011	0.87 ± 0.00076
+6 V	0.98 ± 0.0027 nF	2.28 ± 0.033 μs	0.17± 0.0013	0.88 ± 0.00059
+7 V	0.93 ± 0.0065 nF	1.66 ± 0.048 μs	0.18± 0.0033	0.89 ± 0.0001
+8 V	0.90 ± 0.012 nF	1.42 ± 0.067 μs	0.20± 0.0064	0.90 ± 0.0015
+10 V	1.00 ± 0.042 nF	0.41 ± 0.011 μs	0.13± 0.016	0.91 ± 0.0056

with the best fits according to Eq. (1.29). For better visibility of the knee-like features the curves are plotted in 2-d graphs (Figs. 3.21 and 3.22) and off-set by between 0.04 nF and 0.16 nF each. From the figures it becomes obvious that the fits are remarkably accurate. Nevertheless it has to be pointed out that the fitting procedure presented so far cannot account for the decreasing capacitance at low frequencies which is observed in the curve measured at +10 V. Hence it is assumed that a different mechanism is responsible for the negative differential capacitance. Leaving this decreasing part aside and only using the model presented above, some important parameters can be extracted from the fits. These are the geometric capacitance C_g of the device, the transit time τ_{tr}, the proportionality factor M and the dispersion coefficient γ. The last two have been introduced in Eq. (1.28). The respective numerical values determined from the fits shown in Figs. 3.22 and 3.21 are summarized in table 3.1.

The fit yields a geometric capacitance between 0.9 nF and 1.22 nF. The larger values are determined at low bias, whereas the fitting procedure yields smaller capacitances of below 1 nF at high injection bias. Taking into account the device geometry (A = 5 - 6 mm^2), thickness (d = 130 nm) and an

ε of 3, the geometric capacitance (Eq. (3.2)) is calculated to be within this range. Including errors in the determination of the thickness and the active surface area of the device as well as the inaccuracy in ε, it is not reasonable to limit the calculated geometric capacitance to a smaller range than that found from by fitting the data to Eq. (1.29).

The transit time τ_{tr} decreases several orders of magnitude from low bias to +10 V. The proportionality factor M, as defined in Eq. (1.28) is found to be in the range of 0.1 to 0.5. These two parameters are directly related to the drift of charge carriers through the film. In order to evaluate the numbers, they have to be correlated to the driving force of this drift current. The electric field across the MDMO-PPV layer causes the movement of holes from the ITO/PEDOT:PSS electrode towards the Au. Hence V_{int} has to be considered in order to estimate this driving force. For ITO - PEDOT:PSS - MDMO-PPV - Au structures, V_{int} has been determined by electroabsorption spectroscopy (Fig. 3.2) to be approximately +0.7 V. The potential drop across the MDMO-PPV is hence smaller than the externally applied bias. V_{int} is reducing the external dc voltage, which has to be corrected by V_{int} to determine the net voltage ($V_{dc} - V_{int}$). Therefore a net voltage as driving force for the charge carriers is expected only for a bias more positive than +0.7 V (compare Eq. (1.2)). The relation between transit time and net voltage (as illustrated in Fig. 3.28) reveals the strong dependence of τ_{tr} and therefore the velocity of the charges on the electric field. This is also reflected in M, which in the region above +1 V, where a net voltage drives the charges through the device is determined to be around 0.15. Below V_{int}, at +0.5 V a distinctly different value of 0.48 is determined by fitting the capacitance data.

The dispersion parameter γ increases from 0.59 to 0.91 when the voltage is increased from +0.5 V to +10 V. As the exponent in Eq. (1.28) equals $(1 - \gamma)$, the absolute value of the exponent is reduced with increasing voltage, indicative of a transport becoming less dispersive at higher bias (Fig. 3.27).

Figures 3.23 to 3.25 display data measured on a typical ITO - PEDOT:PSS - MDMO-PPV - Au diode prepared similarly to the device from Fig. 3.20 but with a thicker active layer (d $\approx$ 220 nm). Impedance measurements were performed at applied voltages between +0.6 V and +8 V.

Figure 3.23: Capacitance of a typical ITO - PEDOT:PSS - MDMO-PPV (220 nm) - Au device at dc offsets ranging from +0.8 V to +8 V (200 mV ac amplitude). The lines are best fits to the data.

Figure 3.24: Capacitance of a typical ITO - PEDOT:PSS - MDMO-PPV (220 nm) - Au device at low dc offsets ranging from +0.6 V to +1.5 V (200 mV ac amplitude). For voltages more positive than +0.8 V, a knee becomes visible in the graphs. This knee moves to higher frequencies as the voltage is increased. The lines represent best fits to the data.
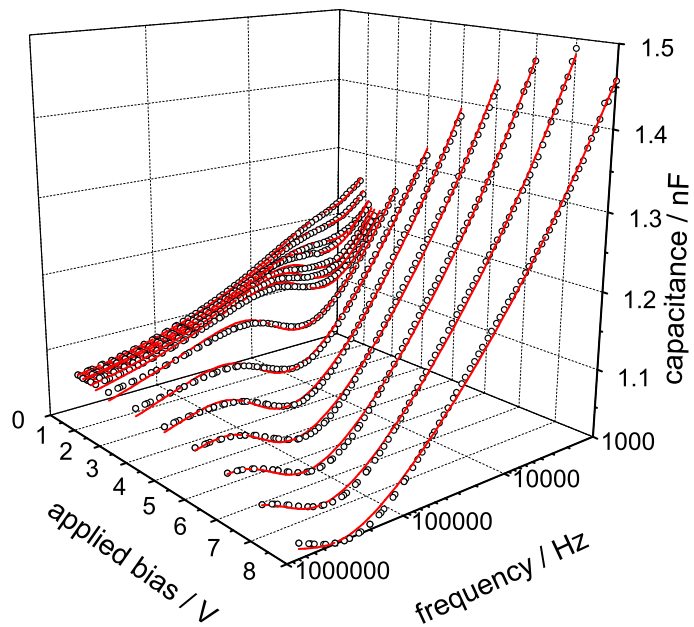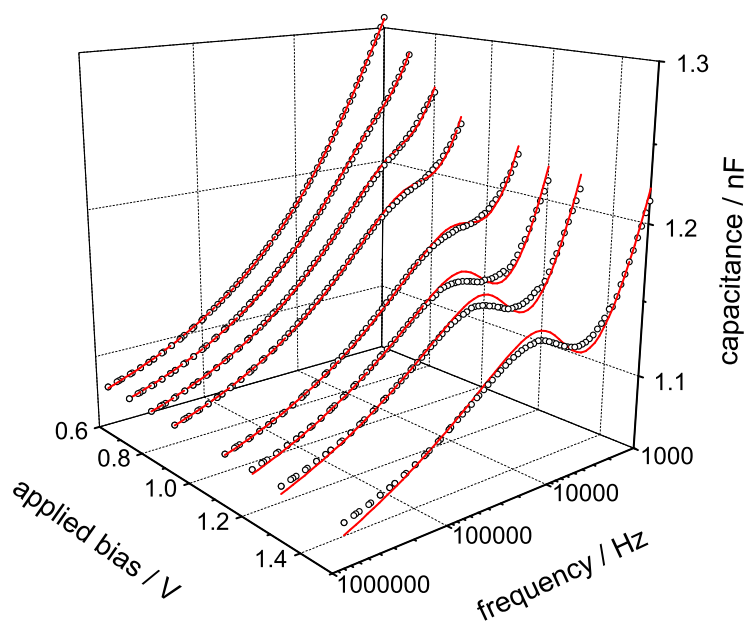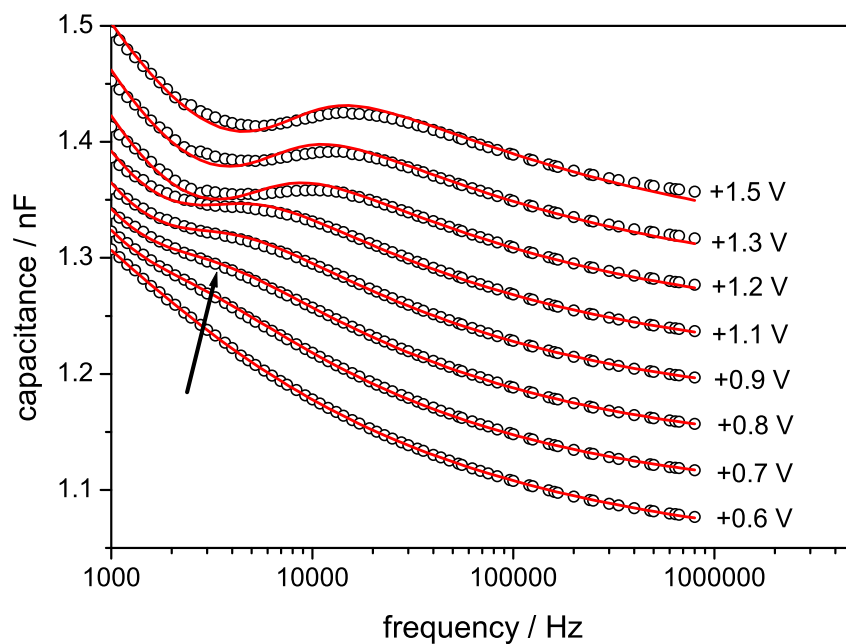
Figure 3.25: Capacitance of a typical ITO - PEDOT:PSS - MDMO-PPV (220 nm) - Au device at low dc offsets ranging from +0.6 V to +1.5 V (200 mV ac amplitude). Each sweep is off-set by 0.04 nF to the following. For voltages more positive than +0.8 V, a knee becomes visible in the graphs. This knee moves to higher frequencies as the voltage is increased. The lines represent best fits to the data.

Table 3.2: Capacitance analysis of ITO - PEDOT:PSS - MDMO-PPV (220 nm) - Au diodes. Fit parameters of the curves presented in Figs. 3.23 to 3.25.

applied bias	geometric capacitance C_g	transit time τ_{tr}	prop. factor M	dispersion coeff. γ
+0.6 V	1.04 ± 0.0006 nF	2130 ± 72 μs	0.31 ± 0.001	0.70 ± 0.002
+0.7 V	1.05 ± 0.0006 nF	760 ± 16 μs	0.27 ± 0.001	0.65 ± 0.002
+0.8 V	1.05 ± 0.0008 nF	570 ± 9.4 μs	0.24 ± 0.001	0.66 ± 0.002
+0.9 V	1.04 ± 0.001 nF	440 ± 7.4 μs	0.22 ± 0.0013	0.67 ± 0.003
+1 V	1.04 ± 0.002 nF	268 ± 6.6 μs	0.18 ± 0.0016	0.69 ± 0.006
+1.1 V	1.04 ± 0.002 nF	348 ± 6.8 μs	0.20 ± 0.0015	0.68 ± 0.0043
+1.2 V	1.04 ± 0.003 nF	211 ± 6.7 μs	0.17 ± 0.0017	0.70 ± 0.0086
+1.3 V	1.03 ± 0.0045 nF	169 ± 6.6 μs	0.16 ± 0.0015	0.72 ± 0.01
+1.5 V	1.01 ± 0.006 nF	128 ± 5.7 μs	0.15 ± 0.0008	0.75 ± 0.011
+2 V	0.98 ± 0.004 nF	41.3 ± 1.3 μs	0.14 ± 0.001	0.79 ± 0.005
+3 V	0.95 ± 0.003 nF	14.5 ± 0.38 μs	0.14 ± 0.001	0.80 ± 0.003
+4 V	0.94 ± 0.003 nF	7.0 ± 0.19 μs	0.14 ± 0.0015	0.81 ± 0.002
+5 V	0.92 ± 0.0046 nF	3.9 ± 0.14 μs	0.14 ± 0.0023	0.81 ± 0.002
+6 V	0.91 ± 0.0066 nF	2.5 ± 0.097 μs	0.14 ± 0.0034	0.82 ± 0.002
+7 V	0.89 ± 0.013 nF	1.6 ± 0.089 μs	0.15 ± 0.0067	0.83 ± 0.003
+8 V	0.83 ± 0.034 nF	1.1 ± 0.11 μs	0.17 ± 0.018	0.86 ± 0.006

Again, the features of the curves are very well reproduced when fitted to Eq. (1.29). The parameters extracted from the fitting procedure are summarized in table 3.2.

The geometric capacitance for this device is found to be in the range between 0.83 nF and 1.05 nF. For the charge carrier transit time, values ranging from the millisecond down to the microsecond regime are determined. The proportionality factor M and the dispersion parameter γ are found in the range of 0.15 - 0.31 and 0.65 - 0.86, respectively.

As the active layer thickness is increased from 130 nm to 220 nm, the geometric capacitance is expected to be reduced according to Eq. 3.2. This is reasonably well reflected in the values for C_g extracted from fitting the admittance data of both types of ITO - PEDOT:PSS - MDMO-PPV - Au diodes presented herein. The dependence of the transit times on the net voltage across the film is comparable for both devices (Fig. 3.28). The proportionality factor M is in the same range of 0.15 - 0.2 for voltages more positive than +1 V for both MDMO-PPV thicknesses. M can hence be

considered as a measure of material properties reflecting the nature of the charge carrier transport. The values of γ also coincide very well with those obtained from the thinner diode presented in Figs. 3.21 and 3.22 as well as in table 3.1.

Figure 3.25 displays the device capacitance at low injection bias between +0.6 V and +1.5 V. Considering a V_{int} of +0.7 V, the net voltage ($V_{dc} - V_{int}$) ranges from -0.1 V to +0.8 V. In the case of +0.6 V applied (-0.1 V net), the electric field is opposite to the favorable direction of the movement of holes in the device from ITO/PEDOT:PSS to Au. Besides the decrease in capacitance from 1 kHz to 1 MHz by more than 0.2 nF, no additional features that could be related to the interelectrode transit time of charges can be observed. When V_{int} is compensated by an external dc bias of +0.7 V, a curve very similar to the +0.6 V case is obtained. However, a shoulder appears in the decay in capacitance, when the bias is further increase to +0.8 V. With increasing bias, the shoulder shifts to higher frequencies forming a separate peak for voltages exceeding +1.2 V. In the case of the thinner MDMO-PPV based device with Au contact shown in Fig. 3.21, the shoulder was observed when the voltage was increased from +0.5 V to +0.75 V, hence also only when V_{int} is overcompensated. Therefore the appearance of the transit time induced features in the device capacitance is attributed to V_{int}, independent of the active layer thickness.

In Fig. 3.26 a set of measured capacitances for ITO - PEDOT:PSS - MDMO-PPV (130 nm) - Al diodes at various injection levels is displayed. The data together with their best fits to Eq. (1.29) are off-set by 0.1 nF each in order to improve clarity. For an applied bias in the range of +1 V to +5 V, the data obtained between 1 kHz and 1 MHz are fitted to Eq. (1.29). For higher voltages a decrease in the capacitance at low frequencies is observed in the measured range (Fig. 3.17). These features cannot be fitted accurately to Eq. (1.29), hence the respective frequency range between 1 kHz and 13 kHz is omitted for the fitting displayed in Fig. 3.26. The data measured at +1 V and +1.5 V show a decrease in capacitance from 1 kHz to 1 MHz by about 0.3 nF. At the next voltage level of +2 V a shoulder appears, which for +3 V and above forms a distinct peak moving to higher frequencies. Table 3.3 summarizes the fit parameters. The geometric capacitance is determined to be between 0.78 nF and 1.05 nF and is hence in
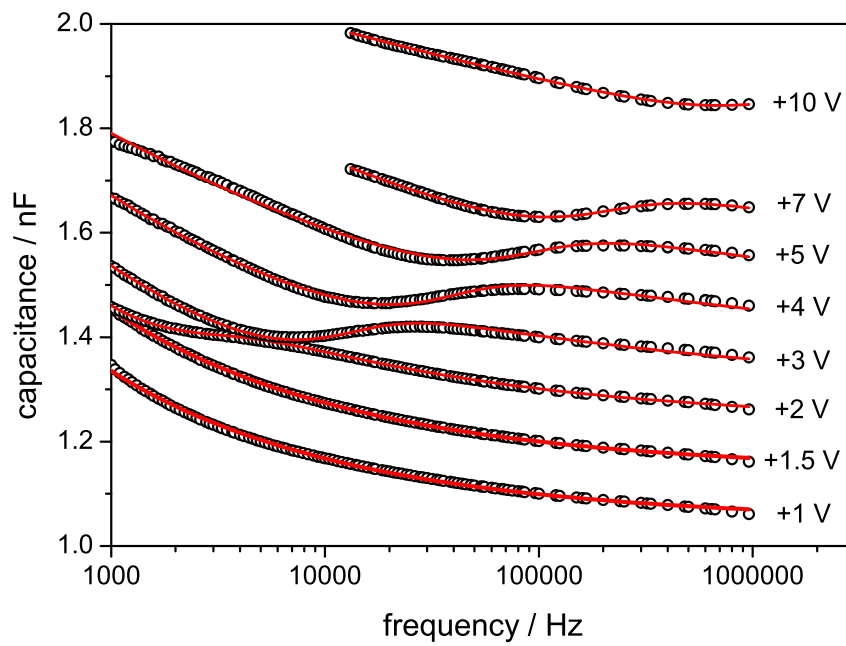
Figure 3.26: Capacitance of a typical ITO - PEDOT:PSS - MDMO-PPV (130 nm) - Al device at dc offsets ranging from +1 V to +10 V (200 mV ac amplitude). The curves are offset by 0.1 nF each to improve clarity. The lines represent best fits to the data assuming space charge limited current with traps.

Table 3.3: Capacitance analysis of ITO - PEDOT:PSS - MDMO-PPV (130 nm) - Al diodes. Fit parameters of the curves presented in Figs. 3.26.

applied bias	geometric capacitance C_g	transit time τ_{tr}	prop. factor M	dispersion coeff. γ
+1 V	1.05 ± 0.0022 nF	28 ± 130 ms	0.98 ± 1.56	0.64 ± 0.013
+1.5 V	1.04 ± 0.0013 nF	10 ± 9 ms	0.72 ± 0.21	0.64 ± 0.0068
+2 V	1.04 ± 0.0005 nF	400 ± 4.2 μs	0.23 ± 0.0008	0.66± 0.0015
+3 V	1.00 ± 0.0028 nF	73.2 ± 1.7 μs	0.14 ± 0.0005	0.75 ± 0.005
+4 V	0.96 ± 0.0021 nF	22.5 ± 0.4 μs	0.14 ± 0.0007	0.80 ± 0.0025
+5 V	0.91 ± 0.0027 nF	8.55 ± 0.19 μs	0.15 ± 0.0012	0.84 ± 0.0019
+7 V	0.87 ± 0.0013 nF	3.7 ± 0.032 μs	0.15± 0.0005	0.85 ± 0.0012
+10 V	0.78 ± 0.055 nF	0.43 ± 0.019 μs	0.22± 0.032	0.93 ± 0.0045

the range expected from the device parameters. As in the two other cases introduced above, a decrease of C_g with bias is observed.

The dependence of τ_{tr} on the acting net voltage is displayed in Fig. 3.28 and found to be similar to the studied devices with Au contacts. Electroabsorption spectroscopy yielded a V_{int} of +1.6 V for ITO - PEDOT:PSS - MDMO-PPV - Al devices. Just as has been observed in Fig. 3.25, the features related to the transit time of charge carriers are only visible at voltages exceeding V_{int}. The values determined for the dispersion coefficient γ are summarized in Fig. 3.27. For all three compared device configurations in the measured voltage range, γ is determined to be between 0.65 and 0.93. When γ is plotted versus the net voltage (V - V_{int}) a similar behavior is observed in all cases. Between V_{int} and an acting net voltage of about +1.5 V, γ rises steeply from 0.65 to approximately 0.8. For further increasing voltages up to +9 V, only a comparably small increase to about 0.9 is observed. The observed behavior indicates the transition from a dispersive to a significantly less dispersive transport in MDMO-PPV around a net voltage of +1.5 V. Figure 3.28 compares the interelectrode transit times extracted from fits at various diode configurations and dc voltages. The dependence on the net voltage acting in the device is very similar for all studied types of devices. The transit time decreases over several orders of magnitude when the dc bias is increased from the compensation voltage of V_{int} up to +10 V. At applied voltages, which are exceeding V_{int} only slightly a τ_{tr} of close to 1 ms is determined, which is reducing to the sub-microsecond regime at net
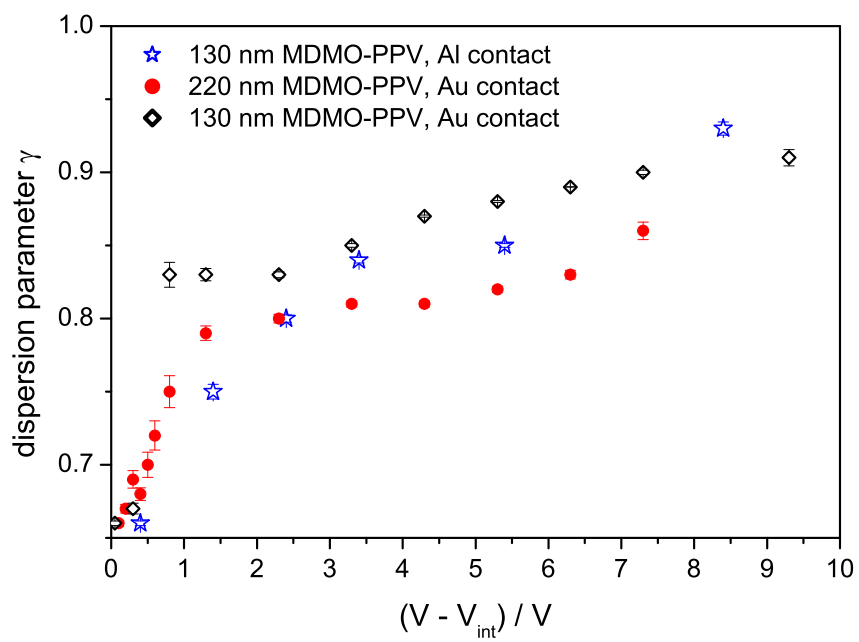
Figure 3.27: Dispersion parameter γ of ITO - PEDOT:PSS - MDMO-PPV - Au devices of 130 nm (diamonds) and 220 nm (circles) active layer thickness as well as ITO - PEDOT:PSS - MDMO-PPV (130 nm) - Al diodes (stars) as a function of the voltage acting in the device.
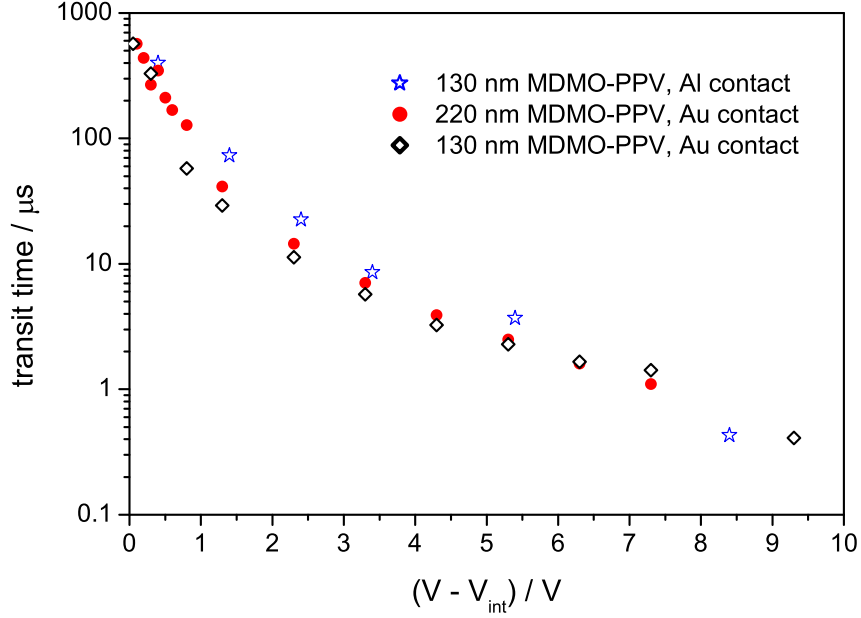
Figure 3.28: Transit time τ_{tr} of ITO - PEDOT:PSS - MDMO-PPV - Au devices of 130 nm (diamonds) and 220 nm (circles) active layer thickness as well as ITO - PEDOT:PSS - MDMO-PPV (130 nm) - Al diodes (stars) as a function of the voltage acting in the device.

voltages around +9 V. It has been shown above that space charge limited current prevails in devices based on pristine MDMO-PPV. From Eq. (1.18)

$$\tau_{tr} = \frac{4L^2}{3\mu_{dc}(V - V_{int})} \; .$$

the drift mobility of single carrier devices can be derived from the transit time under SCLC conditions. Figure 3.29 displays these calculated hole mobilities plotted versus the average electric field inside the device. To determine the electric field, the applied voltage is corrected by V_{int} and divided by the active layer thickness. A strong electric field dependence of the mobility becomes evident from Fig. 3.29. Straight lines are included as guide to the eyes, visualizing a linear relation between $\log(\mu)$ and (electric field)$^{0.5}$. These lines allow to extrapolate the mobilities to zero electric field (μ_0). The assumption of space charge limited current with traps underlies

71
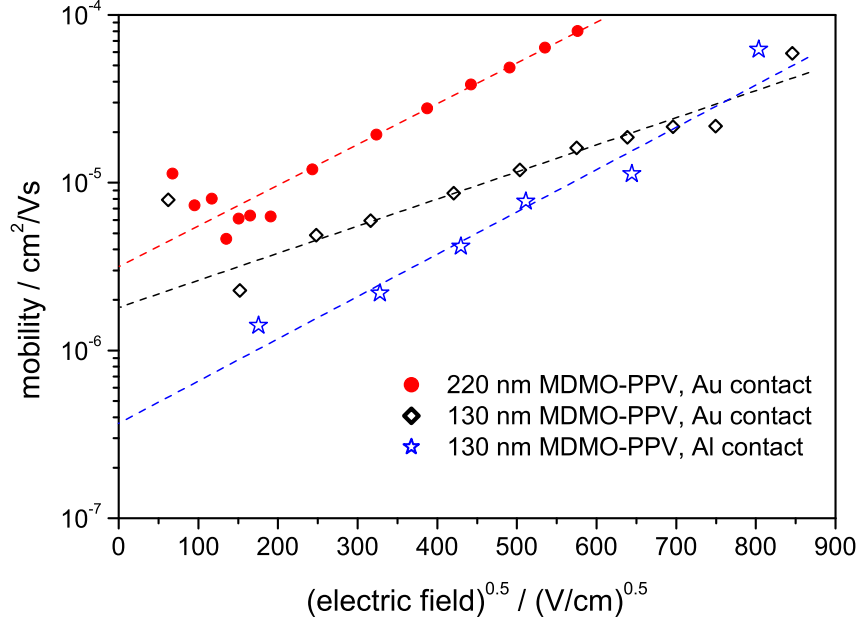
Figure 3.29: Hole mobility of ITO - PEDOT:PSS - MDMO-PPV - Au devices of 130 nm (diamonds) and 220 nm (circles) active layer thickness as well as ITO - PEDOT:PSS - MDMO-PPV (130 nm) - Al diodes (stars) as a function of the electric field acting in the device. The dashed lines are guides to the eye.

the fitting of the admittance data to Eq. (1.29). Together with the large barrier for electron injection in the studied devices which was substantiated by Electroabsorption spectroscopy, predominant hole current is expected in the studied devices. Hence, the fits to the admittance data allow to extract hole mobilities in MDMO-PPV. For the studied ITO - PEDOT:PSS - MDMO-PPV (130 nm) - Al diodes a zero field mobility for holes of approximately 4×10^{-7} cm^2/Vs is estimated from the fits to the measured capacitance data. For ITO - PEDOT:PSS - MDMO-PPV (130 nm) - Au devices $\mu_0 = 2 \times 10^{-6}$ cm^2/Vs and for 220 nm thick devices of the same structure $\mu_0 = 3 \times 10^{-6}$ cm^2/Vs is obtained from impedance spectroscopy with the underlying model summarized in Eq. (1.29). The mobilities extracted from the experimental data and displayed in Fig. 3.29 follow the electric field dependence outlined in Eq. (3.3). They are hence in good

agreement with the findings reported in the literature. Also the numerical values of the zero field hole mobilities estimated from Fig. 3.29, which are determined to be in the order of 10^{-6} cm^2/Vs are in line with previously published values [46, 41, 30]. PPV derivatives are well studied compounds in the field of polymer semiconductors. Reflecting this importance, charge carrier mobilities in PPVs and especially MDMO-PPV have been derived in a whole variety of different ways (e.g. [41, 46, 30]). The electric field dependence of the mobility of various PPV derivatives was found to be well described by the stretched ("Poole-Frenkel type" [72]) exponential law [73]

$$\mu(E) = \mu_0 \ exp(\gamma_F \sqrt{E}) \ . \qquad (3.3)$$

Here, μ_0 is the zero-field mobility, while γ_F describes the "field activation" of the mobility. The mobility relation described in Eq. (3.3) has been found in a whole variety of different materials ([74] and references herein), starting with poly(N-vinyl carbazole) already 30 years ago [75, 31]. Also more recent time-of-flight (ToF) experiments yield the same dependence [76]. Bässler developed a model based on Monte Carlo simulation [11]. Though much more elaborate than Eq. (3.3) it yields the same proportionality between the mobility and E ($\mu \propto exp\sqrt{E}$). This peculiar relation stems from the fact that barriers for charge transport in the field direction by the applied electrostatic potential [77].

3.3 Negative capacitance

3.3.1 Negative capacitance in MDMO-PPV based diodes

By fitting the experimental admittance data to Eq. (1.29) good results can be achieved as shown in the previous section. For moderate injection into MDMO-PPV based diodes with electrodes yielding an appreciable barrier for electron injection (Au, Al), the agreement is excellent. However, with increasing forward bias a phenomenon becomes visible which is not accounted for in the fit (e.g. Fig. 3.20): In the low frequency range a mechanism which diminishes the measured capacitance is observed. This effect is becoming increasingly pronounced when the top electrode is changed from Au to Al (Fig. 3.26). For LiF/Al electrodes it is already dominating the admittance data (Fig. 3.19), even causing the capacitance to change sign at low frequen-

cies. In order to study the peculiar phenomenon of a negative capacitance (NC) in more detail, the low frequency capacitance response is plotted as a function of voltage. Figure 3.30 shows electroluminescence (EL), Electroabsorption and capacitance data typically obtained from ITO - PEDOT:PSS - MDMO-PPV - LiF/Al devices. EL and capacitance are measured at room temperature. The capacitance data is determined at 20 Hz. The EA response is probed at 590 nm and obtained at low temperatures of around 100 K in order to avoid disturbing current flow in the active layer.

From Fig. 3.30, V_{int} is determined to be +1.8 V by EA spectroscopy. The onset of light emission from the device is extrapolated to start at approximately +1.9 V. Following the capacitance versus voltage plot from reverse bias on, an increase in the capacitance is noted, peaking around +1.8 V. From that voltage on the capacitance decreases, eventually turning negative around +3.6 V.

Figure 3.31 depicts the results of EL, EA and capacitance measurements (at 73 Hz) for ITO - PEDOT:PSS - MDMO-PPV - Al devices with a comparably thin active layer of about 70 nm. The onset of EL is extrapolated to about +2.1 V, V_{int} is determined to be +1.6 V and the capacitance at 73 Hz peaks at +2.2 V.

Using LiF/Al or Al top electrodes, in both cases there is a close correlation between the maximum measured capacitance, hence the voltage at which a reducing effect sets in and the onset of light emission. In the case of LiF/Al top electrodes, the onset of the EL also corresponds to the voltage necessary to cancel the EA response, being equivalent to V_{int}. This is interpreted as almost ohmic contact for electrons and holes between MDMO-PPV and the respective electrodes [18]. In the case of Al electrodes light emission only occurs at voltages larger than V_{int}. This is attributed to the barrier for electron injection as compared to LiF/Al electrodes that has to be overcome. The maximum capacitance for the device is measured at approximately the same voltage as the the onset of EL. Therefore the effect of NC can be correlated to bipolar injection into the conjugated polymer based diode as has already been suggested in the literature [78].

In Fig. 3.32 the capacitance for an ITO - PEDOT:PSS - MDMO-PPV - LiF/Al diode with an active layer thickness of ≈ 80 nm is shown. The device capacitance is plotted for voltages between +1.5 V and +2 V and frequencies between 30 Hz and 100 Hz. In the case of +1.5 V the capacitance
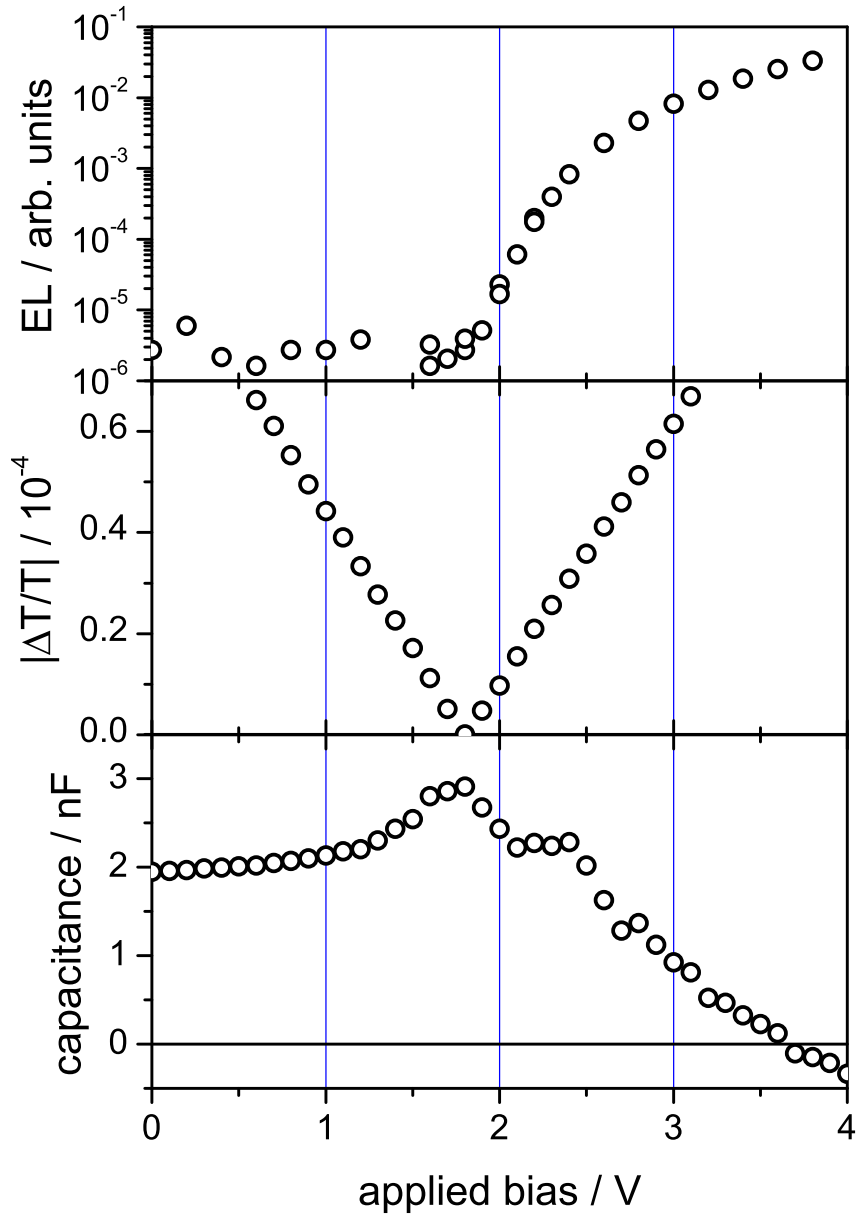
Figure 3.30: Electroluminescence (EL, uppermost graph), first harmonic Electroabsorption (middle) and capacitance (lower graph) of a typical ITO - PEDOT:PSS - MDMO-PPV - LiF/Al device. Electroluminescence and capacitance (20 Hz, 200 mV ac amplitude) are determined at room temperature, the Electroabsorption response (590 nm, 1 V ac amplitude) at $\approx$ 100 K.
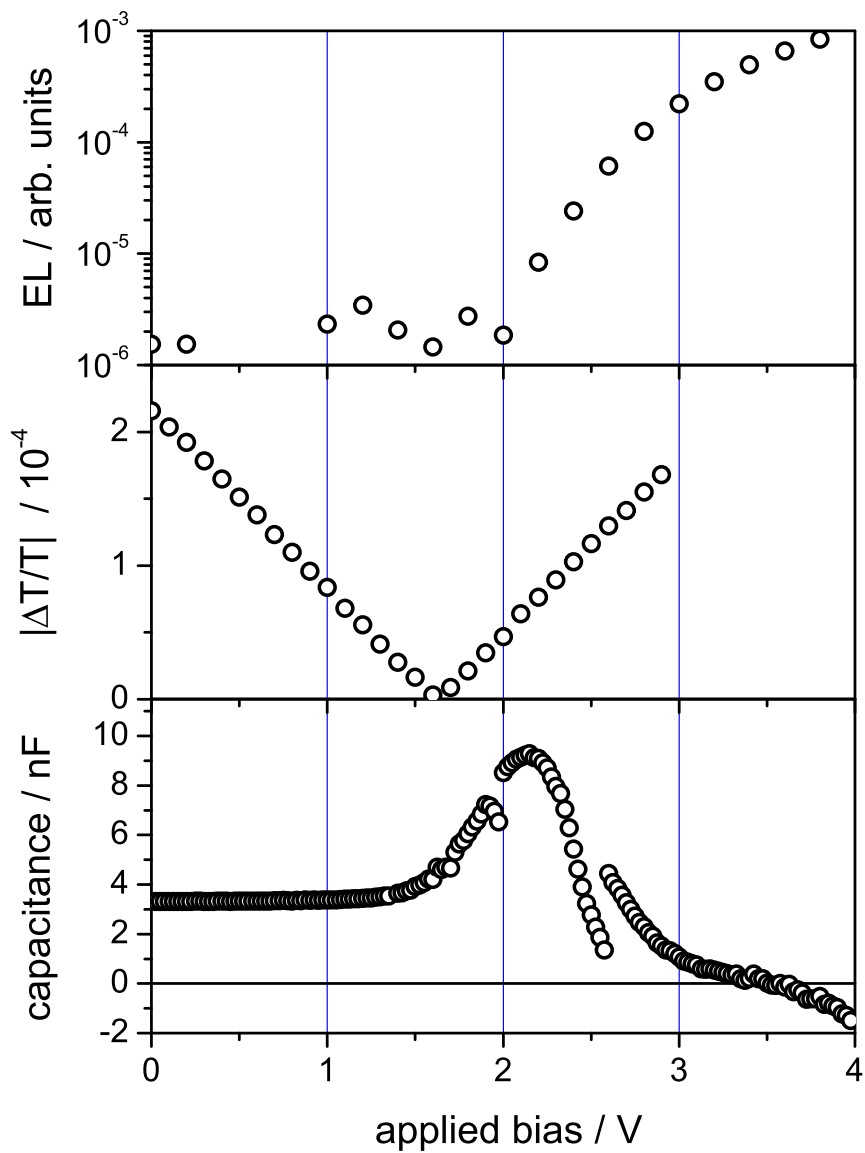
Figure 3.31: Electroluminescence (uppermost graph), Electroabsorption (middle) and capacitance (lower graph) of a typical ITO - PEDOT:PSS - MDMO-PPV - Al device. Electroluminescence and capacitance (73 Hz, 200 mV ac amplitude) are determined at room temperature, the Electroabsorption (590 nm, 1 V ac amplitude) response at $\approx$ 100 K.

Figure 3.32: Capacitance of ITO - PEDOT:PSS - MDMO-PPV ($\approx$ 80 nm) - LiF/Al devices at frequencies ranging from 30 Hz to 100 Hz. Applied bias between +1.5 V and +2 V.
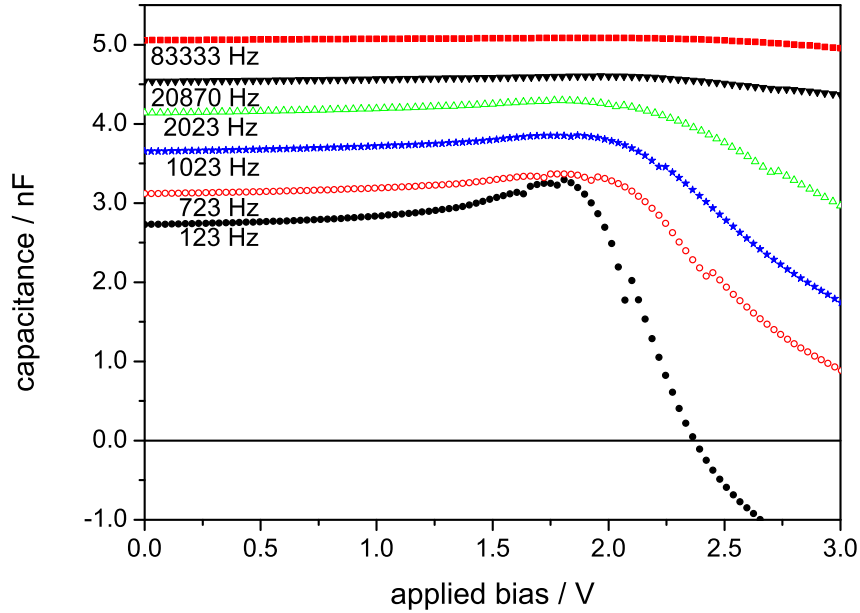
Figure 3.33: Capacitance as a function of the applied bias for ITO - PE-DOT:PSS - MDMO-PPV ($\approx$ 80 nm) - LiF/Al devices at various frequencies. The curves are off-set by 0.6 nF each in order to improve clarity.

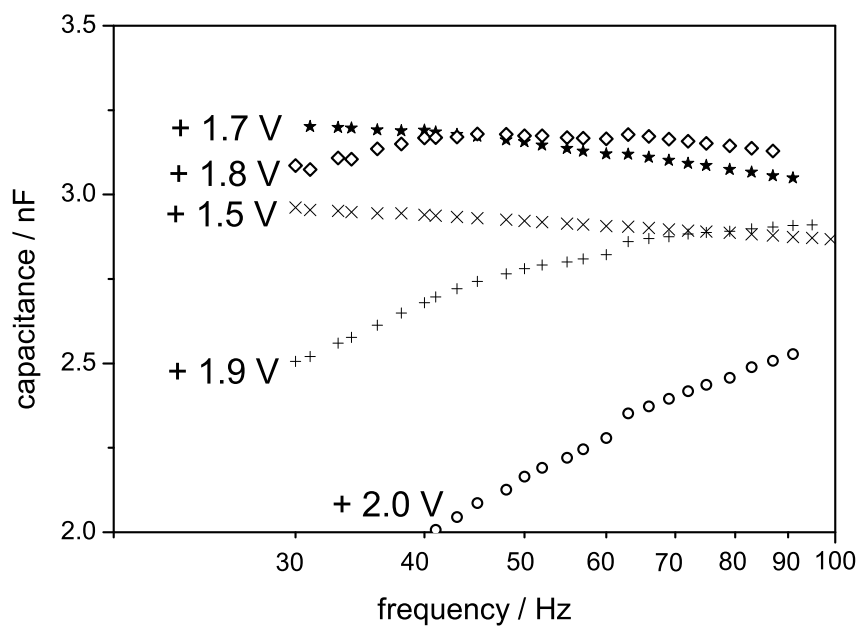monotonously decreases from 30 Hz to 100 Hz. For +1.7 V the capacitance seems to level off and to form a plateau below 40 Hz at roughly +3.2 nF. Increasing the applied dc bias to +1.8 V yields a broad peak around 50 Hz, hence a negative contribution becomes visible at frequencies lower than 50 Hz. By increasing the voltage to +1.9 V and +2 V, the diminishing contribution already dominates the observed frequency range. This observation confirms the experimental data shown in Fig. 3.30. If +1.8 V are applied to ITO - PEDOT:PSS - MDMO-PPV - LiF/Al devices the capacitance is reduced at low frequencies.

Figure 3.33 displays the measured capacitance of an ITO - PEDOT:PSS - MDMO-PPV - LiF/Al diode as a function of voltage for several frequencies. The active layer thickness is $\approx$ 80 nm and therefore the same as for the device in Fig. 3.32. The curves are off-set by 0.6 nF each. At low frequencies the features of the capacitance increase at voltages smaller than +1.8 V and its decrease at higher bias are very pronounced. The capacitance sweep at
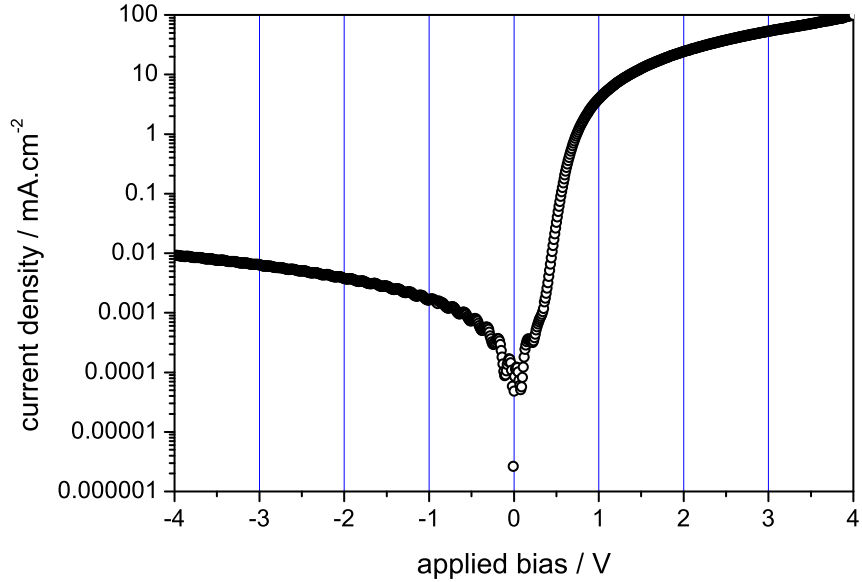
Figure 3.34: Typical current density - voltage characteristic of ITO - PE-DOT:PSS - C_{60} - LiF/Al devices. Active layer thickness $\approx$ 300 nm.

123 Hz is shown to turn negative for voltages more positive than $+2.3$ V. At higher frequencies the capacitance shows broader and less pronounced peaks around $+1.8$ V, but no negative values are observed in the studied voltage range of up to $+3$ V. At 80 kHz the capacitance sweep appears to be almost featureless. The phenomenon of NC is highly frequency dependent, being more pronounced and dominant the lower the frequency.

3.3.2 Negative capacitance in fullerene based diodes

Figure 3.34 displays the J-V characteristics of a typical ITO - PEDOT:PSS - C_{60} - LiF/Al device with an active layer thickness of approximately 300 nm. At $+/-$ 4 V, a rectification ratio of four orders of magnitude is observed. The capacitance features of this device are plotted in Fig. 3.35. For an applied voltage of $+0.5$ V, the capacitance is positive over the studied frequency range between 20 Hz and 1 kHz. Already at $+0.75$ V NC is observed between 20 Hz and 30 Hz. With increasing bias, the magnitude of NC as well as the frequency range over which it is observed grows. At $+4$ V and
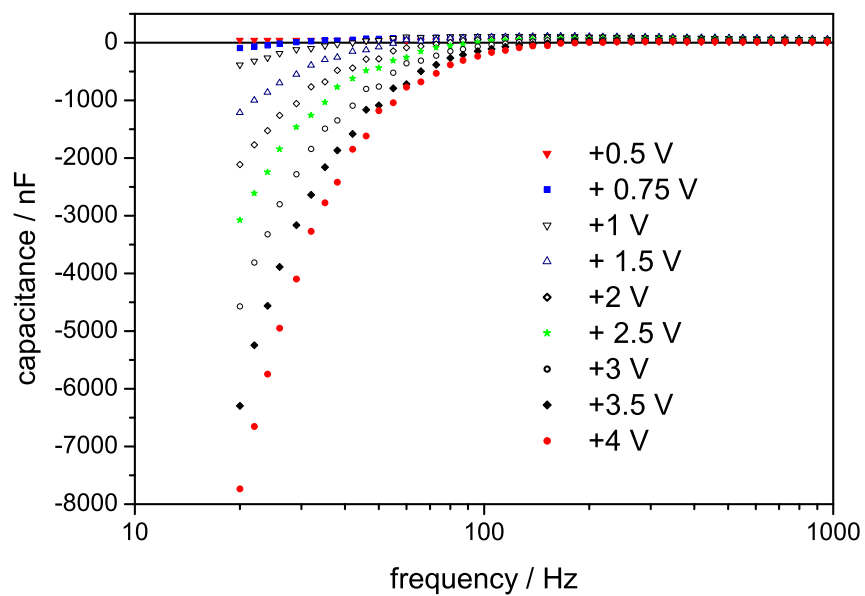
Figure 3.35: Capacitance measurements on ITO - PEDOT:PSS - C_{60} - LiF/Al devices at dc voltages ranging from +0.5 V to +4 V. ac amplitude 50 mV. Active layer thickness $\approx$ 300 nm.
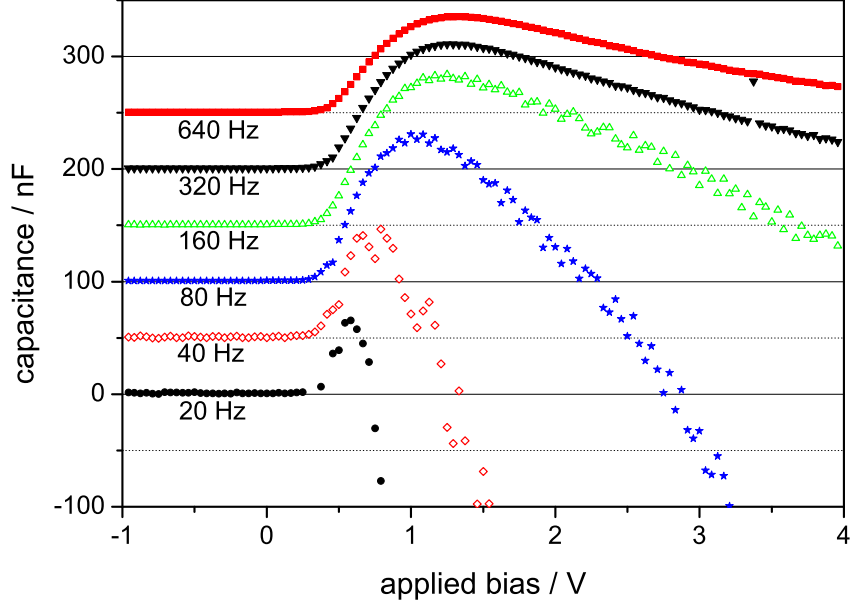
Figure 3.36: Capacitance measurements on ITO - PEDOT:PSS - C_{60} - LiF/Al devices at various frequencies between 20 Hz and 640 Hz. The curves are off-set by 50 nF each to improve clarity. ac amplitude 50 mV. Active layer thickness $\approx$ 300 nm.

20 Hz almost -8 μF are measured. The +4 V curve only turns positive at 200 Hz. In Fig. 3.36 the capacitance of the same device is displayed as a function of voltage at frequencies ranging from 20 Hz to 640 Hz. The curves are off-set by 50 nF each. The maxima of the sweeps shift from +0.6 V at 20 Hz to 1.3 V at 640 Hz.

The correlation between the turn-on of Electroluminescence and the appearance of NC cannot be done as demonstrated above in the case of MDMO-PPV. The lowest energy transition across the bandgap is not allowed. Luminescence from C_{60}-based devices is only observed at low temperatures (e.g. [79, 80]). However, at 100 K, no negative capacitance was observed.

3.3.3 Fits to negative capacitance

Traps for charge carriers in the MDMO-PPV film were found to be responsible for an increase in the measured capacitance, which is exceeding the

geometric capacitance [43, 48]. In the case of moderate bias for Au and Al electrodes the experimental data could be fitted to Eq. (1.29). Eq. (1.29) was derived for current consisting of one kind of charge carriers, electrons or holes.

It was shown experimentally, that bipolar injection leads to an effect opposite to that of traps. As depicted in Figs. 3.30 and 3.31, injection of electrons and holes causes a reduction of the measured capacitance as compared to the single injection case. In order to account for this effect Eitan Ehrenfreund developed an Ansatz of how to treat this reductive component. He suggested to introduce an additional term into Eq. (1.29). The subtractive contribution to the capacitance is

$$\Delta C_r(\omega) = -\frac{\Delta G_r \tau_r}{1 + (\omega^2 \tau_r^2)^\delta} \ , \tag{3.4}$$

where ΔG_r is the recombination induced variation of the conductance G, τ_r is the average electron-hole recombination time and $0 < \delta < 1$ is the dispersive exponent. This term is derived from the influence of electron-hole recombination on the capacitance due to delayed current flow [81]. In Figs. 3.37, 3.38 and 3.39 the capacitance of ITO - PEDOT:PSS - MDMO-PPV - LiF/Al devices is presented as a function of frequency for a wide range of applied bias between +1.5 V and +10 V. They also include the best fits to Eq. (1.29), taking into account Eq. (3.4). With the contribution of Eq. (3.4), the agreement between fit and data is good in a frequency range of several orders of magnitude.

As illustrated in Fig. 3.26 the capacitance of ITO - PEDOT:PSS - MDMO-PPV (130 nm) - Al diodes at +7 V and +10 V could not be fitted meaningfully to Eq. (1.29) over the measured frequency range between 1 kHz and 1 MHz. However, by introducing Eq. (3.4) as additional term to Eq. (1.29), the fit reproduces the experimental data in great detail (Fig. 3.40). As shown in Fig. 3.41, the capacitance obtained over the whole measured frequency and voltage range can be fitted exceptionally well.
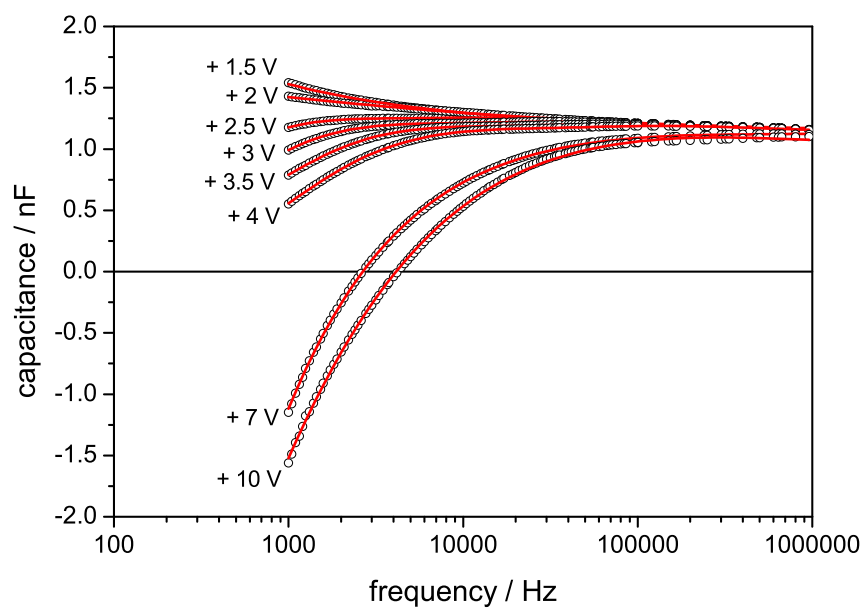
Figure 3.37: Capacitance measurements on ITO - PEDOT:PSS - MDMO-PPV - LiF/Al devices at applied bias voltages between +1.5 V and +10 V in the frequency range between 1 kHz up to 1 MHz. The solid lines represent best fits to the data ac amplitude 200 mV. Active layer thickness ≈ 130 nm.
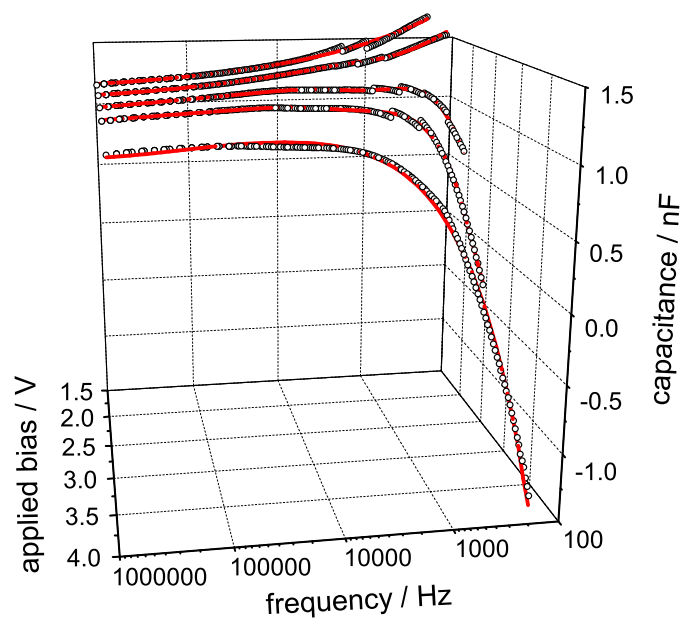
Figure 3.38: Capacitance measurements on ITO - PEDOT:PSS - MDMO-PPV - LiF/Al devices at applied bias voltages between +1.5 V and +4 V in the frequency range between 200 Hz up to 1 MHz. The solid lines represent best fits to the data ac amplitude 200 mV. Active layer thickness $\approx$ 130 nm.
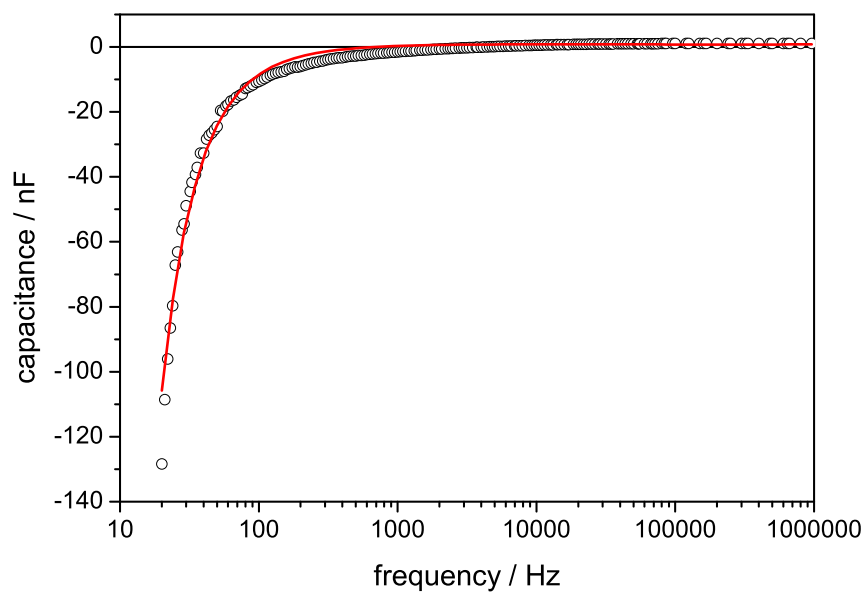
Figure 3.39: Capacitance measurements on ITO - PEDOT:PSS - MDMO-PPV - LiF/Al devices at +10 V from 20 Hz up to 1 MHz. The solid line represents the best fit to the data. ac amplitude 200 mV. Active layer thickness ≈ 130 nm.

Figure 3.40: Capacitance measurements on ITO - PEDOT:PSS - MDMO-PPV - Al devices at +7 V and +10 V in the frequency range between 1 kHz up to 1 MHz. The solid lines represent best fits to the data ac amplitude 200 mV. Active layer thickness ≈ 130 nm.

Figure 3.41: Capacitance measurements on ITO - PEDOT:PSS - MDMO-PPV - Al between +1.5 V and +7 V in the frequency range between 1 kHz up to 1 MHz. The solid lines represent best fits to the data ac amplitude 200 mV. Active layer thickness $\approx$ 130 nm.
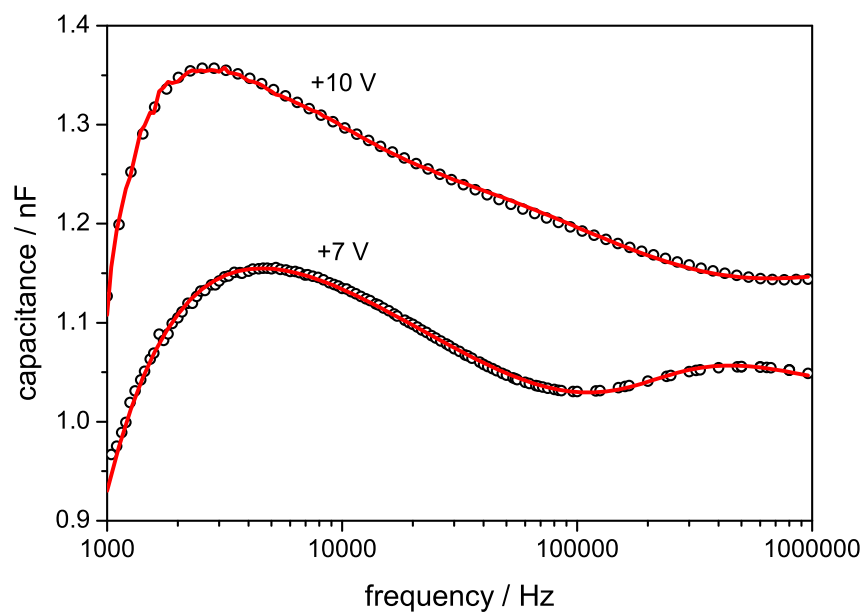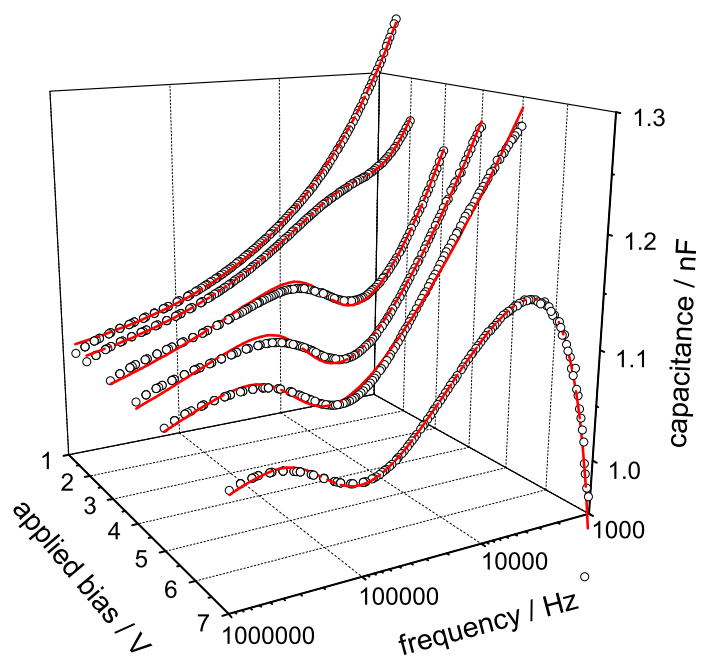
3.4 Negative capacitance induced by charge carrier recombination

Assuming that there exist "recombination centers", in the form of localized states. When both charges are trapped in the center, with a probability which is governed by a time constant τ_r, they recombine, thereby contributing to the current. If τ_r is infinitely long, then there is no contribution to the current, since electrons and holes do not recombine. If $\tau_r = 0$, then the contribution to the current is maximized, since all injected (minority) carriers recombine. For a finite τ_r, the probability of trap filling and hence the contribution to the current should be proportional to

$$\Delta j_r(t) \propto (1 - e^{-t/\tau_r}) \ . \tag{3.5}$$

The variation in conductance due to this recombination process (ΔG_r) depends on the occupancy of the traps, which is a function of carrier concentration, density of recombination centers and the energy levels of the recombination centers.

If a short voltage step, ΔV, superimposed on a dc bias is applied at time $t = 0$, the change due to the recombination current is given by:

$$\Delta j_r(t) = \Delta V \Delta G_r [1 - e^{-t/\tau_r}] \ . \tag{3.6}$$

The response of the system to this short voltage step allows to determine its contribution to the capacitance by employing the method of "Fourier decomposition of transient excitation" used in the small signal analysis of semiconductor devices [81]. Following Eq. (5b) in Ref. [81] the change in capacitance due to the recombination current is determined as:

$$\Delta C_r(\omega) = \frac{1}{\Delta V} \int_0^\infty \Delta j_r(t) \cos(\omega t) \ dt \ . \tag{3.7}$$

Substituting $\Delta j_r(t)$ from Eq. (3.6), the integral in Eq. (3.7) can be solved and

$$\Delta C_r(\omega) = -\frac{\Delta G_r \tau_r}{1 + \omega^2 \tau_r^2} \tag{3.8}$$

is obtained. Thus, the recombination process gives rise to a NEGATIVE contribution to the capacitance.

Eq. (3.8) describes the situation for a single recombination time τ_r. For a distribution of τ_r typical for dispersive dynamics Eq. (3.9) changes to [82]

$$\Delta C_r(\omega) = -\frac{\Delta G_r \tau_r}{1 + (\omega^2 \tau_r^2)^\delta} \ ,$$ (3.9)

where $0 < \delta < 1$ is the dispersive exponent and τ_r corresponds to an average recombination time.

In order to be able to use the fitting procedure in the computer program ORIGIN, ΔC_r is subtracted from Eq. (1.29) as

$$\Delta C_r = rr \ C_g \frac{1 + \Omega_{tr}^{1-br} cos\left(\pi \frac{1-br}{2}\right)}{1 + \Omega_{tr}^{2(1-br)} + 2\Omega_{tr}^{(1-br)} cos\left(\pi \frac{1-br}{2}\right)} \ ,$$ (3.10)

where $\Omega_{tr} = 2\pi f \tau_r$, br is the dispersion coefficient of the recombination process and rr introduced as a recombination ratio, describing the strength of the negative contribution to the capacitance as a proportionality constant to the geometric capacitance C_g.

Chapter 4

Conclusion

The internal electric field in organic semiconductor thin film devices based on π-conjugated polymers is determined and the implications of V_{int} on the device performance is studied. V_{int} is identified as the maximum photovoltage theoretically deliverable by the respective device. It is determined to be the driving force of the photocurrent and depends on the metal top contact in the case of pristine polymer devices. However, V_{int} was shown to be changed by adding only 1 % (w/w) of an electron acceptor species (PCBM). In this case evidence was found that V_{int} is determined by the energy offset between the HOMO of MDMO-PPV and the LUMO of PCBM.

With a sufficiently small amount of mobile charge carriers, which was shown to be the case for MDMO-PPV in the dark, the electric field is homogeneous in absence of significant charge carrier injection. However, in doped conjugated polymers, such as P3HT exposed to air, the amount of free charge carriers in the film is sufficient to screen the electric field already close to the electrode. In this case, Schottky-like behavior of the semiconductor/metal contact was demonstrated.

From the determination of V_{int}, a substantial barrier for electron injection from Al and Au contacts into MDMO-PPV is apparent. Dominant hole current at sufficiently small voltages is hence concluded. Underlying a model based on single carrier space charge limited current with traps, the measured admittance could be fitted satisfactorily for moderate bias.

At higher voltages or by using LiF/Al electrodes, a negative contribution to the device capacitance was found experimentally and could be correlated to bipolar injection. At sufficiently large bias and low frequencies this feature is

dominant and can result in a measured negative device capacitance. In order to account for this contribution, an additional term has to be introduced to the established fit formalism in order to achieve reasonable agreement with the experimental data. This negative contribution is derived assuming a slow recombination process between electrons and holes.

Bibliography

[1] W. Helfich and W. G. Schneider. *Phys. Rev. Lett.*, 14:226, 1965.

[2] G. H. Heilmeier and S. E. Harrison. *Phys. Rev.*, 132, 1963.

[3] C. W. Tang and S. A. VanSlyke. *Appl. Phys. Lett.*, 51:913, 1987.

[4] H. Shirakawa, E. J. Louis, A. G. MacDiarmid, C. K. Chiang, and A. J. Heeger. *J. Chem. Soc. Chem. Comm.*, 16:578, 1977.

[5] C. K. Chiang, C. R. Fincher Jr, Y. W. Park, A. J. Heeger, E. J. Louis H. Shirakawa, S. C. Gau, and A. G. MacDiarmid. *Phys. Rev. Lett.*, 39(17):1098, 1977.

[6] C. K. Chiang, M. A. Druy, S. C. Gau, A. J. Heeger, E. J. Louis, A. G. MacDiarmid, Y. W. Park, and H. Shirakawa. *J. Am. Chem. Soc.*, 100:1013, 1978.

[7] M. C. Scharber, D. Mühlbacher, M. Koppe, P. Denk, C. Waldauf, A. J. Heeger, and C. J. Brabec. *Adv. Funct. Mat.*, 18:789, 2006.

[8] W. Brütting, S. Berleb, and A. G. Mückl. *Org. Electron.*, 2:1, 2001.

[9] S. M. Sze. *Physics of semiconductor devices.* John Wiley & Sons, New York, 1981.

[10] *Primary photoexcitations in conjugated polymers: Molecular exciton versus semiconductor band model.* Edited by N.S. Sariciftci, World Scientific, Singapore, 1997.

[11] H. Bässler. *Phys. Status Solidi (b)*, 175:15, 1993.

[12] P. Würfel. *Physics of Solar Cells.* John Wiley & Sons, New York, 1997.

[13] C. Lungenschmied, G. Dennler, H. Neugebauer, N. S. Sariciftci, M. Glatthaar, T. Meyer, and A. Meyer. *Sol. Energy Mater. Sol. Cells*, 91:379, 2007.

[14] L. J. A. Koster, V. D. Mihailetchi, and P. W. M. Blom. *Appl. Phys. Lett.*, 88:093511, 2006.

[15] S. E. Shaheen, R. Radspinner, N. Peyghambarian, and G. E. Jabbour. *Appl. Phys. Lett.*, 79:2996, 2001.

[16] M. A. Lampert and P. Mark. *Current injection in solids*. Academic Press, New York, 1970.

[17] G. Dennler, N. S. Sariciftci, R. Schwödiauer, S. Bauer, and H. Reiss. *Appl. Phys. Lett.*, 86:193507, 2005.

[18] C. Lungenschmied, G. Dennler, E. Ehrenfreund, H. Neugebauer, and N. S. Sariciftci. *Appl. Phys. Lett.*, 89:223519, 2006.

[19] B. A. Mattis, P. C. Chang, and V. Subramanian. *Mat. Res. Soc. Symp. Proc.*, 771, 2003.

[20] M. S. A. Abdou, F.P. Orfino, Y. Son, and S. Holdcroft. *J. Am. Chem. Soc.*, 119:4518, 1997.

[21] S. Hoshino, M. Yoshida, S. Uemura, T. Kodzasa, N. Takada, T. Kamata, and K. Yase. *J. Appl. Phys.*, 95:5088, 2004.

[22] N. S. Sariciftci, L. Smilowitz, A. J. Heeger, and F. Wudl. *Science*, 258:1474, 1992.

[23] S. E. Shaheen, C. J. Brabec, F. Padinger, T. Fromherz, J. C. Hummelen, and N. S. Sariciftci. *Appl. Phys. Lett.*, 78:841, 2001.

[24] I. H. Campbell, T. W. Hagler, D. L. Smith, and J. P. Ferraris. *Phys. Rev. Lett.*, 76:1900, 1996.

[25] L. S. Hung, C. W. Tang, and M. G. Mason. *Appl. Phys. Lett.*, 70:152, 1997.

[26] T. M. Brown, R. H. Friend, I. S. Millard, D. L. Lacey, J. H. Burroughes, and F. Cacialli. *Appl. Phys. Lett.*, 77(19):3096, 2000.

[27] T. M. Brown, R. H. Friend, I. S. Millard, D. L. Lacey, T. Butler, J. H. Burroughes, and F. Cacialli. *J. Appl. Phys.*, 93(10):6159, 2003.

[28] C. Lungenschmied, G. Dennler, E. Ehrenfreund, H. Neugebauer, and N. S. Sariciftci. *Proc. SPIE*, 6192:322, 2006.

[29] I. D. Parker. *J. Appl. Phys.*, 75(3):1656, 1994.

[30] H. C. F. Martens, P. W. M. Blom, and H. F. M. Schoo. *Phys. Rev. B*, 61:7489, 2000.

[31] W. D. Gill. *J. Appl. Phys.*, 43:5033, 1972.

[32] G. Yu, C. Zhang, and A. J. Heeger. *Appl. Phys. Lett.*, 64:1540, 1994.

[33] C. J. Brabec, S. Shaheen, C. Winder, P. Denk, and N. S. Sariciftci. *Appl. Phys. Lett.*, 80:1288, 2002.

[34] C. J. Brabec, A. Cravino, D. Meissner, N. S. Sariciftci, T. Fromherz, M.T. Rispens, L. Sanchez, and J.C. Hummelen. *Adv. Funct. Mater.*, 11:374, 2001.

[35] A. Gadias, M. Svensson, M. Andersson, and O. Inganäs. *Appl. Phys. Lett.*, 84:1609, 2004.

[36] J. Liu, Y. Shi, and Y. Yang. *Adv. Funct. Mater.*, 11:420, 2001.

[37] L. J. A. Koster, V. D. Mihailetchi, and P. W. M. Blom. *Appl. Phys. Lett.*, 88:093511, 2006.

[38] G. J. Matt, N. S. Sariciftci, and T. Fromherz. *Appl. Phys. Lett.*, 84:1570, 2004.

[39] J. H. Burroughes, D. D. C. Bradley, A. R. Brown, R. N. Marks, K. Mackey, R. H. Friend, P. L. Burn, and A. B. Holmes. *Nature*, 347:539, 1990.

[40] P. Stadler. *Diploma Thesis, Johannes Kepler University, Linz*, 2006.

[41] P. W. M. Blom, M. J. M. de Jong, and J. J. M. Vleggaar. *Appl. Phys. Lett.*, 68:3308, 1996.

[42] I. Shao and G. T. Wright. *Solid State Electronics*, 3:291, 1961.

[43] R. Kassing. *Phys. Status Solidi (a)*, 28:107, 1975.

[44] R. Kassing and E. Kähler. *Solid State Commun.*, 15:673, 1974.

[45] P. W. M. Blom and M. C. J. M. Vissenberg. *Phys. Rev. Lett.*, 80:3819, 1998.

[46] G. Dennler, A. J. Mozer, G. Juška, A. Pivrikas, R. Österbacka, A. Fuchsbauer, and N. S. Sariciftci. *Org. Electron.*, 7:229, 2006.

[47] A. J. Mozer, N. S. Sariciftci, L. Lutsen, D. Vanderzande, R. Österbacka, M. Westerling, and Juška. *Appl. Phys. Lett.*, 86:112104, 2005.

[48] H. C. F. Martens, H. B. Brom, and P. W. M. Blom. *Phys. Rev. B*, 60:R8489, 1999.

[49] J. Bisquert, G. Garcia-Belmonte, A. Pitarch, and H. Bolink. *Chem. Phys. Lett.*, 422:184, 2006.

[50] S. Berleb and W. Brütting. *Phys. Rev. Lett.*, 89:286601, 2001.

[51] H. H. P. Gommans, V. Kemerink, and R. A. J. Janssen. *Phys. Rev. B*, 72:235204, 2005.

[52] A. Pitarch, G. Garcia-Belmonte, J. Bisquert, and H. Bolink. *J. Appl. Phys.*, 100:084502, 2006.

[53] A. Pitarch, G. Garcia-Belmonte, and J. Bisquert. *Proc. SPIE*, 5519:307, 2004.

[54] H. C. F. Martens, J. N. Huiberts, and P. W. M. Blom. *Appl. Phys. Lett.*, 77:1852, 2000.

[55] H. H. P. Gommans, V. Kemerink, and W. H. A. Schilders. *Phys. Rev. B*, 72:165110, 2005.

[56] G. Weiser and A. Horvath. *Primary photoexcitations in conjugated polymers: Molecular exciton versus semiconductor band model*, chapter 12, Electroabsorption spectroscopy on π-conjugated polymers. Edited by N.S. Sariciftci, World Scientific, Singapore, 1997.

[57] D. Mühlbacher, H. Neugebauer, A. Cravino, and N. S. Sariciftci. *Synth. Met.*, 137:1361, 2003.

[58] V. D. Mihailetchi, P. W. D. Blom, J. C. Hummelen, and M. T. Rispens. *J. Appl. Phys.*, 94:6849, 2003.

[59] A. Rajagopal, C. I. Wu, and A . Kahn. *J. Appl. Phys*, 83:2649, 1998.

[60] H. Ishii, K. Sugiyama, E. Ito, and K. Seki. *Adv. Mat.*, 11:605, 1999.

[61] G. Dennler, C. Lungenschmied, N. S. Sariciftci, R. Schwödiauer, S. Bauer, and H. Reiss. *Appl. Phys. Lett.*, 87:163501, 2005.

[62] A. Assadi, C. Svensson, M. Willander, and O. Inganäs. *J. Appl. Phys.*, 72:2900, 1992.

[63] M. Meier, S. Karg, and W. Riess. *J. Appl. Phys.*, 82:1961, 1997.

[64] K. Henisch. *Rectifying Semiconductor Contacts*. Clarendon, Oxford, 1957.

[65] S. Karg, M. Meier, and W. Riess. *J. Appl. Phys.*, 82:1951, 1997.

[66] H. Tomozawa, D. Braun, S. D. Phillips, R. Worland, A. J. Heeger, and H. Kroemer. *Synth. Metals*, 28:687, 1989.

[67] Z. Chiguvare, J. Parisi, and V. Dyakonov. *J. Appl. Phys.*, 94:2440, 2003.

[68] H. Killesreiter and H. Baessler. *Chem. Phys. Lett.*, 11:411, 1971.

[69] C. M. Heller, I. H. Campbell, D. L. Smith, N. N. Barashkov, and J. P. Ferraris. *J. Appl. Phys.*, 81(7):3227 – 3231, 1997.

[70] C. Winder, D. Mühlbacher, H. Neugebauer, N. S. Sariciftci, C. J. Brabec, R. A. J. Janssen, and J. C. Hummelen. *Mol. Cryst. Liq. Cryst. Sci. Technol., Sect. A*, 93:385, 2002.

[71] G. Juška, K. Genevišius, R. Österbacka, K. Arlauskas, T. Kreouzis, D. D. C. Bradley, and H. Stubb. *Phys. Rev. B*, 67:081201, 2003.

[72] J. Frenkel. *Phys. Rev.*, 54:647, 1938.

[73] P. W. M. Blom, M. J. M. de Jong, and M. G. van Munster. *Phys. Rev. B*, 55:R656, 1997.

[74] A. J. Mozer and N. S. Sariciftci. *Handbook of conducting polymers*, chapter 10, Conjugated polymer based photovoltaic devices. John Wiley & Sons, New York, 2006.

[75] D. M. Pai. *J. Chem. Phys.*, 52:2285, 1970.

[76] L. B. Schein, A. Peled, and D. Glatz. *J. Appl. Phys.*, 66:686, 1989.

[77] S. V. Novikov, D. H. Dunlap, V. M. Kenkre, P. E. Parris, and A. V. Vannikov. *Phys. Rev. Lett.*, 81:4472, 1998.

[78] V. Shrotiya and Y. Yang. *J. Appl. Phys.*, 97:054504, 2005.

[79] M. S. Dresselhaus, G. Dresselhaus, and P. C. Eklund. *Science of fullerenes and carbon nanotubes*, chapter 12, Electronic Structure. Academic Press, New York, 1996.

[80] A. T. Werner, H. J. Byrne, and S. Roth. *Synth. Met.*, 70:1409, 1995.

[81] S. E. Laux. *IEEE Transactions on Computer-Aided Design*, 4:472, 1985.

[82] O. Epshtein, G. Nakhmanovich, Y. Eichen, and E. Ehrenfreund. *Phys. Rev. B*, 63:125206, 2001.

CURRICULUM VITAE

DI Christoph Lungenschmied
Tegetthoffstraße 42
4020 Linz, Austria
Telephone: 0043-650-7312831
E-mail: christoph.lungenschmied@jku.at

Personal Data

Date/Place of birth:	April 8, 1979 in Linz, Austria
Nationality:	Austrian
Marital Status:	Unmarried

Education

Since 09/2004	Ph.D. student at the Linz Institute for Organic Solar Cells (LIOS) "Injection and recombination phenomena in organic semiconductor thin film devices"
09/2004 - 01/2006	Co-worker EU project "European polymer solar battery" Prototype development of flexible and sealed plastic solar cell modules
04/2003 - 06/2004	Diploma student at the Linz Institute for Organic Solar Cells (LIOS) "Electroabsorption in organic diodes"
07/2002 - 09/2002	Internship at DAINIPPON Ink and Chemicals, Inc. Tokio, Japan
10/1998 - 07/2004	Johannes Kepler University Linz, Austria Economics/Chemical Engineering
06/1997	School leaving exam passed with distinction

Military Service

10/1997 - 5/1998	Telecommunication unit in Linz/Hörsching

Language Skills

Language:	Englisch (fluent), Spanish and French (beginner)

Personal Interests

Sports (fistball), travelling, reading

PUBLICATIONS

Negative capacitance in organic semiconductor devices:
bipolar injection and charge recombination mechanism

E. Ehrenfreund, C. Lungenschmied, G. Dennler, H. Neugebauer, N. S. Sariciftci
accepted by *Applied Physics Letters*

Flexible, long-lived, large-area, organic solar cells

C. Lungenschmied, G. Dennler, H. Neugebauer, N. S. Sariciftci, M. Glatthaar,
T. Meyer, A. Meyer
Solar Energy Materials and Solar Cells **91** (2007) 379

Internal electric field in organic semiconductor based photovoltaic devices

C. Lungenschmied, G. Dennler, E. Ehrenfreund, H. Neugebauer, N. S. Sariciftci
Applied Physics Letters **89** (2006) 223519

The effect of intermediate layers on the internal electric field in
organic semiconductor devices

C. Lungenschmied, G. Dennler, E. Ehrenfreund, H. Neugebauer, N. S. Sariciftci
Proceedings of SPIE, Organic Optoelectronics and Photonics II **6192** (2006) 330

Flexible encapsulation for organic solar cells

C. Lungenschmied, G. Dennler, G. Czeremuszkin, M. Latreche, H. Neugebauer, N. S. Sariciftci
Proceedings of SPIE, Photonics for Solar Energy Systems **6197** (2006) 258

A self-rechargeable and flexible polymer solar battery

G. Dennler, S. Bereznev , D. Fichou, K. Holl, D. Ilic, R. Koeppe, M. Krebs,
A. Labouret, C. Lungenschmied, A. Marchenko, D. Meissner, E. Mellikov,
J. Meot, A. Meyer, T. Meyer, H. Neugebauer, A. Öpik, N. S. Sariciftci,
S. Taillemite, T. Wöhrle
Solar Energy in print

A new encapsulation solution for flexible organic solar cells

G. Dennler, C. Lungenschmied, H. Neugebauer, N. S. Sariciftci, M. Latreche,
G. Czeremuszkin, M. R. Wertheimer
Thin Solid Films **511 - 512** (2006) 349

Flexible, conjugated polymer based solar cells: Basics, encapsulation and integration

G. Dennler, C. Lungenschmied, H. Neugebauer, N. S. Sariciftci, A. Labouret
Journal of Material Research **20** (2005) 3224

Unusual electromechanical effects in organic semiconductor Schottky contacts:
between piezoelectricity and electrostriction

G. Dennler, C. Lungenschmied, N. S. Sariciftci, R. Schwödiauer, S. Bauer, H. Reiss
Applied Physics Letters **87** (2005) 163501

Electric field induced enhancement of the photoinduced absorption in
conjugated polymer/fullerene bulk heterojunction solar cells

C. Winder, C. Lungenschmied, N. S. Sariciftci, C. Arndt, U. Zhokhavets, and G. Gobsch
submitted to *Organic Electronics*

Smart actuators based on electromechanically active conjugated polymer diodes

G. Dennler, R. Schwödiauer, C. Lungenschmied, S. Bauer, N. S. Sariciftci, H. Reiss
Proceedings of SPIE, Electroactive Polymer Actuators and Devices **5759** (2005) 532

Investigation of excited states in polymer/fullerene solar cells
by means of photoinduced reflection-/absorption spectroscopy

C. Arndt, U. Zhokhavets, G. Gobsch, C. Winder, C. Lungenschmied, N. S. Sariciftci
Thin Solid Films **451 - 452** (2004), 60

Excited state spectroscopy in polymer fullerene photovoltaic devices
under operation conditions

C. Winder, C. Lungenschmied, G. Matt, N. S. Sariciftci, A. F. Nogeira, I. Montanari,
J. R. Durrant, C. Arndt, U. Zhokhavets, G. Gobsch
Synthetic Metals **139** (2003) 577

CONFERENCES

Invited talks

Flexible, large area, encapsulated organic solar cells

C. Lungenschmied, G. Dennler, H. Neugebauer, N. S. Sariciftci, M. Glatthaar,
T. Meyer, A. Meyer
50th Annual Meeting of the Society of Vacuum Coaters (SVC) 2007,
April 30 - May 3, 2007, Louisville (Kentucky)

Oral presentations

Flexible, long lived, large area organic solar cells

C. Lungenschmied, G. Dennler, H. Neugebauer, N. S. Sariciftci, G. Czeremuszkin,
M. Latreche
International Conference on Synthetic Metals (ICSM) 2006,
July 2 - 6, 2006, Dublin (Ireland)

Comparative studies of the internal electric field probed by
electroabsorption spectroscopy in organic semiconductor devices

C. Lungenschmied, C. Winder, M. C. Scharber, A. J. Mozer, G. J. Matt,
H. Neugebauer, N. S. Sariciftci
207th Meeting of the Electrochemical Society (ECS),
May 15 - 20, 2005 Quebec (Canada)

Comparative studies of the internal electric field probed by
electroabsorption spectroscopy in bulk heterojunction solar cells

C. Lungenschmied, C. Winder, M. C. Scharber, A. J. Mozer, H. Neugebauer,
N. S. Sariciftci
16th Workshop on Quantum Solar Energy Conversion (QUANTSOL 2005),
March 13 - 19, 2005, Rauris (Austria)

Comparative electroabsorption studies on organic semiconductor devices
with various interfacial layers

C. Lungenschmied, M. C. Scharber, H. Neugebauer, N. S. Sariciftci
69th Annual Meeting of the German Physical Society (DPG),
March 4 - 9, 2005, Berlin (Germany)

Electroabsorption studies on organic diodes

C. Lungenschmied, C. Winder, M. C. Scharber, A. J. Mozer, G. J. Matt,
H. Neugebauer, N. S. Sariciftci
5th International Conference on Electronic Processes in Organic Materials (ICEPOM-5),
May 24 - 29, 2004, Kiev (Ukraine)

Poster presentations

Internal electric field studies on conjugated polymer and polymer:fullerene based diodes

C. Lungenschmied, G. Dennler, E. Ehrenfreund, H. Neugebauer, N. S. Sariciftci
International Conference on Synthetic Metals (ICSM) 2006,
July 2 - 7, 2006, Dublin (Ireland)

Electroabsorption studies on working organic semiconductor devices with
various intermediate layers

C. Lungenschmied, G. Dennler, E. Ehrenfreund, H. Neugebauer, N. S. Sariciftci
SPIE Photonics Europe,
April 3 - 7, 2006, Strasbourg (France)

Flexible encapsulation for organic solar cells

G. Dennler, C. Lungenschmied, G. Czeremuszkin, M. Latreche, H. Neugebauer,
N. S. Sariciftci
SPIE Photonics Europe,
April 3 - 7, 2006, Strasbourg (France)

Electroabsorption studies on organic diodes

C. Lungenschmied, C. Winder, M. C. Scharber, A. J. Mozer, G. J. Matt,
G. Dennler, H. Neugebauer, N. S. Sariciftci
Euroconference Photovoltaic Devices (EURO-PV 2004),
October 15 - 20, 2004, Kranjska Gora (Slovenia)

Eidesstattliche Erklärung:

Ich erkläre an Eides statt, dass ich die vorliegende Dissertation selbständig verfasst und keine anderen als die angegebenen Quellen und Hilfsmittel benutzt habe.

Linz, am . . . .
                                    (Unterschrift)